Stony Brook University

A Search for First Generation Leptoquarks in $\sqrt{s} = 7$ TeV pp Collisions with the ATLAS Detector

A Dissertation Presented

by

John Stupak III

to

The Graduate School

in Partial Fulfillment of the Requirements

for the Degree of

Doctor of Philosophy

in

Physics

Stony Brook University

August 2012

Stony Brook University
The Graduate School

John Stupak III

We, the dissertation committee for the above candidate for the
Doctor of Philosophy degree, hereby recommend
acceptance of this dissertation.

Michael Rijssenbeek – Dissertation Co-Advisor
Professor, Department of Physics and Astronomy

Dmitri Tsybychev – Dissertation Co-Advisor
Professor, Department of Physics and Astronomy

Derek Teaney – Chairperson of Defense
Professor, Department of Physics and Astronomy

Hong Ma
Physicist, Brookhaven National Laboratory

This dissertation is accepted by the Graduate School.

Charles Taber
Interim Dean of the Graduate School

Abstract of the Dissertation

A Search for First Generation Leptoquarks in $\sqrt{s} = 7$ TeV pp Collisions with the ATLAS Detector

by

John Stupak III

Doctor of Philosophy

in

Physics

Stony Brook University

2012

The Standard Model is an incomplete theory of nature. Numerous extensions of the Standard Model predict the existence of leptoquarks (LQ), color-triplet bosons which carry both baryon and lepton number. This dissertation presents the results of a search for pair production of first generation scalar leptoquarks in the $e\not{E}_T jj$ final state. The search is performed in pp collisions corresponding to an integrated luminosity of 1.03 fb^{-1}, at a center-of-mass energy $\sqrt{s} = 7$ TeV, recorded with the ATLAS detector at the LHC. A multivariate discriminant is used to distinguish signal-like events from background-like events. Observations are consistent with expectations from Standard Model backgrounds, thus limits on allowed LQ mass are determined. First generation scalar leptoquarks with mass $m_{LQ} < 558$ GeV are excluded at a 95% confidence level for $\beta \equiv BR(LQ \to eq) = 0.5$. When combined with a complimentary search in the $eejj$ final state, leptoquarks with mass $m_{LQ} < 607$ (660) GeV are excluded for $\beta = 0.5$ (1.0). These are the strongest limits in existence.

To my parents and brother.

Contents

List of Figures

List of Tables

List of Abbreviations

ALFA - Absolute Luminosity For ATLAS
BC - Bunch Crossing
BR - Branching Ratio
BSM - Beyond the Standard Model
CL - Confidence Level
CR - Control Region
CSC - Cathode Strip Chamber
CTP - Central Trigger Processor
DAQ - Data AcQuisition
DQ - Data Quality
EER - Electron Energy Resolution
EES - Electron Energy Scale
EF - Event Filter
EM - ElectroMagnetic
EMC - ElectroMagnetic Calorimeter
EMEC - ElectroMagnetic End-Cap calorimeter
ESel - Electron Selection
EW - ElectroWeak
EWSB - ElectroWeak Symmetry Breaking
FCAL - Forward CALorimeter
FSR - Final State Radiation
GRL - Good Runs List
GUT - Grand Unified Theory
HEC - Hadronic End-Cap calorimeter
HLT - High-Level Trigger
IBL - Insertable B-Layer
ID - Inner Detector
IP - Interaction Point
ISR - Initial State Radiation
JER - Jet Energy Resolution
JES - Jet Energy Scale

L1 - Level 1
L2 - Level 2
LAr - Liquid Argon
LHC - Large Hadron Collider
LL - Leading Log
LO - Leading Order
LQ - LeptoQuark
LUCID - LUminosity measurement using Cerenkov Integrating Detector
MC - Monte Carlo
MDT - Monitored Drift Tube
ME - Matrix Element
MM - Matrix Method
NLO - Next-to-Leading Order
NNLO - Next-Next-to-Leading Order
PDF - Parton Distribution Function
PMT - Photo-Multiplier Tube
QCD - Quantum ChromoDynamics
QED - Quantum ElectroDynamics
RPC - Resistive Plate Chamber
ROD - ReadOut Driver
ROS - ReadOut System
RoI - Region of Interest
SCT - SemiConductor Tracker
SF - Scale Factor
SM - Standard Model
TGC - Thin Gap Chamber
TRT - Transition Radiation Tracker
UE - Underlying Event
ZDC - Zero-Degree Calorimeter

Acknowledgments

First and foremost, I would like to thank my wonderful family for all the support they have given me over the years, without which I never would have made it to this point. I could not ask for a better family; from my parents, who showed me what it means to be a good person and always pushed me to succeed, to my brother, who I watched grow up and become a true friend, and my Uncle Darryl and the rest of my extended family. I am so grateful that I have all of you, but I would like to especially thank my parents. This dissertation is as much a product of their hard work as it is my own.

I would also like to thank my co-advisors, Michael and Dmitri. They both taught me so much during my time at Stony Brook, and made me the physicist I am today. The rest of the Stony Brook ATLAS group was also very important to my development. John (H) was always happy to answer my questions, so much so that I often thought of him as an advisor as well. I learned so much early on from Regina and later on from Carolina, both of whom I also consider great friends. Burton, David, and Karen were also very helpful on the leptoquark analysis.

I have had so many amazing teachers during my 22 year education, who are deserving of thanks as well. My early development was profoundly influenced by Mr. Carey, who is a one-of-a-kind teacher. Mrs. Murray did an amazing job teaching me algebra and geometry, reviving my enthusiasm for math in the process. My interest in physics was initially sparked by Mr. Seymour, and later by Mr. Welty. I probably wouldn't have gone on to graduate school if not for Dr. Track, who convinced me that I could succeed in physics. I owe you all a debt of gratitude.

Finally, I would like to thank all the friends I have made over the years. I'll never forget the many friends I grew up with in "the Boros." Gomes, Kay, and Marissa made the time I spent in Fairfield truly special, and remain very important to me. The friends I made at Stony Brook and CERN helped me persevere and finish this dissertation.

Chapter 1

Introduction

The goal of high energy physics is to understand the universe at its most fundamental level; what are the basic building blocks of matter and how do they interact with one another. This quest has led to the development of quantum field theory, a framework for understanding the dynamics of fundamental particles. A specific quantum field theory, the Standard Model (SM), is the most accurate description to date of the universe at small distance scales.

The SM facilitates calculation of many important physical quantities. For the most part, these calculations have been verified experimentally to extremely high precision. However, there are a handful of known experimental and theoretical shortcomings of the SM. Many beyond the Standard Model (BSM) theories have been proposed to address these deficiencies, of which numerous postulate the existence of a hypothetical particle known as a Leptoquark (LQ), which would decay to a lepton-quark pair.

1.1 The Standard Model

The SM is a quantum field theory based on local $\mathrm{SU}(3)_C \times \mathrm{SU}(2)_L \times \mathrm{U}(1)_Y$ gauge symmetry [1, 2]. The particle content of the SM is shown in Figure 1.1. There are twelve fermions; six leptons and six quarks. These fermions are the basic building blocks of matter, and interact with one another through the electromagnetic, weak, and strong interactions, which are mediated by gauge bosons. The form of these interactions is specified by the requirement of local gauge invariance. The symmetries of the SM require the gauge bosons to be massless. However, experiments have shown that the W and Z bosons are actually quite massive. The SM accommodates this fact through the Higgs mechanism [3–5], which spontaneously breaks the electroweak symmetry, giving mass to the W and Z bosons, and also the quarks and leptons.

Leptons			Force Carriers
ν_e	ν_μ	ν_τ	γ
e	μ	τ	$W^\pm$
			Z
Quarks			g
u	c	t	Higgs Boson
d	s	b	h

Table 1.1: The Standard Model particle content. The first column contains twelve fermions; six leptons and six quarks. The second column contains bosons; the force mediating gauge bosons of the electromagnetic, weak, and strong interactions, and the Higgs boson, responsible for the breaking of electroweak symmetry.

1.1.1 Leptons and Quarks

Fermions are spin-1/2 particles. This means their intrinsic angular momentum, or spin, is $\hbar/2$. They follow Fermi-Dirac statistics and obey the Pauli exclusion principle. Therefore, no two fermions may simultaneously exist in an identical quantum state. For every fermion f, there exists an antifermion $\overline{f}$ with identical mass but opposite sign quantum numbers.

The fermionic content of the SM is composed of leptons and quarks. Both leptons and quarks come in six flavors. These flavors are organized into three generations, shown in Table 1.2. Each generation contains two leptons and two quarks. Aside from the masses of the constituent particles, the generations are identical; each successive generation is heavier than the last (with the possible exception of neutrinos).

Charge	First Generation		Second Generation		Third Generation	
$[e]$		Mass [MeV]		Mass [MeV]		Mass [GeV]
0	ν_e	< 2 eV	ν_μ	< 0.19	ν_τ	< 18.2 MeV
-1	e	$0.510998910 \pm 0.000000013$	μ	105.658367 ± 0.000004	τ	1.77682 ± 0.00016
$+2/3$	u	1.7 - 3.1	c	1290^{+50}_{-110}	t	$172.9 \pm 0.6 \pm 0.9$
$-1/3$	d	4.1 - 5.7	s	100^{+30}_{-20}	b	$4.19^{+0.18}_{-0.06}$

Table 1.2: The three generations of leptons and quarks. For each of the fermions, the charge is listed as well as the mass. In the case of neutrinos which have very small mass, the experimentally determined mass upper bound is shown. Bare quarks have never been observed experimentally, therefore their masses generally have large uncertainties [6].

Leptons

The first generation of leptons is composed of the electron and its associated neutrino, e and ν_e, respectively. The electron has electric charge $-e$, whereas the electron neutrino is neutral. In the SM, neutrinos are massless, although experiment has shown this is only approximately true. However, various mechanisms can be used to give neutrinos mass within the context of the SM. Figure 1.2 shows the experimentally determined neutrino mass upper bounds. The second and third generations are composed of heavier versions of the electron, the muon μ and tau τ, along with their associated neutrinos.

A quantum number, known as lepton family number, is associated with each generation of lepton. These are electron number L_e, muon number L_μ, and tau number L_τ. First generation leptons have $L_e = +1$ and $L_\mu = L_\tau = 0$. Similarly, second and third generation leptons have $L_\mu = +1$ and $L_\tau = +1$ respectively, with all others being 0. Lepton family numbers are conserved in all SM interactions. Since the sign of antilepton quantum numbers are opposite to those of leptons, the SM only permits the creation and destruction of lepton-antilepton pairs. However, the phenomenon of neutrino oscillation has been observed experimentally, in which a neutrino of one flavor changes to a neutrino of another flavor [7]. This phenomenon violates conservation of lepton family number, but may still leave the sum, lepton number $L \equiv L_e + L_\mu + L_\tau$ as a conserved quantity.

All leptons interact through the weak interaction. The charged leptons interact through the electromagnetic interaction as well. Leptons do not possess color charge and therefore do not participate in the strong interaction.

Quarks

The first generation of quarks is composed of the up u and down d quarks. Up and down quarks have electric charge $+2e/3$ and $-e/3$ respectively. Unlike leptons, bare quarks have never been observed in nature. Instead, they form bound states known as baryons and mesons. Baryons are composed of three quarks or three antiquarks. Mesons are composed of a quark-antiquark pair. Baryons and mesons are collectively referred to as hadrons. The absence of bare quarks makes accurate experimental determination of their masses quite difficult, but approximate values can be obtained through the use of lattice gauge theory [8, 9], Quantum Chromodynamics (QCD) sum rules [10], and heavy quark effective theory [11]. World average values of the quark masses are shown in Table 1.2. The second and third generations are composed of heavier versions of the up and down quarks. The second (third) generation is composed of the charm c and strange s (top t and bottom b) quarks.

Quarks have an associated quantum number, known as baryon number B, which is equal to +1/3. Baryon number is conserved in all SM interactions. Since the sign of antiquark quantum numbers are opposite to those of quarks, the SM only permits the creation and destruction of quark-antiquark pairs. No exceptions to this rule have ever been observed experimentally.

Like the charged leptons, quarks interact through the weak and electromagnetic interactions. However, quarks possess and additional charge known as color charge, and thus interact through the strong interaction as well. There are three separate color charges, commonly referred to as red, green, and blue. Quarks possess either red, green, or blue color charge, while antiquarks possess either antired, antigreen, or antiblue color charge. Colored particles can't exist in isolation. Only colorless bound states of quarks are observed experimentally. Baryons consist of a red, green, and blue quark combination, which yields no net color charge. Mesons consist of a red-antired, green-antigreen, or blue-antiblue quark pair, which is colorless as well.

1.1.2 Quantum Electrodynamics

Quantum Electrodynamics (QED) is a quantum field theory which outlines the dynamics of the electromagnetic interaction. As such, leptons and quarks are represented by fields. Just as in classical field theory, the dynamics of a quantum system are completely specified by its Lagrangian. Spin-1/2 particle fields are represented by the Dirac Lagrangian density. Thus, the Lagrangian for a free electron of mass m is given by

$$\mathscr{L} = \overline{\psi}\left(\mathrm{i}\gamma^{\mu}\partial_{\mu} - m\right)\psi, \tag{1.1}$$

where γ^{μ} are the gamma matrices, ψ is a 4-component column vector representing the electron wave function, and $\overline{\psi} = \psi^{\dagger}\gamma^{0}$. If the global U(1) transformation

$$\psi \rightarrow \psi' = \mathrm{e}^{-\mathrm{i}\alpha}\psi, \tag{1.2}$$

with α constant, is applied to Lagrangian 1.1, then $\mathscr{L} \rightarrow \mathscr{L}' = \mathscr{L}$. Hence, Lagrangian 1.1 is invariant under a global U(1) transformation.

If instead α is allowed to vary as a function of spacetime, $\alpha = \alpha(x)$, then Equation 1.2 is an example of a local U(1) transformation. In this case,

$$\mathscr{L} \rightarrow \mathscr{L}' = \mathscr{L} + \overline{\psi}\gamma^{\mu}\left(\partial_{\mu}\alpha(x)\right)\psi. \tag{1.3}$$

Evidently, Lagrangian 1.1 is not invariant under such a local gauge transformation.

Local gauge invariance can be restored by the introduction of a gauge

field A_μ representing the photon, and making the replacement $\partial_\mu \rightarrow D_\mu$, where D_μ is an appropriately chosen covariant derivative which has the same transformation property as the electron field. In this case $D_\mu = \partial_\mu + \mathrm{i}qA_\mu$, where $q = -e$ is the electron charge. Just as in classical electromagnetism, there is a gauge freedom associated with the photon. The physical system is unaffected by the transformation

$$A_\mu \rightarrow A'_\mu = A_\mu + \partial_\mu \chi(x), \tag{1.4}$$

where $\chi(x)$ is an arbitrary function of spacetime. When the gauge transformation 1.2 is applied to the electron field, by making a simultaneous gauge transformation 1.4 of the photon field with $\chi(x) = \alpha(x)/q$, the covariant derivative will transform according to $D_\mu\psi \rightarrow (D_\mu\psi)' = \mathrm{e}^{-\mathrm{i}\alpha} D_\mu\psi$.

After making these modifications, Equation 1.1 takes the locally gauge invariant form

$$\mathscr{L} = \overline{\psi}\left(\mathrm{i}\gamma^\mu D_\mu - m\right)\psi - \frac{1}{4}F_{\mu\nu}F^{\mu\nu}, \tag{1.5}$$

where $F_{\mu\nu} = \partial_\mu A_\nu - \partial_\nu A_\mu$ is the electromagnetic field strength tensor. Lagrangian 1.5 now contains a $e^+e^-\gamma$ interaction and a term quadratic in the field strength tensor representing the photon kinetic energy. Thus, the requirement of local gauge invariance has led to the introduction of a gauge field representing the photon and requires an electron-photon interaction.

So far, there has been no mention of the muon and tau leptons, or any of the quarks. To include them, Lagrangian 1.5 must be generalized to

$$\mathscr{L} = \sum_i \left[\overline{\psi_i}\left(\mathrm{i}\gamma^\mu D_\mu - m_i\right)\psi_i\right] - \frac{1}{4}F_{\mu\nu}F^{\mu\nu}, \tag{1.6}$$

where $i = e, \mu, \tau, u, d, c, s, t, b$. This is the complete QED Lagrangian.

1.1.3 Electroweak Interaction

In the SM, the electromagnetic and weak interactions are unified into a single electroweak interaction [5]. The electroweak interaction is based on a local $\mathrm{SU}(2)_L \times \mathrm{U}(1)_Y$ gauge symmetry. Just as in Section 1.1.2, the requirement of local $\mathrm{SU}(2)_L \times \mathrm{U}(1)_Y$ gauge invariance leads to the introduction of gauge fields, and determines the interactions mediated by those fields.

The left-handed components of the electron neutrino and electron are grouped into an SU(2) doublet. The right-handed component of the electron is invariant under SU(2), and therefore placed in a singlet. There are no

right-handed neutrinos in the SM.

$$L_e = \begin{pmatrix} \nu_{eL} \\ e_L \end{pmatrix}, e_R \tag{1.7}$$

The dynamic portion of the electroweak Lagrangian for first generation leptons can be represented by

$$\mathscr{L}^e_{dyn} = L^\dagger_e \tilde{\sigma}^\mu \mathrm{i}\partial_\mu L_e + e^\dagger_R \sigma^\mu \mathrm{i}\partial_\mu e_R, \tag{1.8}$$

where $\sigma = (\sigma^0, \sigma^1, \sigma^1, \sigma^3)$, $\tilde{\sigma} = (\sigma^0, -\sigma^1, -\sigma^1, -\sigma^3)$, σ^0 is the identity matrix, and the σ^i are the Pauli matrices. Equation 1.8 is invariant under the global $\mathrm{SU}(2)_L \times \mathrm{U}(1)_Y$ transformation given by

$$L \to L' = \mathrm{e}^{\mathrm{i}\theta} U L \tag{1.9}$$

$$e_R \to e'_R = \mathrm{e}^{2\mathrm{i}\theta} e_R, \tag{1.10}$$

where $U = \mathrm{e}^{-\mathrm{i}\alpha^k \sigma^k}$, and θ and the α^k are real numbers parameterizing the transformation. However, it is not invariant under a local $\mathrm{SU}(2)_L \times \mathrm{U}(1)_Y$ transformation, where θ and the α^k are allowed to vary as a function of spacetime.

Lagrangian 1.8 can be made invariant under such a local transformation with the introduction of gauge fields and the replacement of the spacetime derivatives with an appropriately chosen covariant derivative. In this case, we are forced to introduce a U(1) gauge field $B_\mu(x)$ and three SU(2) gauge fields $W_\mu(x) = W^k_\mu(x)\sigma_k$. Under a $\mathrm{SU}(2)_L \times \mathrm{U}(1)_Y$ transformation, the gauge fields must transform as

$$B_\mu(x) \to B'_\mu(x) = B_\mu(x) + \frac{2}{g_1}\partial_\mu \theta(x) \tag{1.11}$$

$$W_\mu(x) \to W'_\mu(x) = U(x) W_\mu(x) U^\dagger(x) + \frac{2\mathrm{i}}{g_2}(\partial_\mu U(x)) U^\dagger(x), \tag{1.12}$$

where g_1 and g_2 are dimensionless parameters of the theory, the coupling strengths of the interactions. The necessary covariant derivatives are given by

$$D_\mu L_e = \left(\partial_\mu + \mathrm{i}\frac{g_1}{2} Y B_\mu + \mathrm{i}\frac{g_2}{2} W_\mu\right) L_e \tag{1.13}$$

$$D_\mu e_R = \left(\partial_\mu + \mathrm{i}\frac{g_1}{2} Y B_\mu\right) e_R \tag{1.14}$$

where Y is the hypercharge operator, whose eigenvalues are listed in Table 1.3.

These covariant derivatives transform according to the same rule as the fields themselves. With all these modifications, Equation 1.8 becomes

$$\mathscr{L}^{e}_{dyn} = L^{\dagger}_{e}\tilde{\sigma}^{\mu}\mathrm{i}D_{\mu}L_{e} + e^{\dagger}_{R}\sigma^{\mu}\mathrm{i}D_{\mu}e_{R} - \frac{1}{4}B_{\mu\nu}B^{\mu\nu} - \sum_{i=1}^{3}\frac{1}{4}W^{i}_{\mu\nu}W^{i\mu\nu}, \qquad (1.15)$$

where $B_{\mu\nu} = \partial_{\mu}B_{\nu} - \partial_{\nu}B_{\mu}$ and $W_{\mu\nu} = \left[\partial_{\mu} + \left(\mathrm{i}\frac{g_2}{2}\right)W_{\mu}\right]W_{\nu} - \left[\partial_{\nu} + \left(\mathrm{i}\frac{g_2}{2}\right)W_{\nu}\right]W_{\mu}$ are the field strength tensors. With these changes, the Lagrangian is now locally gauge invariant.

	Gauge Representation		
Field	$\mathrm{SU}(3)_C$	$\mathrm{SU}(2)_L$	Y
Q_u	3	2	$+1/3$
u_R	3	1	$+4/3$
d_R	3	1	$-2/3$
L_e	1	2	-1
e_R	1	1	-2

Table 1.3: Left- and right-handed particle content of the Standard Model. The representation under $\mathrm{SU}(3)_C$ and $\mathrm{SU}(2)_L$ are shown, as well as the the value of weak hypercharge [5].

The W_1 and W_2 gauge fields are electrically charged. The physical $W^{\pm}$ bosons are linear combinations of the W_1 and W_2, given by

$$W^{\pm}_{\mu} = \frac{W^{1}_{\mu} \mp \mathrm{i}W^{2}_{\mu}}{\sqrt{2}}. \qquad (1.16)$$

The W_3 and B gauge fields are electrically neutral. The physical Z and photon are linear combinations of these fields, given by

$$Z_{\mu} = W^{3}_{\mu}\cos\theta_W - B_{\mu}\sin\theta_W \qquad (1.17)$$

$$A_{\mu} = W^{3}_{\mu}\sin\theta_W - B_{\mu}\cos\theta_W, \qquad (1.18)$$

where the Weinberg angle θ_W is defined by $\sin\theta_W = g_1/\sqrt{g_1^2 + g_2^2}$. The interactions contained within Equation 1.15 only couples the $W^{\pm}$ to the left-handed lepton components, but couples the Z and photon to both the left- and right-handed components. Also, from the contained interactions it can be inferred that $g_2\sin\theta_W = g_1\cos\theta_W = e$.

In order to include second and third generation leptons, Equation 1.15

generalizes to

$$\mathscr{L}^{\ell}_{dyn} = \sum_{leptons} \left(L_e^{\dagger} \tilde{\sigma}^{\mu} \mathrm{i} D_{\mu} L_e + e_R^{\dagger} \sigma^{\mu} \mathrm{i} D_{\mu} e_R \right) - \frac{1}{4} B_{\mu\nu} B^{\mu\nu} - \sum_{i=1}^{3} \frac{1}{4} W^i_{\mu\nu} W^{i\mu\nu}, \quad (1.19)$$

Quarks are included in the electroweak sector in a similar manner. The left-handed components of the u and d quark are placed in SU(2) doublet, and the right-handed components reside in singlets.

$$Q_u = \begin{pmatrix} u_L \\ d_L \end{pmatrix}, u_R, d_R \quad (1.20)$$

Two additional doublets and four singlets exist for the second and third generation quarks. The covariant derivatives acting on the quark fields are the same as those which act on the lepton fields, but the quarks have different weak hypercharge assignments from the leptons. Therefore, the dynamic portion of the u and d quark Lagrangian is given by

$$\mathscr{L}^{q}_{dyn} = \sum_{quarks} Q_u^{\dagger} \tilde{\sigma}^{\mu} \mathrm{i} D_{\mu} Q_u + u_R^{\dagger} \sigma^{\mu} \mathrm{i} D_{\mu} u_R + d_R^{\dagger} \sigma^{\mu} \mathrm{i} D_{\mu} d_R. \quad (1.21)$$

Again, the W bosons couple only to the left-handed quark components, while the Z and photon couple to the right-handed components as well.

The dynamic portion of the electroweak Lagrangian is then

$$\mathscr{L}^{EW}_{dyn} = \mathscr{L}^{\ell}_{dyn} + \mathscr{L}^{q}_{dyn}. \quad (1.22)$$

This Lagrangian exhibits accidental global symmetries aside from the $\mathrm{SU}(2)_L \times \mathrm{U}(1)_Y$ which was imposed. A U(1) transformation of the form $L_e \rightarrow \mathrm{e}^{\mathrm{i}\alpha} L_e$, $e_R \rightarrow \mathrm{e}^{\mathrm{i}\alpha} e_R$ leaves Equation 1.22 invariant, which leads to conservation of electron number, as discussed in Section 1.1.1. Similar transformations on the muon and tau fields lead to conservation of muon and tau number. Additionaly, a U(1) transformation multiplying all negatively (positively) charged fields by $\mathrm{e}^{\mathrm{i}\alpha}$ ($\mathrm{e}^{-\mathrm{i}\alpha}$) leaves Equation 1.22 invariant, and implies conservation of electric charge.

Equation 1.22 is not invariant under charge conjugation C or a parity transformation P. Charge conjugation is the operation of changing the sign of all discrete quantum numbers, or equivalently exchanging all particles with antiparticles and vice-versa. A parity transformation is the inversion of spatial coordinates, $\boldsymbol{r} \rightarrow -\boldsymbol{r}$. The neutral current interactions, mediated by the Z and photon, preserve combined CP invariance. However, even combined CP symmetry is violated by weak current interactions, mediated by the $W^{\pm}$, in

the quark sector [12]. A third important potential symmetry is time reversal T, where $t \to -t$. Combined CPT invariance is required to maintain Lorentz invariance [13]. Therefore, the breaking of CP also implies the breaking of T symmetry.

1.1.4 Strong Interaction

QCD is the theory of the strong interaction, and is based on a local $\mathrm{SU}(3)_C$ gauge symmetry. It was mentioned in Section 1.1.1 that quarks possess color charge, which comes in three varieties. Therefore, each quark is placed in a color triplet

$$q_u = \begin{pmatrix} u_r \\ u_g \\ u_b \end{pmatrix}. \tag{1.23}$$

Given this representation, an appropriate globally SU(3) invariant quark Lagrangian would be

$$\mathscr{L}^q_{QCD} = \sum_{i=1}^{6} \overline{q}_i \mathrm{i}\gamma^\mu \partial_\mu q_i, \tag{1.24}$$

which is invariant under $q_i \to q_i' = U q_i$, where U is any member of SU(3).

However, under a local SU(3) transformation, where $U = U(x)$, Equation 1.24 is not invariant. In order to maintain local SU(3) invariance, eight gauge fields $G_\mu(x)$ must be introduced which represent gluons, and the space-time derivative must be replaced by the appropriate covariant derivative. The gauge fields must transform according to

$$G_\mu \to G'_\mu = U G_\mu U^\dagger + \frac{\mathrm{i}}{g_s} \left(\partial_\mu U\right) U^\dagger, \tag{1.25}$$

where g_s is a dimensionless parameter of the theory, the coupling strength of the color interaction. The covariant derivative appropriate to ensure local gauge invariance is given by

$$D_\mu q_i = \left(\partial_\mu + \mathrm{i} g_s G_\mu\right) q_i. \tag{1.26}$$

Thus, the locally SU(3) gauge invariant Lagrangian for quarks is given by

$$\mathscr{L}^q_{QCD} = \sum_{i=1}^{6} \left(\overline{q}_i \mathrm{i}\gamma^\mu D_\mu q_i\right) - \frac{1}{4} \sum_{i=1}^{8} G^i_{\mu\nu} G^{i\mu\nu}, \tag{1.27}$$

where $G_{\mu\nu} = \partial_\mu G_\nu - \partial_\nu G_\mu + \mathrm{i} g_s \left(G_\mu G_\nu - G_\nu G_\mu\right)$.

Unlike the electroweak interaction, C, P, and T are all conserved in QCD. At low energy scales, or equivalently large distance scales, QCD is a strongly coupled theory. This fact is responsible for the hadronic bound states of quarks. In this non-perturbative regime QCD calculations are extremely difficult, and techniques such as lattice gauge theory [14] must be exploited. At high energy scales, or equivalently small distance scales, the strong interaction becomes weakly interacting and quarks are effectively free [15]. In this regime the usual techniques of perturbation theory can be used, allowing high-precision calculations.

1.1.5 Higgs Mechanism

So far, there have been no mass terms in the EW or QCD Lagrangians. This is because local $\mathrm{SU}(3)_C \times \mathrm{SU}(2)_L \times \mathrm{U}(1)_Y$ gauge invariance has been required of the Lagrangian, and adding the spin-1 mass terms necessary to correctly describe massive W and Z bosons would violate this symmetry. The Higgs Mechanism [3–5] is the procedure used in the SM to generate mass for the W and Z while also preserving gauge invariance. It is also used to generate mass for the quarks and electrically charged leptons. The neutrinos, photon, and gluons remain massless, as observed experimentally.

A doublet of complex, scalar fields is postulated,

$$\Phi = \begin{pmatrix} \Phi_A \\ \Phi_B \end{pmatrix} = \begin{pmatrix} \phi_1 \\ \mathrm{i}\phi_2 \\ \phi_3 \\ \mathrm{i}\phi_4 \end{pmatrix}, \tag{1.28}$$

which can also be thought of as four real fields. The corresponding locally $\mathrm{SU}(2)_L \times \mathrm{U}(1)_Y$ gauge invariant contribution to the SM Lagrangian is then

$$\mathscr{L}^{\Phi}_{higgs} = (D_\mu \Phi)^\dagger (D^\mu \Phi) - V(\Phi^\dagger \Phi), \tag{1.29}$$

where $D_\mu \Phi = \left[\partial_\mu + (\mathrm{i}g_1/2)\, B_\mu + (\mathrm{i}g_2/2)\, W_\mu\right] \Phi$ is the appropriate covariant derivative, B_μ and W_μ are the gauge fields introduced in Section 1.1.3, and the potential V is taken to be

$$V(\Phi^\dagger \Phi) = \frac{m^2}{2\phi_0^2} \left[\left(\Phi^\dagger \Phi\right) - \phi_0^2 \right]. \tag{1.30}$$

The ground state of this potential is degenerate. $V(\Phi^\dagger \Phi)$ has a minimum for all values of the field such that $\phi_1^2 + \phi_2^2 + \phi_3^2 + \phi_4^2 = \phi_0^2$. ϕ_0 is referred to as the

vacuum expectation value. By choosing the specific ground state

$$\Phi_{ground} = \begin{pmatrix} 0 \\ \phi_0 \end{pmatrix} \tag{1.31}$$

and then expanding the field in terms of deviations from this ground state

$$\begin{pmatrix} 0 \\ \phi_0 + \frac{h(x)}{\sqrt{2}} \end{pmatrix}, \tag{1.32}$$

the $\mathrm{SU}(2)_L \times \mathrm{U}(1)_Y$ of the EW interaction is broken to the $\mathrm{U}(1)_{EM}$ of QED. $h(x)$ corresponds to the scalar Higgs field. Using the gauge freedom, any potential field configuration can be expressed this way, with $h(x)$ real. With this choice of ground state, $\mathscr{L}^{\Phi}_{higgs}$ takes the form

$$\begin{aligned} \mathscr{L}^{\Phi}_{higgs} =& \frac{1}{2}\partial_\mu h \partial^\mu h - m^2 h^2 + \frac{m^2 h^3}{\sqrt{2}\phi_0} + \frac{m^2 h^4}{8\phi_0^2} \\ &+ \frac{g_2^2}{2} W_\mu^- W^{+\mu} \left(\phi_0^2 + \sqrt{2}\phi_0 h + \frac{h^2}{2} \right) \\ &+ \frac{1}{4}\left(g_1^2 + g_2^2\right) Z_\mu Z^\mu \left(\phi_0^2 + \sqrt{2}\phi_0 h + \frac{h^2}{2} \right), \end{aligned} \tag{1.33}$$

where the first line describes a massive scalar Higgs boson and its self interactions, and the second and third lines describe massive W and Z bosons and their interactions with the Higgs. Thus, the W and Z bosons have acquired mass through the introduction of a scalar doublet and spontaneous breaking of the $\mathrm{SU}(2)_L \times \mathrm{U}(1)_Y$ symmetry.

The charged leptons also acquire mass as a result of the Higgs mechanism. The gauge invariant term

$$\mathscr{L}^{e}_{higgs} = -c_e \left[\left(L^\dagger \Phi \right) e_R + e_R^\dagger \left(\Phi^\dagger L \right) \right] \tag{1.34}$$

is added to the SM Lagrangian "by hand," which after symmetry breaking becomes

$$\mathscr{L}^{e}_{higgs} = -c_e \phi_0 \left(e_L^\dagger e_R + e_R^\dagger e_L \right) - \frac{c_e h}{\sqrt{2}} \left(e_L^\dagger e_R + e_R^\dagger e_L \right). \tag{1.35}$$

Equation 1.35 describes a massive electron with $m_e = c_e \phi_0$ and coupling to the Higgs proportional to m_e/ϕ_0. Similar terms exist for the muon and tau leptons.

Since $SU(3)_C$ is unbroken, gluons must remain massless. However, the quarks acquire mass through the Higgs mechanism. The SM Lagrangian contains the gauge invariant term

$$\mathscr{L}^q_{higgs} = -\phi_0 \sum_{ij} \Big[G^d_{ij} \left(L_i^\dagger \mathbf{\Phi} \right) d_{Rj} + G^{d*}_{ij} d^\dagger_{Rj} \left(\mathbf{\Phi}^\dagger L_i \right) \\ + G^u_{ij} \left(L_i^\dagger \epsilon \mathbf{\Phi}^\star \right) u_{Rj} - G^{u*}_{ij} u^\dagger_{Rj} \left(\mathbf{\Phi}^T \epsilon L_i \right) \Big], \tag{1.36}$$

where G^d_{ij} and G^u_{ij} are arbitrary 3×3 complex matrices, and

$$\epsilon = \begin{pmatrix} 0 & 1 \\ -1 & 0 \end{pmatrix}. \tag{1.37}$$

Unlike neutrinos, up type quarks have mass, which is responsible for the second line in Equation 1.36. Also, the quark mass matrices G^d_{ij} and G^u_{ij} are non-diagonal in flavor space. Unitary matrices D_L, D_R, U_L, U_R relate the flavor and mass eigenstates according to

$$\begin{aligned} d'_L &= D_L d_L \\ d'_R &= D_R d_R \\ u'_L &= U_L u_L \\ u'_R &= U_R u_R, \end{aligned} \tag{1.38}$$

where the primes indicate mass eigenstates. The mass matrices, real and diagonal in the mass basis, and are defined by

$$\begin{aligned} m^d &= \phi_0 D_L G^d D_R^\dagger \\ m^u &= \phi_0 U_L G^u U_R^\dagger. \end{aligned} \tag{1.39}$$

After symmetry breaking and transforming to the mass basis, Equation 1.36 takes the form

$$\mathscr{L}^q_{higgs} = -\sum_{i=1}^{3} \Big\{ m^d_i \left(d'^\dagger_{Li} d'_{Ri} + d'^\dagger_{Ri} d'_{Li} \right) + m^u_i \left(u'^\dagger_{Li} u'_{Ri} + u'^\dagger_{Ri} u'_{Li} \right) \\ + \frac{1}{\sqrt{2}\phi_0} \left[m^d_i h \left(d'^\dagger_{Li} d'_{Ri} + d'^\dagger_{Ri} d'_{Li} \right) + m^u_i h \left(u'^\dagger_{Li} u'_{Ri} + u'^\dagger_{Ri} u'_{Li} \right) \right] \Big\}. \tag{1.40}$$

The first line of Equation 1.40 contains six mass terms with real masses given by m^d (m^u) for the down (up) type quarks. The second line contains couplings

to the Higgs proportional to m/ϕ_0. In the remainder of this chapter, the mass eigenstates will be used with the primes dropped.

1.2 Beyond the Standard Model

The SM is a remarkably successful theory [6, 16]. It has been tested and validated by an array of high-precision tests over the course of decades. However, there are a few experimental hints which suggest that the SM may not be a complete theory of nature. Galactic rotational curves reveal the existence of dark matter [17, 18], whose existence can't be explained within the context of the SM. The only candidate weakly interacting particles in the SM are the neutrinos, but their masses are too small to account for the amount of observed dark matter [19]. In fact, the SM predicts massless neutrinos, but the recent discovery of neutrino oscillation [20, 21] shows that neutrinos must actually have non-zero mass. There is a small amount of CP violation in the SM [22], but not enough to account for the observed dominance of matter over antimatter in the universe. A 3.4σ discrepancy between the measured [23] and predicted [24] values of the muon anomalous magnetic moment has been observed. The Higgs boson, predicted by the SM, has not yet been observed experimentally. The ATLAS and CMS collaborations have recently observed small excesses of events in several final states [25, 26], which could be explained by a Higgs boson with a mass of $\sim$125 GeV. However, the excesses are not yet statistically significant, and more data is needed in order to make a definitive statement. Measurements of the $t\bar{t}$ forward-backward asymmetry performed at the Tevatron [27, 28] may be incompatible with the SM, but this too is inconclusive at the moment.

There are purely theoretical motivations for looking beyond the SM as well. The SM contains 19 parameters which are not predicted by the theory, but must instead be measured experimentally. It is believed that the values of these parameters should be predicted by a more complete theory. There is also the hierarchy problem [5, 29] associated with the mass of the Higgs boson. The bare Higgs mass m_{bare} is given by $\sqrt{2}m$, where m is a constant appearing in the Higgs potential, Equation 1.30. This bare mass is modified by quantum corrections to yield the physically observable Higgs mass m_h, according to

$$m_h^2 = m_{bare}^2 + C\Lambda^2, \tag{1.41}$$

where C is a dimensionless constant and Λ is the energy scale up to which the SM is valid. If the SM is expected to remain valid up to the Planck scale, or some other high energy scale, then the second term on the RHS

of Equation 1.41 is very large. But, the physically observable Higgs mass is required to be relatively small ($m_h \lesssim 1$ TeV) in order to preserve unitarity in WW scattering. Thus, there must be very large cancellations between the two terms on the RHS of Equation 1.41. For Λ equal to the Planck mass, a fine tuning of about one part in 10^{32} is required, but even for smaller values of Λ the amount of required fine tuning is unacceptable. Alternatively, Λ could be O(1 TeV), in which case fine tuning is not required, and new physics would be expected to manifest itself at LHC energies. Finally, the SM does not include gravity. A complete theory should incorporate gravity into a common theoretical framework with the three forces of the SM.

Many extensions to the SM have been proposed which attempt to remedy or explain some of the problems inherent in the SM. The most well known extension of the SM is supersymmetry [30–34], but there are also Grand Unified Theories which attempt to unify the strong and electroweak interactions [35, 36], models with composite lepton and quarks [37], and models with new strongly coupled interactions which are capable of generating mass without introducing fundamental scalars [38], just to name a few. Many of these BSM theories share a common feature; in at least some of their variations, they predict the existence of color-triplet bosons which carry both lepton and baryon number. These particles are referred to as leptoquarks.

1.2.1 Grand Unified Theories

Grand Unified Theories (GUTs) attempt to unify the electroweak interaction with the strong interaction, in analogy with the unification of the electromagnetic and weak interactions [35, 36]. Generally, a larger symmetry group is assumed, of which the $\mathrm{SU}(3)_C \times \mathrm{SU}(2)_L \times \mathrm{U}(1)_Y$ symmetry of the SM is a subgroup. Quarks and leptons are unified by placing them together in a fermionic multiplet. The symmetry group determines the interaction between fermions, which are mediated by new gauge bosons with a single coupling strength. These gauge bosons carry baryon as well as lepton number, i.e. they are leptoquarks. These models typically lead to lepton and baryon number violation, which much be suppressed through some mechanism in order to reproduce experimental observations.

1.2.2 Composite Models

Composite models postulate that quarks and leptons are not fundamental particles, but are instead composed of combinations of some fundamental building blocks [37]. Generally, the second and third generations are taken to be higher order excitations of the first generation, which explains the observed

similarity between generations of the SM. Composite models also explain the relationship between quark and lepton charges.

Leptoquarks arise naturally in composite models. Consider a simple model with two spin-1/2 fundamental particles, a T (with $Q = 1/3$) and a V (with $Q = 0$). In such a model, the u ($\overline{d}$) quark would be identified with a bound state of TTV, TVT, or VTT (TVV, VTV, or VVT). Assuming these bound states are degenerate, the quarks would have 3 different internal arrangements corresponding to the 3 color states. The e^+ (ν_e) would be identified with a bound state of TTT (VVV). There is only one internal arrangement of the leptons, thus they would not possess color charge. Generally, there is no reason why there couldn't be a $TTTTVV$ bound state, which would be identified with a $Q = 4/3$ LQ. Such a bound state could decay via

$$TTTTVV \rightarrow TVV\ TTT$$
$$LQ^{Q=4/3} \rightarrow \overline{d}\ e^+,$$

just as expected for a LQ.

1.2.3 Technicolor

In technicolor models a new interaction, technicolor, is introduced, along with technifermions similar to their SM counterparts, but which also carry a technicolor charge [38]. Technicolor is strongly interacting, which results in bound states of the technifermions. Among these bound states are technipions with the quantum numbers of a LQ. Technicolor gives mass to the W and Z bosons, and can also be made to give mass to the ordinary SM fermions. It is therefore an alternative to the Higgs mechanism, which some prefer as it does not require the introduction of a fundamental scalar.

1.3 Leptoquark Theory and Phenomenology

By definition, LQs are color-triplet bosons which carry both lepton and baryon number. A variety of BSM models predict the existence of LQs; however, these models all lead to a set of common features. There are also many characteristics of LQs which are model-dependent, such as the spin and electric charge. This section outlines the most general model of leptoquarks consistent with experimental observations, the phenomenology predicted by this model, and the relevant experimental constraints.

1.3.1 Leptoquark Production

Leptoquarks can be categorized by their fermion number, $F = L + 3B$. Leptoquarks have either $|F| = 0$ or $|F| = 2$, depending on whether they couple to a fermion-fermion or fermion-antifermion pair. The most general, effective low-energy LQ Lagrangian [39, 40] which satisfies $\mathrm{SU}(3)_C \times \mathrm{SU}(2)_L \times \mathrm{U}(1)_Y$ gauge invariance is given by

$$\mathscr{L} = \mathscr{L}^f_{|F|=0} + \mathscr{L}^f_{|F|=2} + \mathscr{L}^V, \tag{1.42}$$

where $\mathscr{L}^f_{|F|=0}$ ($\mathscr{L}^f_{|F|=2}$) characterizes the interactions of $|F| = 0$ ($|F| = 2$) leptoquarks with the SM fermions and $\mathscr{L}^V$ describes LQ interactions with the SM gauge bosons. The interactions with first generation fermions are given by

$$\begin{aligned}\mathscr{L}^f_{|F|=0} &= (h_{2L}\overline{u}_R\ell_L + h_{2R}\overline{q}_L \mathrm{i}\tau_2 e_R)R_2 + \tilde{h}_{2L}\overline{d}_R\ell_L\tilde{R}_2 \\ &+ (h_{1L}\overline{q}_L\ell_L + h_{1R}\overline{d}_R\gamma^\mu e_R)U_{1\mu} \\ &+ \tilde{h}_{1R}\overline{u}_R\gamma^\mu e_R\tilde{U}_{1\mu} + h_{3L}\overline{q}_L\tau\gamma^\mu\ell_L U_{3\mu} + h.c.\end{aligned} \tag{1.43}$$

$$\begin{aligned}\mathscr{L}^f_{|F|=2} &= (g_{1L}\overline{q}^c_L \mathrm{i}\tau_2\ell_L + g_{1R}\overline{u}^c_R e_R)S_1 \\ &+ \tilde{g}_{1R}\overline{d}^c_R e_R\tilde{S}_1 + g_{3L}\overline{q}^c_L \mathrm{i}\tau_2\tau\ell_L S_3 \\ &+ (g_{2L}\overline{d}^c_R\gamma^\mu\ell_L + g_{2R}\overline{q}^c_L\gamma^\mu e_R)V_{2\mu} \\ &+ \tilde{g}_2\overline{u}^c_R\gamma^\mu\ell_L\tilde{V}_{2\mu} + h.c.\end{aligned} \tag{1.44}$$

where $R_2, \tilde{R}_2, S_1,$ and S_3 ($U_{1\mu}, \tilde{U}_{1\mu}, U_{3\mu}, V_{2\mu},$ and $\tilde{V}_{2\mu}$) represent the possible scalar (vector) LQ fields, h_{2L}, h_{2R}, $\tilde{h}_{2L}$, h_{1L}, h_{1R}, $\tilde{h}_{1R}$, h_{3L}, g_{1L}, g_{1R}, $\tilde{g}_{1R}$, g_{3L}, g_{2L}, g_{2R}, and $\tilde{g}_{2L}$ represent LQ-ℓ-q Yukawa couplings, and $\tau = (I, \boldsymbol{\sigma})$. Similar terms exist for second and third generation leptons. The interactions specified in Equations 1.43 and 1.44 conserve baryon and lepton numbers, and are flavor diagonal. Table 1.4 summarizes the various LQ fields.

Leptoquarks also interact with the SM gauge bosons. The most general $\mathrm{SU}(3)_C \times \mathrm{SU}(2)_L \times \mathrm{U}(1)_Y$ gauge invariant interaction of scalar and vector

LQ	Spin	F	T_3	Q	$\lambda_L(\ell^{\pm}q)$	$\lambda_R(\ell^{\pm}q)$	$\lambda_L(\nu q)$
S_1	0	2	0	$+1/3$	g_{1L}	g_{1R}	$-g_{1L}$
$\tilde{s}_1$	0	2	0	$+4/3$	0	$\tilde{g}_{1R}$	0
S_3	0	2	$+1$	$+4/3$	$-\sqrt{2}g_{3L}$	0	0
			0	$+1/3$	$-g_{3L}$	0	$-g_{3L}$
			-1	$-2/3$	0	0	$\sqrt{2}g_{3L}$
R_2	0	0	$+1/2$	$+5/3$	h_{2L}	h_{2R}	0
			$-1/2$	$+2/3$	0	$-h_{2R}$	h_{2L}
$\tilde{R}_2$	0	0	$+1/2$	$+2/3$	h_{2L}	0	0
			$-1/2$	$-1/3$	0	0	$\tilde{h}_{2L}$
$V_{2\mu}$	1	2	$+1/2$	$+4/3$	g_{2L}	g_{2R}	0
			$-1/2$	$+1/3$	0	g_{2R}	g_{2L}
$\tilde{V}_{2\mu}$	1	2	$+1/2$	$+1/3$	$\tilde{g}_{2L}$	0	0
			$-1/2$	$-2/3$	0	0	$\tilde{g}_{2L}$
$U_{1\mu}$	1	0	0	$+2/3$	h_{1L}	h_{1R}	h_{1L}
$\tilde{U}_{1\mu}$	1	0	0	$+5/3$	0	$\tilde{h}_{1R}$	0
$U_{3\mu}$	1	0	$+1$	$+5/3$	$-\sqrt{2}h_{3L}$	0	0
			0	$+5/3$	$-h_{3L}$	0	$-h_{3L}$
			-1	$-1/3$	0	0	$\sqrt{2}h_{3L}$

Table 1.4: All potential LQ states and their associated spin, fermion number F, third component of weak isospin T_3, charge Q, coupling to left-handed charged leptons $\lambda_R(\ell^{\pm}q)$, coupling strength to right-handed charged leptons $\lambda_R(\ell^{\pm}q)$, and coupling to neutrinos $\lambda_L(\nu q)$ [39].

leptoquarks Ψ with gluons are given by

$$\mathscr{L}_S^g = \sum_{scalars} \left[\left(D_{ij}^{\mu} \Psi^j \right)^{\dagger} \left(D_{\mu}^{ik} \Psi_k \right) - m_S \Psi^{i\dagger} \Psi_i \right] \tag{1.45}$$

$$\mathscr{L}_V^g = \sum_{vectors} \left\{ -\frac{1}{2} V_{\mu\nu}^{i\dagger} V_i^{\mu\nu} + M_V^2 \Psi_{\mu}^{i\dagger} \Psi_i^{\mu} \right.$$
$$\left. -\mathrm{i} g_s \left[(1-\kappa_G)\, \Psi_{\mu}^{i\dagger} t_{ij}^a \Psi_{\nu}^j \mathcal{G}_a^{\mu\nu} + \frac{\lambda_G}{M_V^2} V_{\sigma\mu}^{i\dagger} t_{ij}^a V_{\nu}^{j\mu} \mathcal{G}_a^{\nu\sigma} \right] \right\}, \tag{1.46}$$

where m_S (m_V) is the scalar (vector) LQ mass, the covariant derivative $D_{ij}^{\mu} = \partial_{\mu}\delta^{ij} - \mathrm{i} g_s t_a^{ij} G_{\mu}^a$, δ^{ij} is the Kronecker δ, t_a are the generators of SU(3), the vector LQ field strength tensor $V_{\mu\nu}^i = D_{\mu}^{ij}\Psi_{\nu k} - D_{\nu}^{ik}\Psi_{\mu k}$, the gluon field strength tensor $\mathcal{G}_{\mu\nu}^a = \partial_{\mu}G_{\nu}^a - \partial_{\nu}G_{\mu}^a + g_s f^{abc} G_{\mu b} G_{\nu c}$, f are the SU(3) structure constants, and κ_G and λ_G represent dimensionless parameters of the theory, anomalous coupling strengths. In both the scalar and vector case, this leads to *LQ*-*LQ*-*g* and *LQ*-*LQ*-*g*-*g* interactions. Leptoquarks also interact with the other SM gauge bosons, but these interactions can be neglected at a hadron collider.

At a hadron collider, leptoquarks can be produced both singly or in pairs, as shown in Figures 1.1 and 1.2 respectively. Single LQ production occurs in association with lepton, either charged or neutral.

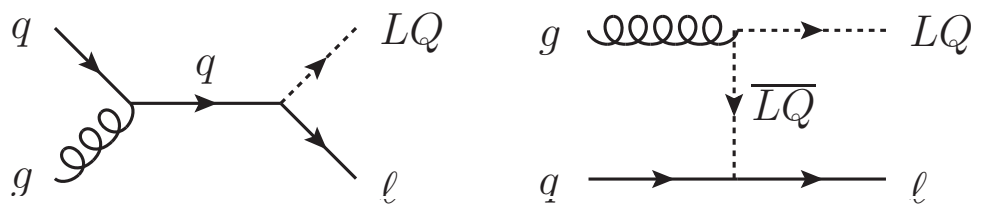

Figure 1.1: Leading order Feynman diagrams representing single LQ production. S-channel diagram (left) and t-channel diagram (right).

The single LQ production diagrams, as well as the t-channel pair production diagram with lepton exchange, include an *LQ*-ℓ-*q* vertex. Accordingly, the rate of these processes is proportional to the square of the Yukawa couplings present in Equations 1.43 and 1.44. LQ pair production (excluding t-channel lepton exchange) does not have this dependence, as there are no *LQ*-ℓ-*q* vertices in the diagrams of Figure 1.2. Instead, pair production of scalar and vector leptoquarks occurs through the gluon interactions contained in Equations 1.45 and 1.46 respectively. The scalar production rate depends only on

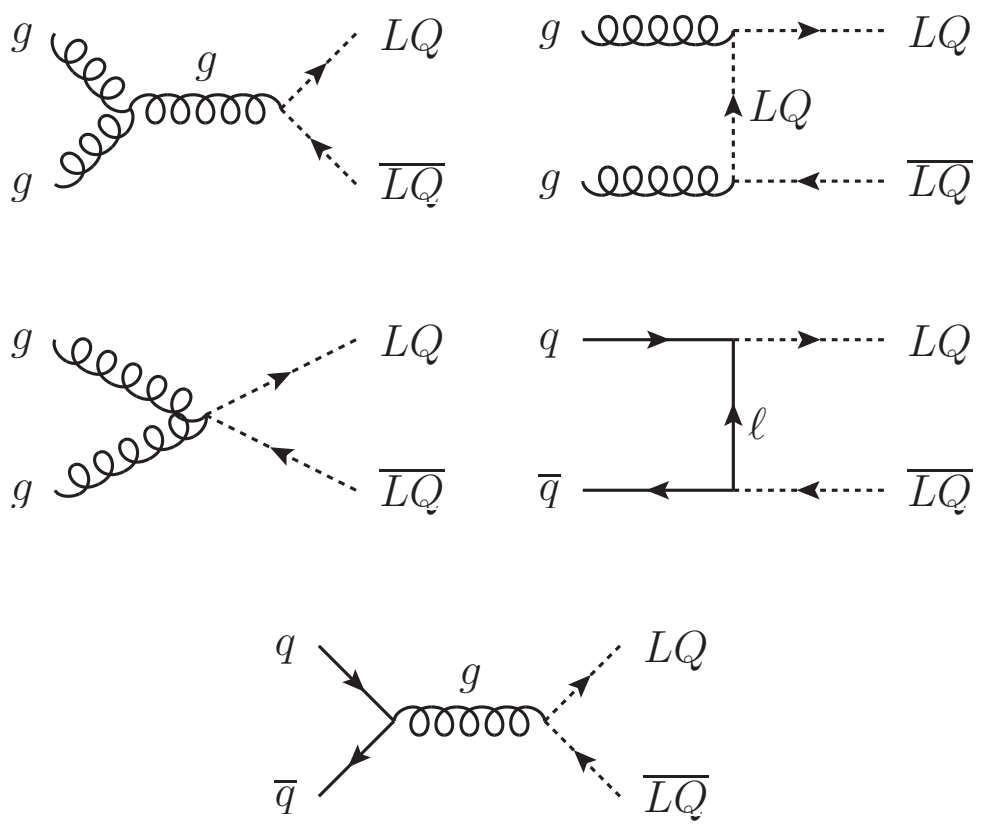

Figure 1.2: Leading order Feynman diagrams representing LQ pair production. Gluon fusion (left), t-channel diagrams (right), and quark-antiquark annihilation (bottom).

the LQ mass, whereas vector LQ production depends on the anomalous κ_G and λ_G couplings as well, which are model-dependent. In all cases, the the LQ decay rate depends on the Yukawa coupling.

Low-energy precision experiments [41, 42] have placed upper bounds on the *LQ*-ℓ-q Yukawa couplings, which render single production and pair production through t-channel lepton exchange negligible at the Large Hadron Collider (LHC) for small LQ masses. Instead, pair production through gluon fusion and quark-antiquark annihilation dominates. The parton-level leading order (LO) cross sections for these processes [43] are given by

$$\hat{\sigma}_{gg}^{LO} = \frac{\alpha_s^2 \pi}{96\hat{s}} \left[v\left(41 - 31v^2\right) + \left(18v^2 - v^4 - 17\right) \log\frac{1+v}{1-v} \right] \tag{1.47}$$

$$\hat{\sigma}_{q\bar{q}}^{LO} = \frac{2\alpha_s^2 \pi}{27\hat{s}} v^3, \tag{1.48}$$

where $v = (1 - 4m_{LQ}^2/\hat{s})^{1/2}$ is the LQ velocity and $\hat{s}$ is the square of the subprocess center-of-mass energy. At small LQ masses, gluon fusion dominates. As LQ mass increases, quark-antiquark annihilation becomes increasingly important, contributing ∼30% of the total cross section at $m_{LQ} = 1.5$ TeV.

Next to leading order (NLO) corrections to the cross sections have been calculated as well [43]. The NLO cross sections are given by

$$\hat{\sigma}_{ij} = \frac{\alpha_s^2\left(m_{LQ}^2\right)}{m_{LQ}} \left\{ f_{ij}^B(v) + 4\pi\alpha_s\left(m_{LQ}^2\right) \left[f_{ij}^{V+S}(v) + f_{ij}^H(v) \right] \right\}, \tag{1.49}$$

where f^B represents the born cross section term, f^{V+S} represents the virtual and soft gluon corrections, and f^H represents hard gluon corrections. Near threshold for LQ production, where $\hat{s} \simeq 4m_{LQ}^2$, these term are given by

$$\begin{array}{ll} f_{gg}^B = \frac{7\pi v}{384} & f_{q\bar{q}}^B = \frac{\pi v^3}{54} \\ f_{gg}^{V+S}/f_{gg}^B = \frac{11}{336v} & f_{q\bar{q}}^{V+S}/f_{q\bar{q}}^B = -\frac{1}{48v} \\ f_{gg}^H/f_{gg}^B = \frac{3}{2\pi^2}\log^2(8v^2) - \frac{183}{28\pi^2}\log(8v^2) & f_{q\bar{q}}^H/f_{q\bar{q}}^B = \frac{2}{3\pi^2}\log^2(8v^2) - \frac{107}{36\pi^2}\log(8v^2). \end{array} \tag{1.50}$$

The k-factor, defined as the ratio of the NLO and LO cross sections, varies from ∼1.5-2, depending on the LQ mass. The LO and NLO cross sections are shown in Figure 1.3.

1.3.2 Experimental Signature

In the most general case, the branching fraction β of a LQ to a charged lepton is unknown. Assuming the *LQ*-ℓ-q Yukawa coupling is sufficiently large

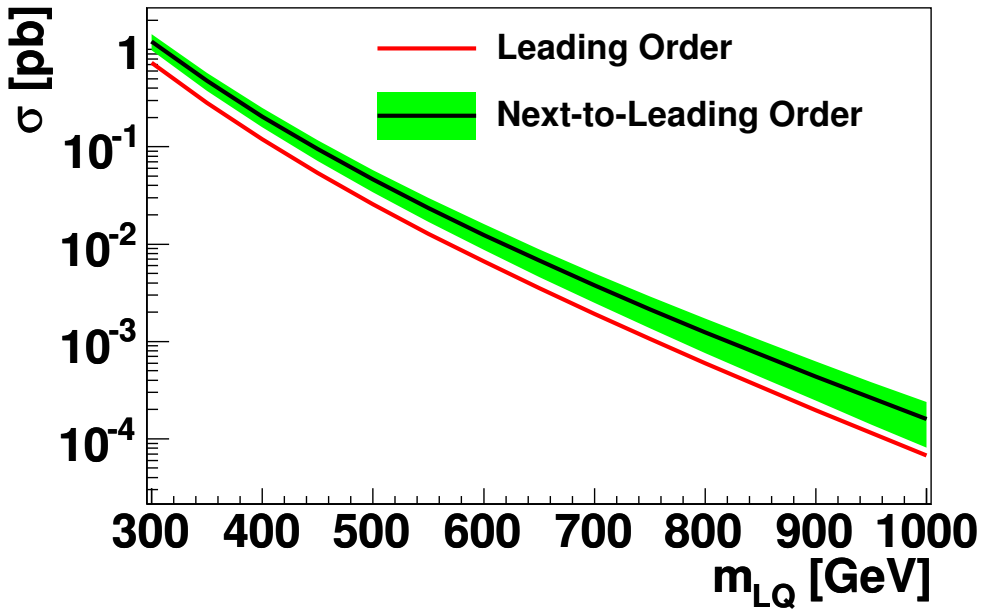

Figure 1.3: Scalar LQ pair production cross section as a function of m_{LQ}. LO and NLO values are shown in red and black respectively. The green band represents the systematic uncertainty on the NLO cross section from the choice of parton density function. The LO CTEQ6L1 parton distribution function was used to calculate the cross section central value, while the CTEQ6.6 NLO parton distribution function error sets were used to calculate the systematic uncertainty [43].

to allow prompt LQ decay, there are three possible decay modes for a pair of leptoquarks, $qq + \{\ell^+\ell^-, \ell^\pm\nu, \nu\nu\}$, which are maximally produced for $\beta = 1$, 0.5, and 0 respectively. Since there is no momentum transverse to the beam direction in the initial state, the vector sum of the transverse momentum of all final state particles is expected to be zero. Any neutrinos produced in the LQ decay will escape undetected, thus their momentum will go "missing" and a significant transverse momentum imbalance results. The $\not\!\!E_T$ vector is defined as minus the transverse momentum imbalance. The longitudinal momentum of the initial state partons is unknown, so the final state momentum imbalance in the longitudinal direction is not a useful quantity. Due to the confining nature of QCD, each of the bare quarks will shower and hadronize, forming a jet, denoted j. Thus, the potential final states which may result from pair production of leptoquarks are $jj + \left\{\ell^+\ell^-, \ell^\pm\not\!\!E_T, \not\!\!E_T\right\}$. In the case where both leptoquarks decay to a charged lepton, there will be two lepton-jet combinations whose invariant mass roughly equals that of the LQ. In the case where only one LQ decays to a charged lepton, there will be one such combination. But the transverse mass of the other jet and the $\not\!\!E_T$, defined by

$$m_T^{LQ} = \sqrt{2p_T^j \not\!\!E_T \left(1 - \cos\Delta\phi_{j,\not\!\!E_T}\right)}, \tag{1.51}$$

where p_T^j is the jet transverse momentum and $\Delta\phi_{j,\not\!\!E_T}$ is the azimuthal separation of the jet and $\not\!\!E_T$, should also be relatively close to the LQ mass. In all cases, due to the large LQ mass the jets and leptons should have relatively large p_T.

1.3.3 Experimental Constraints

In Section 1.3.1 the LQ Lagrangian, Equation 1.42 was taken to be lepton and baryon number conserving. This was done in order to accommodate very strict experimental limits on lepton and baryon violating processes [41, 42], taken for example from searches for proton decay. Suppression of proton decay also requires $\sqrt{\lambda} \lesssim \frac{m_{LQ}}{25\ \text{TeV}}$ [44], where λ is the LQ-ℓ-q Yukawa coupling. In this study, λ is taken to be $0.01\times4\pi\alpha_{EM}$, which is consistent with experimental constraints. This choice allows for prompt decay and limits single LQ production, but has no other effect. Leptoquarks were also assumed to come in three generations, just like the quarks and leptons. This was done to accommodate experimental constraints from the observed smallness of flavor changing neutral currents [41, 42].

The most stringent first generation mass limits to date come from the Tevatron and the LHC. The DØ experiment performed a search for first generation

leptoquarks in $\sqrt{s} = 1.96$ TeV $p\overline{p}$ collisions at the Tevatron [45]. All three of the $jj + \left\{e^+e^-, e^{\pm}\not\!\!E_T, \not\!\!E_T\right\}$ final states were examined. Using 1 fb^{-1} of data, 95% confidence level (CL) lower limits on m_{LQ} of 299 GeV, 284 GeV, and 216 GeV were established, for branching fractions to an electron and a quark $\beta = 1$, 0.5, and 0.02 respectively. More recent searches at the LHC have not been performed in the $jj\not\!\!E_T$ channel, so for small β this analysis yields the most stringent mass bound to date.

The CMS experiment performed a search in $\sqrt{s} = 7$ TeV pp collisions at the LHC [46]. Only the jje^+e^- final state was examined. Using 33 pb^{-1} of data, a 95% CL lower limit on m_{LQ} of 385 GeV was established for $\beta = 1$. For large β, this search yields the most stringent mass bound to date.

An earlier search was also performed by the ATLAS experiment [47]. This search used 35 pb^{-1} of $\sqrt{s} = 7$ TeV pp collision data, and examined the jje^+e^- and $jje^{\pm}\not\!\!E_T$ final states. For $\beta = 1$ (0.5), a 95% CL lower limit on m_{LQ} of 376 (319) GeV was established. This analysis yields the most stringent mass bound to date for intermediate values of β. The bounds for arbitrary values of β are shown in Figure 1.4 for the DØ, CMS, and ATLAS searches.

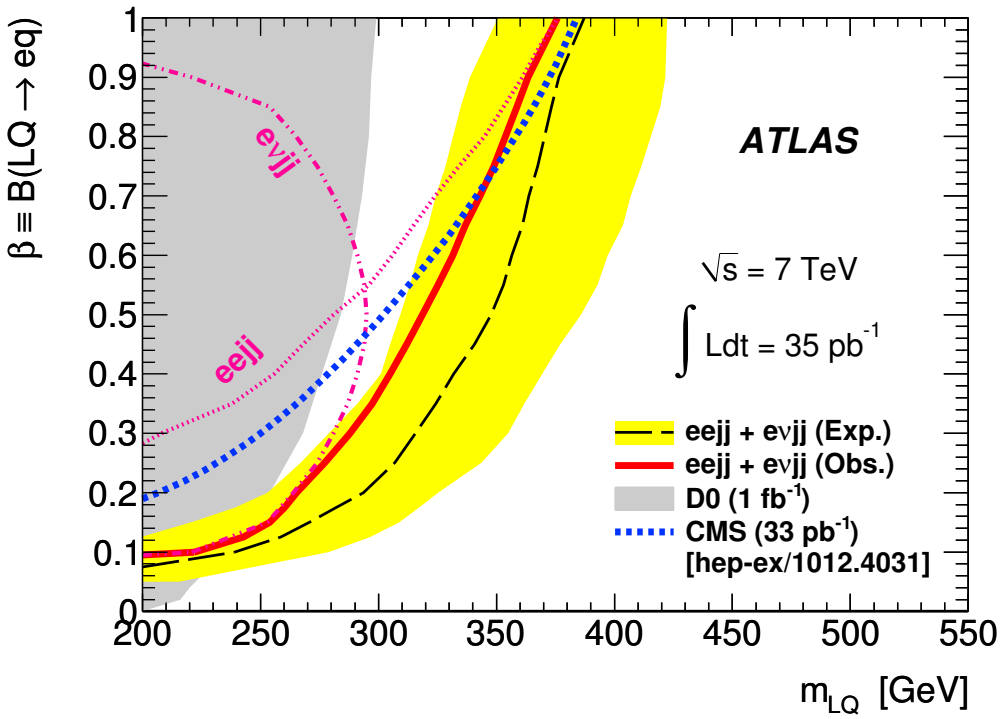

Figure 1.4: 95% CL exclusions resulting from the DØ [45], CMS [46], and ATLAS [47] first generation LQ searches shown in the β versus m_{LQ} plane. The grey area represents the DØ excluded region and the dotted blue line indicates the CMS exclusion. The pink dotted (dashed-dotted) line indicates the exclusion resulting from the ATLAS search in the $eejj$ ($e\not{E}_T jj$) channel alone. The black dashed line indicates the expected exclusion resulting from the ATLAS search combining the $eejj$ and $e\not{E}_T jj$ channels, with the yellow band indicating the $\pm 1\sigma$ uncertainty. The solid red line represents the observed combined limit.

Chapter 2

The LHC and ATLAS Detector

According to Einstein's famous equation $E = mc^2$, energy and mass are interchangeable. Therefore, in order to produce heavy particles, a large amount of energy is required. The LHC has been designed and constructed to produce highly energetic pp collisions in which a variety of elementary particles may be produced. High energy collisions also enable the study of extremely small distance scales.

Heavy particles produced in the pp collision typically decay very rapidly. Highly advanced detectors, such as ATLAS, are needed to observe and measure the properties of their decay products. From the particles which are eventually detected and measured, the properties of their parent particles may be deduced, enabling the study of SM particles such as the the W and Z bosons and top quark, or hypothesized particles such as leptoquarks.

2.1 The Large Hadron Collider

The Large Hadron Collider [48, 49] is a particle accelerator located on the border between France and Switzerland. It accelerates two counter-rotating beams of protons which intersect at four interaction points (IP) around a 27 km ring, producing highly energetic collisions. These collisions produce an array of elementary particles in sufficient quantities for detailed study.

The beams are not continuous streams of particles, but rather trains of regularly spaced proton bunches. The LHC was designed to operate with 2,808 bunches of protons per beam, with 1.15×10^{11} protons per bunch. In this configuration, pairs of bunches would interact within each of the four IPs every 25 ns. The machine was designed to accelerate the protons to 7 TeV, for a total center-of-mass energy $\sqrt{s} = 14$ TeV. During 2010-2011, the machine operated at only $\sqrt{s} = 7$ TeV, which was still a factor of 3.5 more energetic than the

Tevatron [50], which had previously been the most energetic accelerator in the world. The LHC is now operating at $\sqrt{s} = 8$ TeV in 2012, after which it will undergo a long shutdown to prepare the machine for operation at the design energy. The LHC was also designed to accelerate and collide lead ions with up to 2.8 TeV per nucleon.

In order to bend the proton beams into a circle, state-of-the-art superconducting magnets are needed. The LHC uses dipole magnets for this purpose, which are cooled to less than 2 K using superfluid helium. These magnets can produce a maximum field of 8.33 T. A total of 1,232 main dipoles are placed along the LHC ring, in addition to ∼7,000 quadrupole, sextupole, octupole, and decapole magnets which are used to correct and focus the beams [51].

The CERN accelerator complex provides the LHC with 450 GeV protons, which are then accelerated up to the collision energy. Before reaching the LHC, protons are accelerated in turn by the Linac2, Proton Synchrotron Booster, Proton Synchrotron, and Super Proton Synchrotron. The accelerator complex is shown in Figure 2.1.

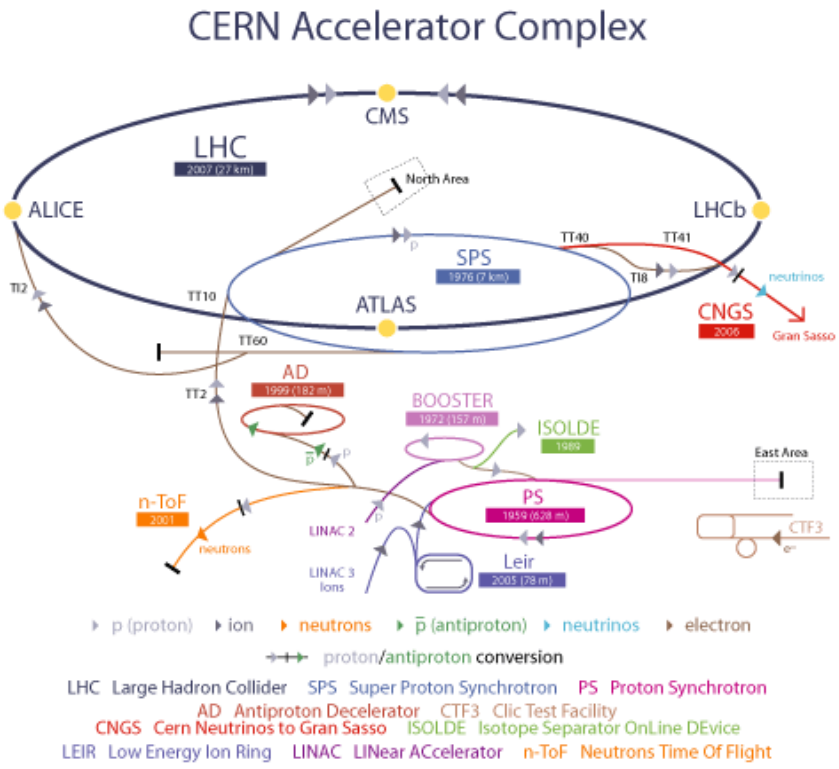

Figure 2.1: The accelerator complex at CERN. A series of boosters provide the LHC with 450 GeV protons which are then accelerated up to 3.5 TeV [52].

The rate of a particular interaction is proportional to the instantaneous luminosity L and the cross section σ of the interaction,

$$\frac{\mathrm{d}N}{\mathrm{d}t} = L\sigma. \tag{2.1}$$

The cross section is a measure of the likelihood of a given interaction taking place. The instantaneous luminosity depends only on the beam parameters, and is given by

$$L = \frac{N_b^2 n_b f_{rev} \gamma F}{4\pi\varepsilon_n \beta^\star}, \tag{2.2}$$

where N_b is the number of particles per bunch, n_b is the number of bunches per beam, f_{rev} is the revolution frequency, γ is the relativistic gamma factor, ε_n is the normalized transverse beam emittance, β^* is the beta function at the collision point, and F is the geometric luminosity reduction factor. The geometric luminosity factor depends on the crossing angle at the IP θ_c, the longitudinal beam size σ_Z, and the transverse beam size σ_Z according to

$$F = \left[1 + \left(\frac{\theta_c \sigma_z}{2\sigma^*}\right)^2\right]^{-1/2}. \tag{2.3}$$

Table 2.1 summarizes the design values of these parameters.

Parameter	Value
N_b	1.15×10^{11}
n_b	2,808
f_{rev}	11.22 kHz
γ	7,461
F	0.836
ε_n	3.75 μm rad
$\beta^\star$	0.55 m

Table 2.1: LHC beam parameter design values [48, 49].

The LHC was designed to reach a peak instantaneous luminosity of 1-2.5×10^{34} cm^{-2}s^{-1}. The integrated luminosity $\int L\mathrm{d}t$ is simply the time integral of the instantaneous luminosity, and gives the total number of interactions over some time period. Ultimately, it is hoped that the LHC can accumulate 80-120 fb^{-1} of pp collisions per year. During 2011, 5.61 fb^{-1} of integrated luminosity was delivered to the ATLAS detector [53].

Two general purpose particle detectors are located on opposite sides of the

LHC ring, ATLAS [54] and CMS [55]. These are "onion-type" detectors with near hermetic coverage of the IP, consisting of a tracking system close to the IP, surrounded by a calorimeter system, which is itself surrounded by a muon system. There are three other detectors located along the ring designed for specific purposes, LHCb [56], ALICE [57], and TOTEM [58].

2.2 The ATLAS Detector

The ATLAS detector [54], shown in Figure 2.2, is a general purpose particle detector designed to have strong performance for a wide array of physics scenarios. The inner detector (ID) surrounds the IP, providing pattern recognition, momentum measurement of charged particles, and vertex identification. A solenoid magnet surrounds the ID, providing a 2 T axial magnetic field which bends the trajectories of charged particles, allowing the determination of their momenta. The solenoid is surrounded by the calorimeter, providing energy measurement of electrons, photons, and hadrons. Surrounding the calorimeter are air-core toroidal magnets and the muon spectrometer. The muon spectrometer is designed to measure the momenta of muons to high precision within the magnetic field provided by the toroid magnets. ATLAS also has an advanced trigger system, which is capable of operating at up to 400 Hz [59].

2.2.1 Coordinate System

ATLAS uses a right-handed coordinate system. The origin is defined as the nominal interaction point. The beam direction defines the z-axis. The x-axis points to the center of the ring and the y-axis points upward. The azimuthal angle ϕ is measured with respect to the x-axis and the polar angle θ is measured from the z-axis. The pseudorapidity η, typically used instead of θ, is defined by

$$\eta = -\ln\left(\tan\frac{\theta}{2}\right). \tag{2.4}$$

The angular separation in η-ϕ space ΔR, is defined by

$$\Delta R = \sqrt{(\Delta\eta)^2 + (\Delta\phi)^2}. \tag{2.5}$$

2.2.2 Inner Detector

The ID extends up to $|\eta| < 2.5$ and consists of three sub-detectors, shown in Figure 2.3. The innermost of these is the Pixel Detector, followed by the semi-

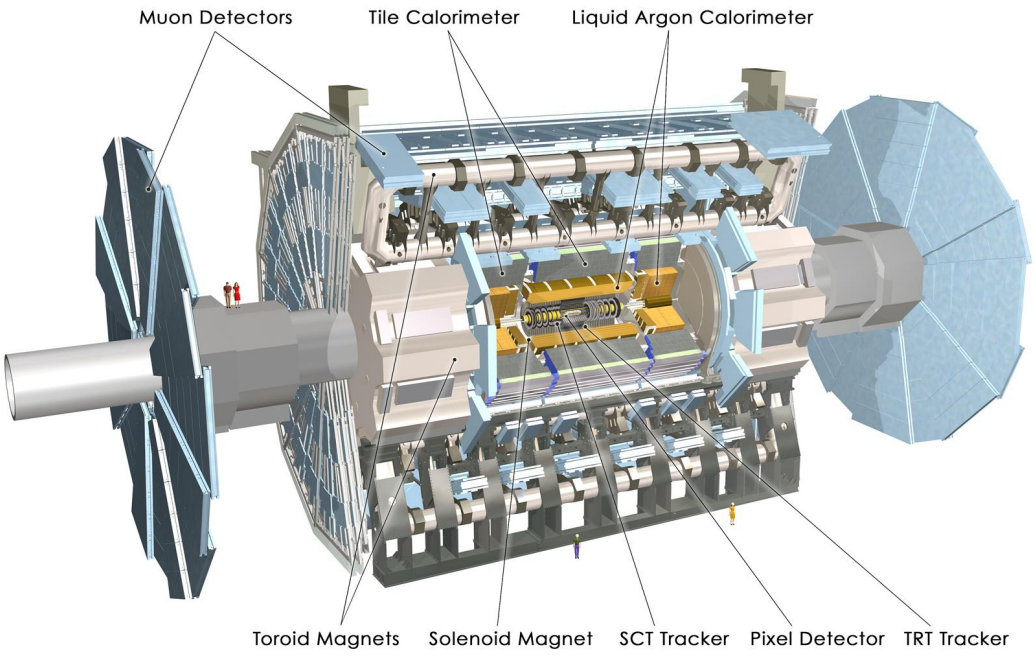

Figure 2.2: The ATLAS detector. A tracking system surrounds the IP, followed by the calorimeters and muon system [60].

conductor tracker (SCT) and the transition radiation tracker (TRT). Charged particle trajectories are bent by a 2 T axial magnetic field provided by a solenoid magnet. Charged particles produced at the interaction point traverse the ID, producing a series of hits in the sub-detectors along their trajectory. From these position measurements, particle tracks are determined. The track p_T is determined from its radius of curvature. Thus, In order to achieve good momentum resolution, a series of precise position measurements are needed. The track p_T design resolution is $\sigma_{p_T}/p_T = 0.05\% \cdot p_T[\text{GeV}] \oplus 1\%$, where $\oplus$ denotes addition in quadrature. Charged tracks with p_T as low as 0.5 GeV can be measured. The ID also assists electron identification up to $|\eta| < 2$. Of course, a typical event will contain many charged particles, thus good pattern recognition is needed in order to correctly associate each hit to the correct track. From the collection of tracks observed in an event, primary and secondary vertices can be resolved [54].

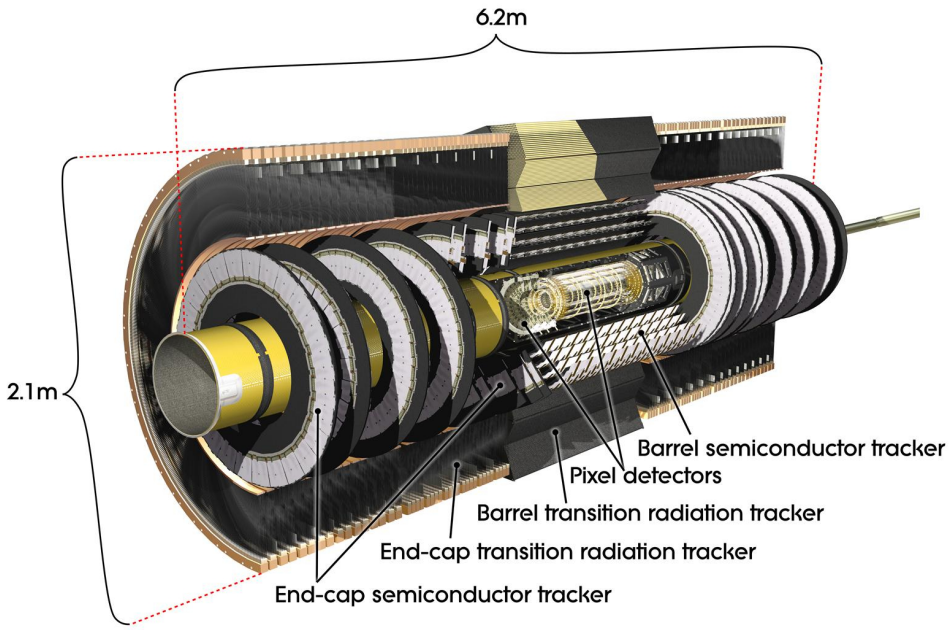

Figure 2.3: The ATLAS ID. The Pixel Detector surrounds the IP, followed by the SCT and TRT [60].

Pixel Detector

The Pixel Detector is a semiconductor tracker [62]. The sensors are composed of 250 μm thick n-doped silicon bulk with n^+ and p^+ implants on op-

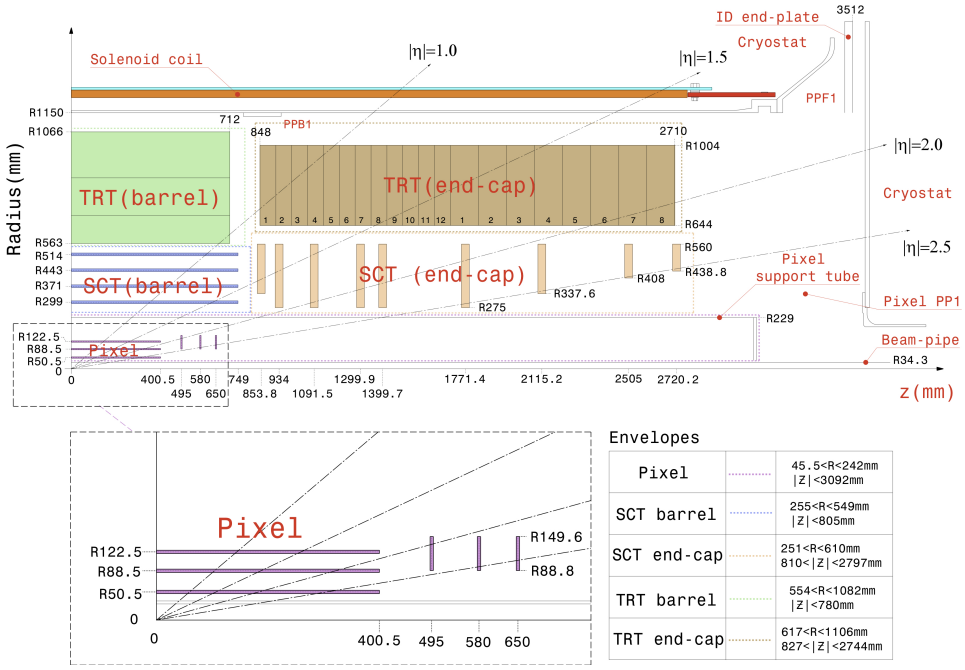

Figure 2.4: A Quadrant of the ID in the R-z plane [61].

posite ends. A bias voltage is applied to the p^+ implant which depletes the bulk of free charge carriers. When a charged particle traverses the depleted bulk, it produces electron-hole pairs. The electrons drift under the applied voltage to the n^+ side, which is highly segmented into 47,232 distinct pixels. 16 front-end chips are bump-bonded to a sensor, each of which is responsible for the readout of 2,952 pixels. Upon receipt of a trigger signal, the hits stored in these 16 front-end chips are read by a module control chip and passed to the central ATLAS data acquisition (DAQ) system. The sensor, 16 front-end chips, and module control chip constitute a module.

The majority of the ATLAS pixels are 50×400 μm^2, with some slightly larger 50×600 μm^2 pixels. A total of 1,744 modules are arranged into three concentric barrel layers centered on the IP, and two end-caps with three disks each covering the high $|\eta|$ region. This is shown in Figure 2.4. The innermost of the barrel layers is referred to as the "b-layer." The barrel layers are located at radii of 5, 9, and 12 cm. The disks are located 50, 58, and 65 cm from the interaction point. The high granularity and closeness to the interaction point leads to good momentum and impact parameter resolution. The impact parameter is the distance of closest approach of the track to the primary vertex. Good impact parameter resolution is important for vertex reconstruction

and b-tagging, the identification of jets originating from b quarks. In the barrel region, the spatial resolution in the transverse (longitudinal) plane is 19 (105) μm. The ATLAS Pixel Detector has a $> 98.7\%$ hit efficiency, including problematic and disabled modules, and a noise occupancy on the order of 10^{-10} per event [54, 63].

Silicon Strip Detector

Similar to the Pixel Detector, the silicon strip detector (SCT) is a semiconductor tracker. Whereas the pixels are highly segmented in two dimensions, the SCT is composed of strips which are segmented in a single dimension only. For this reason, SCT modules are double-sided, with a set of strips on each side rotated by 40 mrad relative to one another. This design allows the detection of space-points (with some ambiguity) when hits are registered in both sets of strips. Six chips on both sides of the module are used for binary readout. The strips have a 99.75% hit efficiency, and noise occupancy less than 5×10^{-4}.

As shown in Figure 2.4, modules are arranged in 4 concentric cylinders in the barrel region and nine disks each in the two end-caps. Over the fiducial coverage of the ID, this arrangement provides at least four precision space-point measurements per track. In the barrel layers, strips are rectangular with a length of 6 cm and width of 80 μm. In the end-caps, the strips are trapezoidal with a length of 6 cm and average width of 80 μm. The width increases with radial distance from the beam. The SCT by itself can reconstruct isolated leptons with $p_T > 5$ GeV with a $> 95\%$ efficiency, and 30% precision up to $p_T = 500$ GeV [54, 64].

Transition Radiation Tracker

The Transition Radiation Tracker (TRT) is a gaseous straw tube tracker which provides many position measurements along a particle track. Straw drift tubes with a 4 mm inner diameter are filled with 70% Xe, 27% CO_2, and 3% O_2. Along their center is a tungsten wire with a 31 μm diameter, which serves as an anode. The straw wall is kept at -1.5 kV relative to the wire. When a charged particle passes through the tube it loses energy through ionization of the gas. The liberated electrons drift towards the anode wire, where avalanche multiplication results in a gain of $\sim$25,000 and a measurable signal. The distance of the track from the anode is estimated from time of flight information. The straws are also surrounded by polypropylene-polyethylene fiber, which can produce transition radiation when traversed. These photons lead to a much larger signal than that produced through ionization, thus separate low and high threshold discriminators can be used to identify electrons.

The signal time-over-threshold is related to dE/dx, and can also be used for particle identification. The anode wire is connected directly to the front-end electronics. The hit efficiency depends on the distance from the track to the anode, but peaks at 94%.

As shown in Figure 2.4, the TRT consists of three concentric cylinders each with 32 modules covering $|\eta| < 1$, and two end-caps covering $1 < |\eta| < 2$. The straws of the barrel layers run parallel to the beam. The end-caps are made up of 20 wheels. Each wheel contains eight successive layers of radially oriented straw tubes. For tracks with $p_T > 0.5$ GeV and $|\eta| < 2$ at least 36 straws are traversed, except in the transition region between barrel and end-cap where as few as 22 straws may be traversed. For electrons with $p_T > 2$ GeV, this yields 7-10 high threshold hits. The SCT has a position resolution of 130 μm for tracks with $p_T > 0.5$ GeV, and enhances pattern recognition and improves the overall momentum resolution [54, 65].

2.2.3 Calorimeter

The ATLAS calorimetry system is designed to accurately measure the energy of electromagnetic (EM) and hadronic particles. The system consists of four separate calorimeters, shown in Figure 2.5. A high granularity liquid argon (LAr) calorimeter provides EM calorimetry up to $|\eta| < 3.2$. A scintillating-tile calorimeter provides hadronic calorimetry up to $|\eta| < 1.7$. Additional LAr end-cap calorimeters provide hadronic calorimetry in the range $1.5 < |\eta| < 3.2$. Hadronic and EM calorimetry in the range $3.1 < |\eta| < 4.9$ is provided by the forward LAr calorimeters. The calorimeters have full ϕ coverage.

All of the ATLAS calorimeters are sampling calorimeters. They consist of alternating layers of absorber and active medium. The absorber medium causes the primary particle to shower, producing a number of secondary particles. The ionization energy of the secondary particles is then measured in the active medium, providing a signal proportional to the total charged particle track length in the active medium. The shower evolution in the absorber layers continues until all secondaries lack sufficient energy to produce additional particles. There must be enough layers of absorber and active medium to contain this showering process in order to achieve accurate energy measurement [54].

Energy resolution is typically parametrized according to

$$\frac{\sigma_E}{E} = \frac{a}{\sqrt{E[\text{GeV}]}} \oplus \frac{b}{E[\text{GeV}]} \oplus c, \tag{2.6}$$

where the first term represents the stochastic contribution to mis-measurement, the second term represents a contribution due to electronic and pileup noise,

and the third term represents the contribution from local non-uniformities in the calorimeter response. The energy resolution of the four ATLAS calorimeters is summarized in Table 2.2.

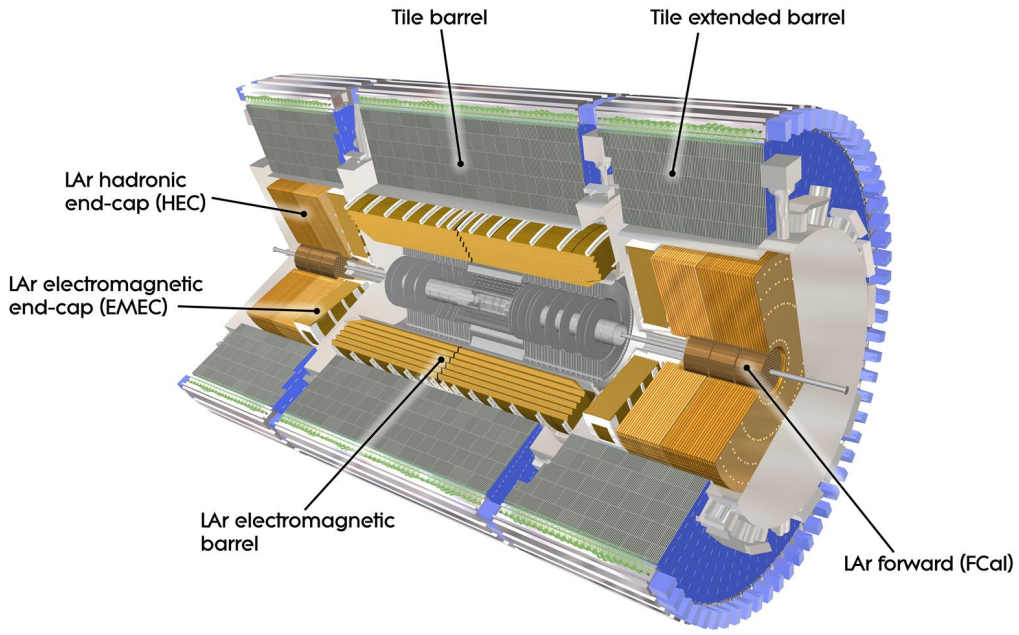

Figure 2.5: The ATLAS Calorimeter. Calorimetry in the barrel region is provided by a LAr EM calorimeter and scintillating tile hadronic calorimeter. LAr end-cap and forward calorimeters provide both EM and hadronic calorimetry for large $|\eta|$ [60].

Electromagnetic Calorimeter

Precision measurement of electron and photon energy is provided by the LAr EM calorimeter (EMC). The absorber medium is lead and the active medium is LAr. Between slabs of lead, charged particles ionize the LAr. The free electrons drift under the influence of an applied high voltage. They are collected on a central electrode layer, creating an ionization current [70]. The drift time is approximately 450 ns for an operating voltage of 2 kV.

The EM calorimeter consists of a barrel covering $|\eta| < 1.475$ and two end-caps covering $1.375 < |\eta| < 3.2$. An accordion geometry was chosen which provides full ϕ symmetry without any gaps in coverage. The region covering

Calorimeter	Particle Type	a [%]	c [%]
EMC	electron	10	0.17
Tile	hadron	56 ± 0.4	5.5 ± 0.1
HEC	electron	21.4 ± 0.1	≈ 0
	hadron	70.6 ± 1.5	5.8 ± 0.2
FCAL	electron	28.5 ± 1.0	3.5 ± 0.1
	hadron	94.2 ± 1.6	7.5 ± 0.4

Table 2.2: Summary of energy resolution for EMC, Tile calorimeter, HEC, and FCAL [54, 66–69]. The noise term in Equation 2.6 is negligible at typical energies, thus the noise constants b have been omitted.

$|\eta| < 2.5$ is designed for enhanced precision. In this region the calorimeter depth is segmented in three sections, compared to two at higher $|\eta|$. The first layer is highly segmented in η, as fine as $0.025/8 \times 0.1$ in $\Delta\eta \times \Delta\phi$. The second layer collects the majority of the shower energy, and has segmentation of 0.025×0.025. The third layer contains the remainder of the shower, and has segmentation of 0.05×0.025. An η-ϕ tower showing the 3 layers, their depth and segmentation in η-ϕ, and the accordion geometry is shown in Figure 2.6. A presampler covers the region $|\eta| < 1.8$, which samples the energy lost in front of the calorimeter. The total barrel thickness varies in $|\eta|$ between 22 and 30 radiation lengths (X_0).

The EMC electron energy resolution was tested at $|\eta| = 0.687$. Over an energy range from 15 to 180 GeV, it was found that $a = 10\%$ and $c = 0.17\%$. The barrel (end-cap) was also tested at 245 GeV (119 GeV), where $c = 0.5\%$ (0.7%) was observed. The measured noise term was $b = 14\%$, but this contribution is negligible for high energy electrons. The position resolution has also been measured, and was observed to be 50-60 mrad $/\sqrt{E\ [\text{GeV}]}$ [54, 66].

Tile Calorimeter

The tile calorimeter uses the iron flux return of the solenoid as the absorber and scintillating plastic tiles as the active material. Molecules within the plastic are excited by charged particles, which then rapidly de-excite by emitting photons on a nanosecond timescale. These photons are collected by wavelength shifting fibers and passed to photo-multiplier tubes (PMT), which amplify the signal.

Hadronic calorimetry is provided by the cylindrical tile calorimeter over the range $|\eta| < 1.7$, which surrounds the EMC. It consists of a barrel and two extended barrels, about 7.4 interaction lengths (λ) deep at $\eta = 0$. The tile calorimeter contains three radial sampling depths with varying granularity.

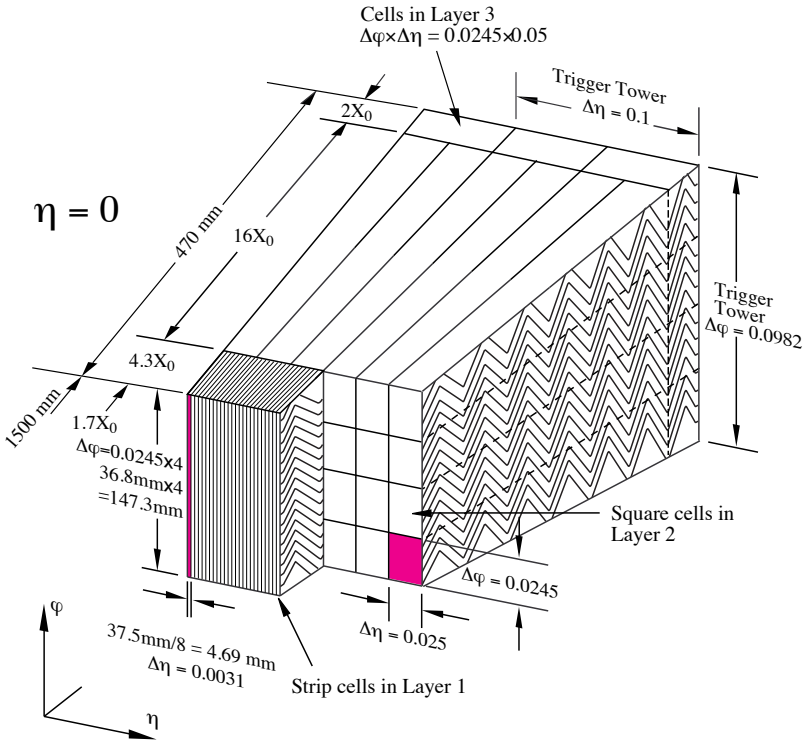

Figure 2.6: A tower of the LAr barrel EMC. The three layers are shown, along with their segmentation and depth in radiation lengths. The accordion geometry is also visible [54].

The first and second layers provide a total of 5.6λ at $\eta = 0$, and the granularity in $\Delta\eta \times \Delta\phi$ is 0.1×0.1. The third layer provides the final 1.8λ, and its granularity in $\Delta\eta \times \Delta\phi$ is 0.2×0.1.

In order to obtain accurate measurements of energy, the light yield of the individual scintillator tiles must be relatively uniform. The light yield was measured for a number of tiles and found to vary by only 1-2%. The fractional energy resolution was also measured over a range of hadron energies in beam tests. The 20-180 GeV beams were mostly composed of pions, kaons, and protons. For $|\eta| = 0.35$, the stochastic and non-uniformity parameters were found to be $a = (56 \pm 0.4)\%$ and $c = (5.5 \pm 0.1)\%$ respectively. The resolution was found to depend strongly on $|\eta|$. The effective calorimeter depth increases with $|\eta|$, therefore decreasing lateral leakage and improving resolution. For 20 GeV beams, the fractional resolution is 14.2% (13.0%) at $|\eta| = 0.25$ (0.55) [54, 67].

Hadronic End-Cap Calorimeter

The hadronic end-cap calorimeter (HEC) uses LAr as the active medium, and resides inside the same end-cap cryostat as the EM end-cap calorimeters (EMEC). However, the absorber is copper, and rather than the accordion geometry a flat-plate design is used. The HEC covers the region $1.5 < |\eta| < 3.2$. Each end-cap consists of two wheels, and each wheel is composed of 32 identical wedge shaped modules. 24 copper absorber plates, each 25 mm thick, make up the front wheel. The 8.5 mm gaps between plates are filled with LAr. The sampling fraction in the rear wheel is coarser, with 16 copper plates of 50 mm thickness. The LAr gaps are themselves divided into four separate drift zones of 1.8 mm width, for a drift time of 430 ns at nominal operating voltage. The granularity in $\Delta\eta \times \Delta\phi$ is 0.1×0.1 for $|\eta| < 2.5$, and 0.2×0.2 elsewhere.

The HEC is also capable of detecting muons and EM showers. The longitudinal segmentation allows differentiation between EM and hadronic showers. For electrons, the HEC was found to have fractional energy resolution with stochastic parameter $a = (21.4 \pm 0.1)\%$ and uniformity parameter compatible with zero. The fractional resolution for pions was also measured, which characterizes the hadronic capabilities. Stochastic parameter $a = (70.6 \pm 1.5)\%$ and uniformity parameter $c = (5.8 \pm 0.2)\%$ were observed [54, 68].

Forward Calorimeter

The final component of the ATLAS calorimeter system is the forward calorimeter (FCAL). As implied by the name, it covers the far forward region, with $3.1 < |\eta| < 4.9$. This region receives a high particle flux, which

is accounted for in the design. Three modules make up each FCAL, the first of which is optimized for EM calorimetry and the remaining two for hadronic calorimetry. The EM modules use copper for the absorber, and the hadronic modules use mainly tungsten. All modules are 45 mm deep. A matrix of holes are drilled into the copper, which run parallel to the beam direction. Thin tubes are inserted into the holes, and coaxial rods are are inserted into the tubes, separated by a small gap. These rods serve as electrodes, and the small gaps between tube and rod are filled with LAr, the active medium.

The fractional energy resolution of the FCAL has been measured with electron and pion beams. For the electron beam, the measured stochastic term was $a = (28.5 \pm 1.0)\%$ and the uniformity term was $c = (3.5 \pm 0.1)\%$. For the pion beam, the measured stochastic term was $a = (94.2 \pm 1.6)\%$ and the uniformity term was $c = (7.5 \pm 0.4)\%$ [54, 69].

2.2.4 Muon Spectrometer

Muons are minimum ionizing particles, thus they deposit very little energy in the calorimeters. A dedicated muon spectrometer (MS), shown in Figure 2.7, is located outside of the calorimeters to precisely measure muon momenta from ∼3 GeV up to ∼3 TeV. Large super-conducting toroid magnets produce a strong magnet field which bends muon trajectories. Multiple position measurements are made by the muon spectrometer, allowing determination of the muon trajectory and momentum. Three cylindrical barrel layers provide coverage for small $|\eta|$, and three disks oriented perpendicular to the beam axis provide coverage for high $|\eta|$. The barrel radii are 5, 7.5, and 10 m. The Disks are located at $|z| = 7.4$, 10.8, 14, and 21.5 m from the interaction point. Both the barrel layers and disks can be seen in Figure 2.8.

The muon spectrometer consists of monitored drift tubes (MDT) and cathode strip chambers (CSC) which provide precision position measurements in the principle bending direction of the magnetic field, and cover the region $|\eta| < 2.7$. Resistive plate chambers (RPC) and thin gap chambers (TGC) are used for muon triggering and position measurement in both the principle bending direction and the orthognal direction, and cover the region $|\eta| < 2.4$. The muon spectrometer was designed to have a fractional p_T resolution of no more than 10% for 1 TeV muons [54].

Monitored Drift Tube Chambers

A drift tube consists of a 3 cm diameter Al tube filled with Ar and CO_2. A tungsten-rhenium anode wire with 50 μm diameter runs down the center of the tube at a potential of 3,080 V. A muon passing through the tube ionizes

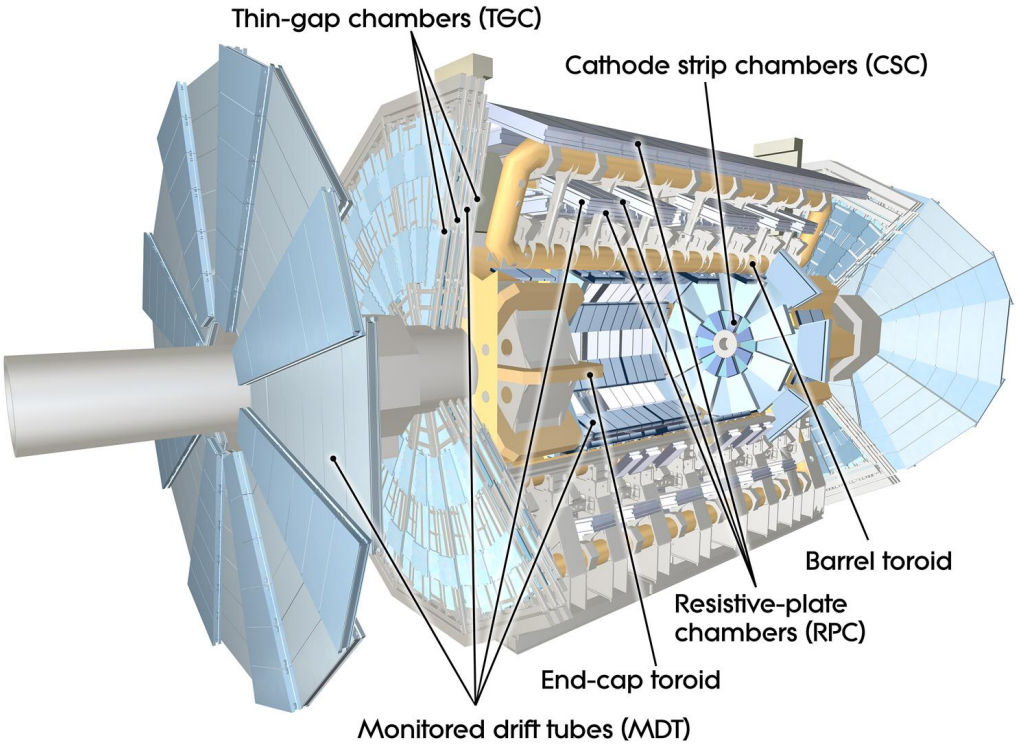

Figure 2.7: The ATLAS MS. MDTs and CSCs provide tracking up to $|\eta| < 2.7$. RPCs and TGCs provide the ability to trigger on high p_T muons up to $|\eta| < 2.4$ [60].

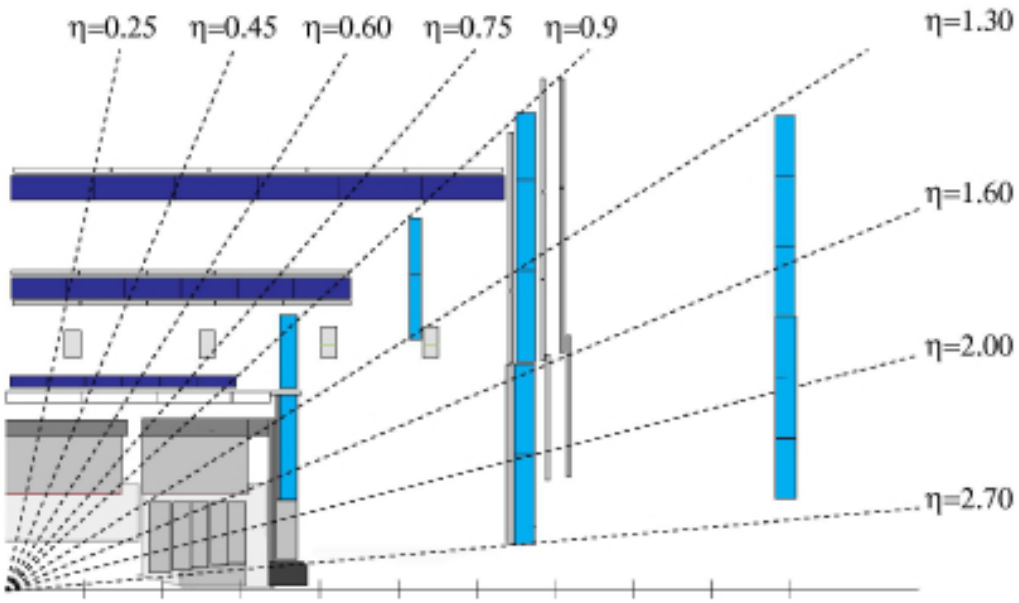

Figure 2.8: A Quadrant of the MS in the R-z plane [71].

the gas, and the free electrons drift to the anode wire creating a signal which is amplified and measured. The maximum drift time is 700 ns. A single tube has $\sim$80 μm resolution.

A MDT chamber consists of two groups of tube layers, referred to as multi-layers. In the innermost barrel and disk, these multi-layers are made of four layers of drift tubes, while the rest of the chambers use three layers of tubes. These chambers are arranged in three concentric barrels and three disks, shown in Figure 2.8, providing coverage up to $|\eta| < 2.7$. The three (four) tube multi-layers have a combined resolution of 50 (40) μm, and the multilayer pairs have combined resolution of 35 (30) μm. The design momentum resolution for a muon passing through three chambers is $\leq$10% for $p_T \leq 1$ TeV [54, 72].

Cathode Strip Chambers

In the high $|\eta|$ region of the muon spectrometer end-caps, MDTs are not capable of handling the counting rate. Therefore, the innermost end-cap disk uses cathode strip chambers over the radial space 881 mm $< R <$ 2081 mm, or equivalently $2 < |\eta| < 2.7$. CSCs are multiwire proportional chambers, with a high spatial and time resolution, and a higher rate capability than MDTs. Parallel anode wires run in the radial direction, sandwiched between two cathode planes. One cathode is segmented in the principle bending direction (perpendicular to the wires) and the other is segmented in the orthogonal direction. Muon traversal ionizes the gas between the two cathodes, leading to avalanche multiplication in the high field in the vicinity of the anode wires. This induces charge on the segmented cathodes, which is amplified and measured. Due to the segmentation of both cathodes, both the η and ϕ coordinates can be measured.

As shown in Figure 2.7, each CSC end-cap consists of two disks roughly 7 m from the IP. The outer disk is composed of eight large CSC chambers. Coverage gaps between large chambers are filled in by the inner disk, which consists of eight smaller CSC chambers. Each chamber consists of four CSC planes which give four independent measurements in η and ϕ for each track. The cathode segmentation is different in the large and small chambers. In the large (small) chambers the cathode pitch is 5.567 (5.308) mm in the principle bending direction and 21 (12.92) in the perpendicular direction, for a chamber resolution of $\sim$40 μm and $\sim$5 mm respectively [54, 73].

Trigger Chambers

The muon spectrometer also includes trigger chambers for trigger on low and high p_T muons, covering the range $|\eta| < 2.4$. These chambers must

provide fast muon track information, enabling momentum discrimination. In the barrel region ($|\eta| < 1.05$), three layers of resistive plate chambers were chosen, which provide good spatial and time resolution with adequate rate capability. In the end-caps ($1.05 < |\eta| < 2.4$), where a high rate capability is necessary, four layers of thin gap chambers were selected. Both the barrel layers and disks are shown in Figure 2.8. In both regions, triggers consist of fast coincidences between the last three layers traversed by a muon track, above a given p_T threshold. The RPCs also complement the ϕ measurement of the MDTs, which is particularly coarse in this non-bending direction.

The RPCs are gaseous parallel electrode-plate detectors. Two parallel, resistive plates are separated by a distance of 2 mm. A nominal potential of 9.8 kV is maintained between plates, creating a high electric field in the gas filled region between plates. Muons traversing this gap ionize the gas, leading to avalanche multiplication and a measurable signal. Two sets of these plates are stacked on top of each other, forming a unit. A side-by-side pair of units makes up a chamber. The chambers are arranged in three concentric barrel layers surrounding the IP. Each chamber has a design resolution of 10 mm in both the principal bending and orthogonal direction [54, 74].

The TGCs are multi-wire proportional chambers. Two copper plates are separated by a gas gap, with wires running along the middle of the gap. One plate is segmented perpendicular to the wires, from which signal is read out, providing one coordinate measurement. The wires measure the orthogonal coordinate. The drift time is under 25 ns. Two or three of these chambers are stacked to create a unit. Units are arranged in four layers of two circular disks. The outer disk covers the region $1.05 < |\eta| < 1.92$, while the inner disk covers the region $1.92 < |\eta| < 2.4$. Each chamber has a design resolution of 2-6 mm in the bending direction and 3-7 mm in the orthogonal direction [54, 74].

2.2.5 Magnet System

The ID and muon spectrometer determine particle momentum by measuring the deflection of tracks within a high magnetic field. The magnetic field for the ID is provided by the central solenoid. In the barrel region, a barrel toroid provides the bending power for the muon spectrometer, and in the end-caps the bending power is supplied by end-cap toroids. In order to bend the trajectory of high p_T particles sufficiently, intense fields are necessary. An overview of the magnet system is shown in Figure 2.9.

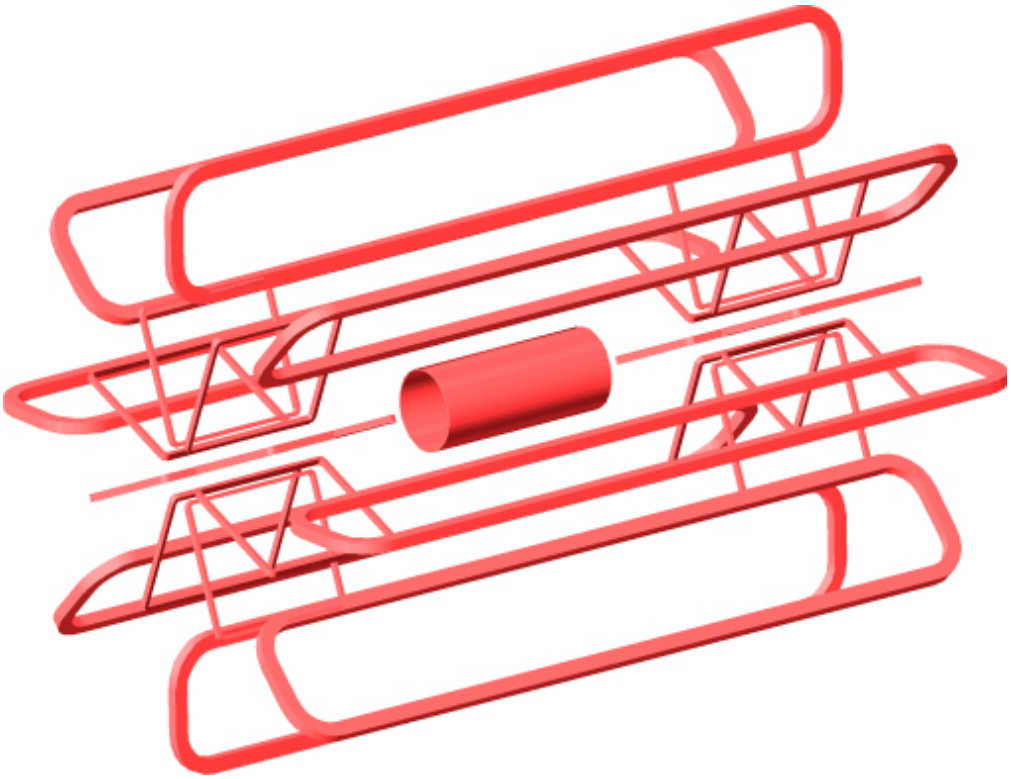

Figure 2.9: The ATLAS magnet system. The barrel solenoid provides bending power for track p_T measurement in the ID. Barrel and end-cap toroids provide bending power for track p_T measurement in the MS [75].

Solenoid Magnet

The central solenoid magnet provides bending power for ID momentum measurements. It operates at 4.5 K, and provides a 2 T field at nominal operational current (7.73 kA), directed along the beam axis. This represents 40 MJ of stored energy. In order to maintain optimal perforce of the calorimeters, the solenoid presents minimal material thickness in front of the calorimeters. At normal incidence, it represents $\sim$0.66 X_0. The inner (outer) diameter of the solenoid is 2.46 (2.56) m, and the axial length is 5.8 m [54].

Toroid Magnets

A system of toroidal magnets provide the bending power for the muon spectrometer. The barrel toroids provide magnetic field for the central region ($|\eta| \lesssim 1.65$). Eight racetrack-shaped coils surround the IP with eight-fold azimuthal symmetry. The inner (outer) radius of the system is 9.4 (20.1) m, and the axial length is 25.3 m. The nominal operating current is 20.5 kA, representing 1.1 GJ of stored energy. A pair of toroidal end-cap magnet systems provide bending power for the muon spectrometer end-caps ($|\eta| \gtrsim 1.3$). The layout posseses the same eight-fold azimuthal symmetry as the barrel toroids. The inner (outer) diameter of the end-cap toroids is 1.65 (10.7) m, and the axial length is 5 m. Like the barrel toroids, the nominal operating current is 20.5 kA, but the stored energy is lower at 2×0.25 GJ. The nominal operating temperature of both the barrel and end-cap toroids is 4.6 K [54].

2.2.6 Forward Detectors

There are also three forward detectors associated with ATLAS. The LUCID and ALFA detectors are important for luminosity measurement. The Zero Degree Calorimeter is primarily used during heavy-ion runs.

LUCID

LUCID (LUminosity measurement using Cerenkov Integrating Detector) is a Cerenkov detector designed to measure the relative luminosity delivered to ATLAS in real time. It consists of two detectors located at $|z| = 17$ m from the IP. They cover the region $5.6 < |\eta| < 6.0$. A series of 20 highly-reflective 15 mm diameter aluminium tubes filled with C_4F_{10} gas surround the beam, pointing toward the IP. Particles produced in inelastic pp collisions enter the tubes and produce Cerenkov light. These photons exit the back of the tubes where PMTs are located. The signal from these PMTs is amplified and passed to a discriminator. Signals above the discriminator threshold are considered

hits. The number of observed hits in LUCID is proportional to the number of interactions in a given bunch crossing. With an appropriate calibration, the relative luminosity measured by LUCID can be converted to an absolute luminosity [54, 76].

ALFA

ALFA (Absolute Luminosity For ATLAS) is designed for measuring the absolute luminosity delivered to ATLAS during special high $\beta^\star$ runs. It consists of four stations located at $|z| = 240$ m from the IP. At each station is a Roman pot connected to the beam pipe with bellows. These bellows allow the Roman pots, which are retracted from the beam during normal operations, to be moved very close to the beam, as close as 1 mm. On each side of the interaction point, one Roman pot approaches the beam from below and one approaches from above. Each Roman pot houses a scintillating fiber tracker. The trackers measures the x and y coordinates of elastically scattered protons, which are deflected by $\sim$3 μrad from the beam direction. This enables a determination of the forward elastic scattering amplitude, which is related via the optical theorem to the total cross section. From this, the absolute luminosity can then be extracted. This technique can't be used during actual physics runs, but can be used to calibrate LUCID [54, 77].

Zero Degree Calorimeter

The Zero-Degree Calorimeter (ZDC) is designed primary for heavy-ions runs, where its main purpose is to aid in the determination of collision centrality. It measures the number of very forward neutrons produced in each collision, from which the centrality can be extracted. In early pp runs, it also provided an additional minimum bias trigger. It is located at $|z| = 140$ m from the IP, covering the region $|\eta| > 8.3$. On each side of the interaction point there are four ZDC modules, one for EM ($\sim$29 X_0) and three for hadronic (1.14 λ each) measurements. The EM modules consists of 11 tungsten plates with faces perpendicular to the beam. 96 quartz rods running parallel to the beam are inserted into the plates. Cerenkov light produced by incident particles are read out by PMTs linked to the rods. The hadronic modules are similar, with a factor of four reduced granularity. The time resolution of each detector is $\sim$100 ps, from which the longitudinal vertex position can be determined with a resolution of $\sim$3 cm [54].

2.2.7 Trigger and Data Acquisition

The data aquisition (DAQ) system controls the trigger processing chain and allows configuration, control, and monitoring of the entire ATLAS detector. The collision rate within ATLAS will eventually reach 40 MHz. Three successive levels of triggering reduce the rate of selected events to about 400 Hz for permanent storage. The level 1 (L1) hardware trigger accepts events with high E_T energy deposits in the calorimeters or hit patterns in the muon trigger chambers consistent with high p_T tracks, reducing the event rate to 75 kHz. Regions of interest (RoI) identified by the L1 trigger are passed to the level 2 (L2) trigger. A L2 trigger decision is made from the detector data in these RoIs, which further reduces the event rate to 5 kHz. Events passing the L2 trigger are sent to the event filter (EF), a processor farm running the ATLAS reconstruction software. Full events are built and a final trigger decision is made, reducing the event rate to 400 Hz. The L1 trigger uses only reduced granularity information from the calorimeters and MS. The L2 and EF software triggers, jointly referred to as the high-level trigger (HLT), use the full granularity and precision of the calorimeters and MS, as well as information from the ID [54, 78].

Level 1 Trigger

The L1 trigger performs the initial event selection and determines RoIs for the L2 trigger decision. It uses reduced granularity information from the calorimeters and muon trigger chambers. The L1 trigger decision is based on the multiplicity of high E_T objects. While the L1 decision is being made, all detector information must be stored in memory on the front-end electronics of the various detector components. This limits the trigger latency to $\lesssim 2.5$ μs.

The calorimeter trigger uses 7,000 reduced granularity trigger towers from the EM and hadronic calorimeters. It identifies electron/photon, tau, and jet candidates, as well as events with large $\not\!\!E_T$ and scalar E_T sums. The muon trigger is based on inputs from the RPC and TPG chambers. It identifies coincidences of hits consistent with high p_T muon trajectories originating at the IP, and quickly estimates the muon p_T. The calorimeter and muon triggers determine the multiplicity of each object type above six programmable E_T thresholds. This information is then reported to the central trigger processor (CTP) which makes the final L1 trigger decision.

A trigger menu is defined with up to 256 trigger items. Each trigger item is a combination of trigger conditions. A trigger condition is a requirement on the multiplicity of an object type above one of the six programmable E_T thresholds, or a combination of such objects. The ultimate L1 trigger decision

is the logical OR of all trigger items. If the L1 trigger is accepted, detector data is transferred from readout drivers (ROD) to the readout system (ROS), where it is stored temporarily until the HLT trigger decision is made. The RoI information found at L1 is sent to the RoI builder [54].

High-Level Trigger

The HLT is a series of two software based triggers, the L2 and EF triggers. The event rate is reduced from the L1 rate of 75 kHz to 3.5 kHz after the L2 trigger, and 400 Hz after the EF trigger [59]. Unlike the L1 trigger, the ID information and the full detector granularity are used by the HLT. This enhances the E_T resolution and particle identification. Events passing the EF trigger are stored permanently and reconstructed offline.

The RoIs identified by the L1 trigger are passed to the RoI builder. The RoI builder requests information from the ROS which is relevant to the RoI's, typically about 1-2% of the event data. After building the RoIs, a L2 trigger accept decision is made. This generally takes about 40 ms. If the event satisfies the L2 trigger conditions, the event gets fully assembled on an event-builder node. The EF then evaluates the entire event in $\sim$4 s and makes a final trigger determination. If the event is accepted by the EF, it is transferred to permanent storage for offline reconstruction.

Both HLT trigger decisions are made in a similar manner. A series of feature extraction algorithms run on the RoI or event data, depending on the trigger step. These algorithms identify features in the event, such as a track or calorimeter cluster. A series of hypothesis algorithms are then run on identified features, which asses if the feature meets a set of predefined criteria. If no signatures pass these hypothesis algorithms, the event is rejected. Otherwise, it is passed on to the next step in the trigger chain, EF or permanent storage [54, 79]

Chapter 3

Reconstruction

Ultimately, for each event selected by the HLT all position and energy measurements are read out from the ATLAS detector. It is the job of the reconstruction software to process the raw information and identify physics objects. Trajectories of charged particles, or tracks, are reconstructed from the position hits in the ID. From the collection of tracks in an event, the primary and any secondary vertices are reconstructed. Electrons, photons, and jets are reconstructed from clusters of energy deposited in the calorimeter. Tracks matched to clusters of EM energy deposits are reconstructed as electrons. Muons are reconstructed from MS tracks extrapolated and matched to an ID track.

3.1 Track Reconstruction

Two complimentary approaches are used to find charged particle trajectories in the ID [80]. An inside-out procedure is used first to find the majority of tracks present in an event, followed by an outside-in procedure which can find additional tracks.

The inside-out procedure starts with the Pixel Detector, then successively incorporates information from the SCT and TRT. Three dimensional space-points are first determined in the Pixel Detector and SCT. This is a simple task for the pixels, where the hits are already localized in three dimensions. For the SCT, the pairs of rotated strips which constitute a module are used to determine a localized space-point in three dimensions. Track seeds are then found by considering pairs of pixel space-points. This step includes an optional constraint on the allowed vertex position in z. The track seeds are extrapolated out from the Pixel Detector into the SCT. As a track seed is extrapolated further from the IP, nearby hits are associated to the track, after

which the track is refit before continuing the extrapolation. In this way the track is updated progressively, and outlying space-points, identified by their contribution to the track χ^2, can be excluded from the track.

Poor track candidates must be discarded. Also, the many ambiguities arising from shared hits between track candidates must be resolved. Track candidates are scored according to the likelihood they describe actual particle trajectories. Different characteristics result in positive or negative contributions to a track candidate score. Hits provide a positive contribution and holes, the lack of a hit where one is expected, provide a negative contribution. The contribution is greater for Pixel hits/holes than those in the SCT. An iterative procedure is then performed where hits shared between tracks are assigned to the highest scoring track candidate, and the track candidates are re-fit and re-scored with this new assignment. Ultimately, track candidates falling below a quality threshold are discarded. The remaining track candidates are then extrapolated into the TRT. All TRT hits compatible with an extrapolated track candidate are associated to it and the track candidate is re-fit and re-scored. If the score of the new track candidate is worse than prior to inclusion of the TRT hits, outliers are iteratively removed from the track until the score has improved.

Some track seeds can be missed by this procedure, and some tracks simply lack seeds in the Pixel Detector, such as charged daughters from long lived particle decays and electrons from photon conversions. An outside-in procedure is used to find tracks which may have been missed by the inside-out approach. To reduce CPU usage, only space-points which are not already associated to tracks are used. This procedure starts in the TRT. Since the TRT tubes provide space points localized in only two dimensions, global pattern recognition is performed in projective planes (R-ϕ in the barrel region and z-ϕ in the endcaps). During the global pattern recognition, drift time information is ignored and space-points are assumed to lie at the center of the tubes. Each space-point is assumed to lie on a track originating at the IP. For each space-point, a variety of tracks with different momenta will fulfill this requirement. A range of allowed momenta and the associated azimuthal coordinate of the tracks extrapolated to the origin ϕ_0 are placed in a two dimensional histogram. Local maxima are then found, each of which corresponds to a track candidate. These track segments are re-processed using drift time information to refine the fit. These track candidates are back-tracked into the SCT and the Pixel Detector. As additional hits are associated to the track candidates during this back-tracking, the track is iteratively re-fit and outliers are dropped.

3.2 Vertex Reconstruction

From the collection of tracks in an event, vertices are reconstructed. At design luminosity, there will be on average 24 pp interactions per bunch crossing [54]. Most of these interactions correspond to soft minimum bias interactions, and are referred to as in-time pileup. In the data collected for this analysis, an average of 5.6 interactions occurred per bunch crossing [76]. Thus, in a typical event many primary vertices, spread out along z, must be reconstructed. Secondary vertices displaced transverse to the beam direction are also possible, resulting from photon conversion and long-lived particle decays. These must be reconstructed as well.

There are essentially two stages of vertex reconstruction, vertex finding and fitting. In many algorithms these stages are highly intertwined. Vertex finding consists of associating tracks to particular vertex candidates. Vertex fitting is the determination of vertex position and covariance matrix from the collection of associated tracks. The default ATLAS primary vertex reconstruction algorithm involves an iterative "finding-through-fitting" approach [81]. All tracks likely to originate from the interaction region are associated to a single primary vertex candidate. This vertex candidate is fit, and any outlier tracks are removed. These outlier tracks are then used to seed additional primary vertices and a simultaneous fit of all vertex candidates is performed. During this iterative procedure the candidates compete for the association of tracks.

There is also an alternative "fitting-after-finding" approach. Clusters of tracks in the longitudinal direction are used as candidate seeds. These clusters are iteratively fit, rejecting outlier tracks after each iteration. Unlike the default algorithm, the number of vertex candidates does not grow and the maximum number is fixed by the initial seeding process. In both cases, a number of vertex fitting algorithms are available. Primary vertices are reconstructed with 10-12 (35-55) μm resolution in the transverse (longitudinal) direction [81]. Figure 3.1 shows an example event after track and vertex reconstruction. There are four primary vertices marked by red ellipses.

Secondary vertices arise from photon conversion and long-lived particle decay. These vertices are typically reconstructed by exploiting assumed properties of the interaction and applying kinematic constraints during the vertex fit. The reconstruction of photon conversion vertices begins by collecting electron tracks, using the electron identification capability of the TRT. The massless nature of the photon requires the electron-positron pair from conversion to have a common direction at the location of production. Therefore, pairs of electron tracks are formed with small distance of closest approach and small initial angular separation. The vertices formed from these track pairs are then fit, assuming collinearity at the vertex position. This allows a radial reso-

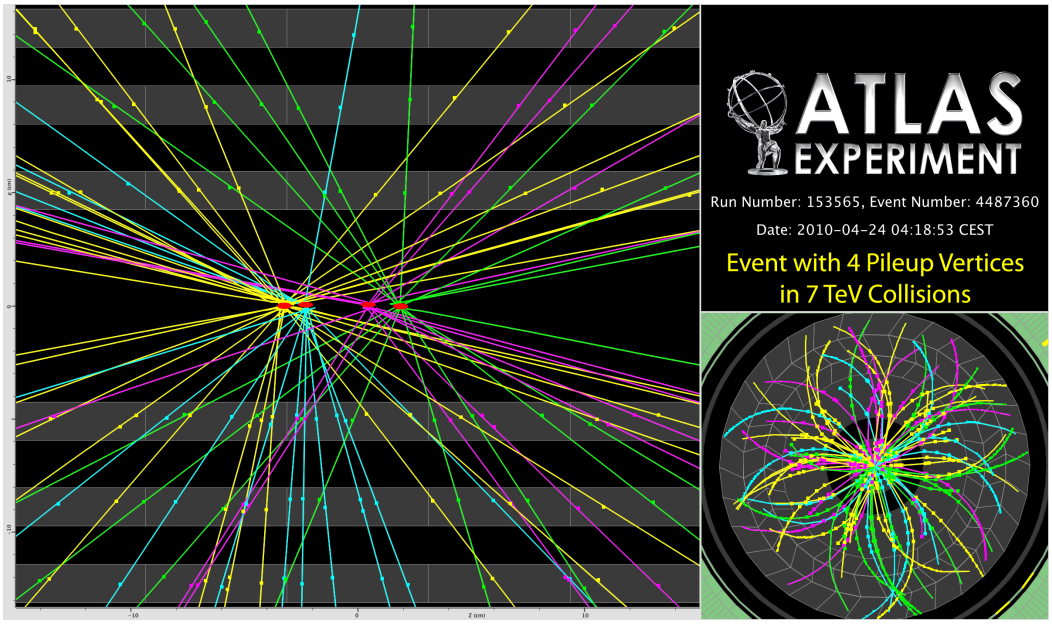

Figure 3.1: The result of track and vertex reconstruction for an event with four primary vertices, shown in the r-z plane (left) and R-ϕ plane (right). Hits and tracks are represented by colored dots and lines respectively. Vertices are shown as red ellipses, enlarged for visibility [61].

lution of ∼7 mm in the ideal case, with a large degradation possible due to bremstrahlung. Vertices from long-lived neutral particles are reconstructed in a similar manner, with a mass constraint applied during the fit rather than an angular constraint. Since the decay products emerge with a non-zero opening angle, and do not typically undergo bremstrahlung, the resolution is much better, typically ∼0.3 mm. For both photon conversion and long-lived decays, the resolution depends strongly on the radial distance of the interaction from the IP. The further out the interaction occurs, the fewer precision tracking measurements are available for reconstruction.

Vertex reconstruction within jets is particularly important in the identification of heavy-flavor and τ leptons. There are two common techniques to identify vertices from b-hadron electroweak decays. Both techniques begin by identifying displaced tracks. The typical b-hadron decay produces a c-hadron, which then itself decays. The first, a topological technique, assumes the primary, b, and c vertices all lie on the flight axis of the b-hadron. Track clusters are then searched for along this flight path, reducing a three dimensional clustering problem to a single dimension. A second, inclusive technique simply attempts to reconstruct a single vertex from the collection of displaced tracks. Both methods provide similar performance. Radial resolution of ∼400 μm is achievable, with a large tail [81].

3.3 Jet Reconstruction

Jet reconstruction is the process of identifying jets from the deposits of energy in the calorimeter cells. The individual cells are first grouped to form clusters. From these clusters, jets are reconstructed using one of many available jet algorithms. The calculated jet energy must then be corrected to account for several detector effects. Electrons, photons, and taus produce calorimeter energy deposits and are therefore typically reconstructed as jets as well as their actual object type. Therefore, an overlap removal procedure must be applied to discard these jets.

The ATLAS calorimeters are finely segmented in both the longitudinal and transverse directions. Incoming particles deposit energy in a number of calorimeter cells. Clustering is the process of combining the energy deposition in nearby cells into a single energy cluster, whose energy is equal to the sum of the energies of the individual cells. ATLAS uses a topological algorithm for this purpose with two basic steps, cluster making and splitting [82]

The cluster making step begins by finding all calorimeter cells with significant energy deposition. These seed cells must have a signal to noise ratio of at least four, where the noise is the η-dependent RMS of electronics noise

and pileup noise added in quadrature. A protocluster is formed for each seed cell. Neighboring cells with signal to noise ratios of at least two are iteratively added to the protoclusters, where neighbor is typically defined to include cells in adjacent calorimeter layers. If any of these cells neighbor two or more protoclusters, the protoclusters are merged. Finally, all cells neighboring the protocluster are added regardless of their signal to noise ratio. These protoclusters then undergo a splitting procedure to separate nearby showers into distinct protoclusters. The protoclusters are searched for local maxima above a certain threshold. Each local maximum then serves as a seed cell, and the clustering procedure is repeated with only those cells already selected. This time, no thresholds are imposed and no merging is performed. Rather than merging protoclusters with a common cell, these cells are shared. The relative contribution to each protocluster depends on the distance to each protocluster centroid and the procluster energies. At this point, the remaining protoclusters are promoted to clusters. The energy of a cluster is equal to the sum of the energies of the associated cells, the mass is defined as zero, and the η, ϕ position is defined as the average η, ϕ of all cells weighted by energy.

The definition of a jet is somewhat ambiguous. Many different algorithms exist which reconstruct jets and the results vary from one algorithm to the next. ATLAS uses the anti-k_t algorithm, which belongs to the class of sequential recombination jet algorithms [83]. These algorithms start by defining a "distance" measure between entities i and j

$$d_{ij} = \min\left(p_{T_i}^{2n}, p_{T_j}^{2n}\right)\frac{\Delta_{ij}^2}{R^2}, \tag{3.1}$$

and between entity i and the "beam"

$$d_{iB} = p_{T_i}^{2n}, \tag{3.2}$$

where $\Delta_{ij}^2 = (y_i - y_j)^2 + (\phi_i - \phi_j)^2$, R is a radius parameter, and n is a parameter which sets the power of the transverse momentum scale relative to the geometrical distance. The term "beam" is a bit misleading, as the quantity d_{iB} has nothing to do with the proton beams, depending only on entity i itself.

The distance between all entities is calculated. If the smallest distance between any two entities is a d_{ij}, those two entities are combined. If the smallest distance is a d_{iB}, then entity i is considered a jet and removed from the list of entities. The distances are then recalculated and this process is repeated until no entities remain.

A comparison of three important jet algorithms is shown in Figure 3.2. The anti-k_t algorithm is defined by $n = -1$, whereas n values of 0 and 1

correspond to the Cambridge/Aachen [84] and k_t [85] algorithms respectively. The k_t and Cambridge/Aachen algorithms form highly irregular shaped jets. In the anti-k_t algorithm, due to the dependence on p_T^{-2} in Equation 3.1, the clustering order is determined primarily by the hardest clusters in an event. Therefore, jet shapes are relatively unaffected by soft radiation and jets tend to be essentially conical. If a high p_T cluster is isolated from other high p_T clusters, a nearly conical jet will result centered on the high p_T cluster and containing any low p_T clusters within a radius of R. If two high p_T clusters are located within a distance of $R < \Delta_{ij} < 2R$, two jets are reconstructed which cannot both be conical. They will be nearly conical except in the overlap region, which will be associated to one jet or the other depending on the p_T of both jets. If there are two high p_T clusters within a distance $\Delta_{ij} < R$, a single jet is reconstructed with a somewhat irregular shape.

The jet four-momentum is defined as the sum of the four-vectors of the clusters associated to the jet. Due to calorimeter non-compensation and various other detector effects, the reconstructed jet energy is not equal to the sum of the energies of the incident hadrons. The calorimeters reconstruct energy at the EM scale, which correctly describes the energy of an EM shower. But the calorimeters have a lower response to hadronic showers, so the measured energy must be corrected to the jet energy scale (JES). A four stage correction is applied in ATLAS to correct the jet energy and position as measured by the calorimeter [86, 87]. First, the average energy due to pileup interactions is subtracted from the measured jet energy according to

$$E_T = E_T^{meas} - \mathscr{O}(\eta^{meas}, N_{PV}, \tau_{bunch}), \tag{3.3}$$

where E_T^{meas} and η^{meas} are the transverse energy and pseudorapidity as measured by the calorimeter, N_{PV} is the number of reconstructed primary vertices, and τ_{bunch} is the bunch spacing. The offset correction $\mathscr{O}(\eta^{meas}, N_{PV}, \tau_{bunch})$ is measured in minimum bias data and corrects jet energy on average to account for energy deposited by pileup interactions in the region of η-ϕ occupied by the jet. Next, the jet four-momentum is corrected to account for the location of the jet origin. Up to this point, it has been assumed that the jet was produced at the geometric center of the detector. The jet momentum is therefore corrected using the primary hard-scattering vertex as the jet origin, and all kinematic observables are recalculated. The jet energy is then brought from the EM scale to the JES. The jet energy response is defined as

$$\mathscr{R}_{EM}^{jet} = \frac{E_{EM}^{jet}}{E_{truth}^{jet}}, \tag{3.4}$$

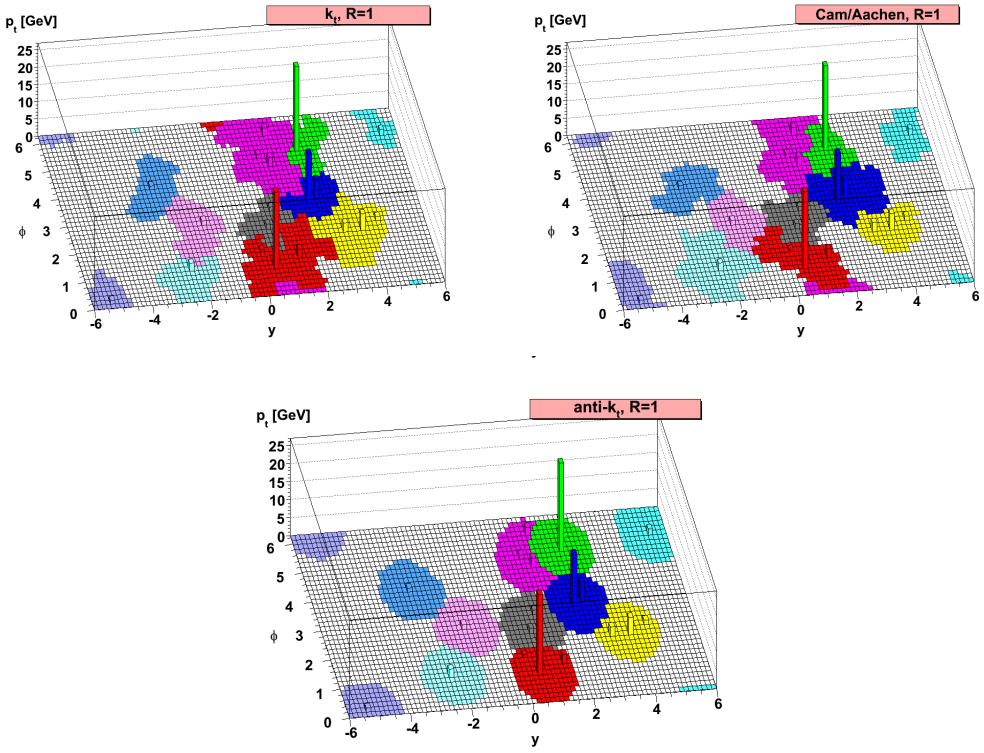

Figure 3.2: A comparison of jet algorithms for a typical event, with a few high p_T clusters and many soft clusters distributed in ϕ-y space. The results for the k_t (left), Cambridge/Aachen (right), and anti-k_t (bottom) jet reconstruction algorithms are shown. The shape of jets reconstructed with the anti-k_t algorithm are far more regular than those reconstructed with the other algorithms [83].

where E^{jet}_{EM} is the jet energy measured at the EM scale and E^{jet}_{truth} is the true energy of the particles making up the jet. This ratio is measured in simulated data, described in Chapter 4, binned in E^{jet}_{truth} and η^{meas}. For each bin, $\langle \mathscr{R}^{jet}_{EM} \rangle$ is defined as the peak position of a Gaussian fit to the $E^{jet}_{EM}/E^{jet}_{truth}$ distribution, and $\langle E^{jet}_{EM} \rangle$ is defined as the mean of the E^{jet}_{EM} distribution. A fit is then performed to the observed $\left(\langle \mathscr{R}^{jet}_{EM} \rangle, \langle E^{jet}_{EM} \rangle\right)$ values to obtain a continuous function $F_{calib}\left(E^{jet}_{EM}\right)$ for each η^{meas} bin, which relates the energy measured at the EM scale E^{jet}_{EM} to the energy measured at the JES E^{jet}_{EM+JES},

$$F_{calib}\left(E^{jet}_{EM}\right) = \sum_{i=0}^{N_{max}} a_i \left(\ln E^{jet}_{EM}\right)^i, \tag{3.5}$$

where the a_i are the fit parameters and N_{max} is chosen between 1 and 6 to obtain a good fit result. The JES value is then obtained by dividing the energy measured at the EM scale by this calibration function evaluated in the proper η^{meas} bin,

$$E^{jet}_{EM+JES} = \frac{E^{jet}_{EM}}{F_{calib}\left(E^{jet}_{EM}\right)|_{\eta^{meas}}}. \tag{3.6}$$

The value of this calibration function varies from ∼1.2 for high energy jets in the forward region to ∼2.1 for low energy jets in the central region, as shown in Figure 3.3. Finally, an η correction is applied to account for a bias in the measurement of jet position in the vicinity of poorly instrumented regions of the detector. The average difference $\Delta\eta = \eta^{truth} - \eta^{meas}$ is calculated in MC, binned in E^{truth} and η^{meas}. The observed $\langle \Delta\eta \rangle$ is parametrized in terms of E^{jet}_{EM+JES} and η^{meas} and amounts to a very small correction over most of the detector.

3.4 Electron Reconstruction

ATLAS uses three different algorithms for the reconstruction of electrons [88]. The standard algorithm is designed to reconstruct high p_T, isolated electrons. It is seeded by a cluster in the EM calorimeter, matched to a track from the ID. An alternative algorithm is used to reconstruct low p_T or non-isolated electrons. It is seeded by a track from the ID, matched to a cluster in the EM calorimeter. Finally, a separate algorithm is dedicated to the reconstruction of electrons in the range $2.5 \leq |\eta| \leq 4.9$. In this region no tracking information is available, so reconstruction is based on calorimeter information only.

The standard "egamma" algorithm [88, 89] is primarily responsible for reconstructing high p_T, isolated electrons, with $|\eta| \leq 2.47$. It begins by searching

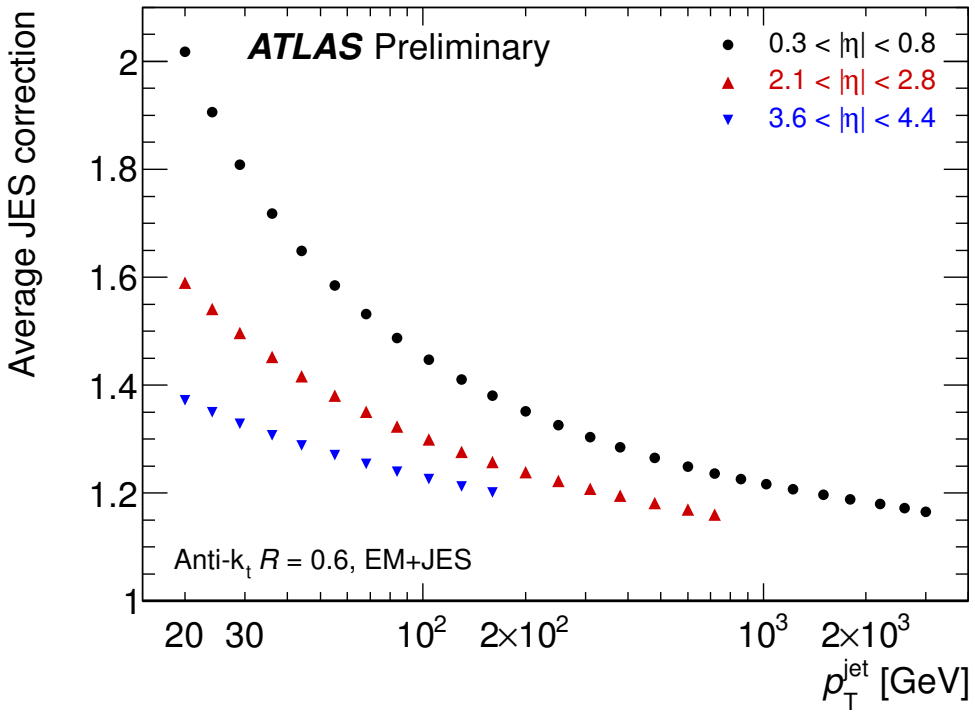

Figure 3.3: Average JES correction as a function of jet p_T for anti-k_t jets with radius parameter $R = 0.6$. Similar results are found for anti-k_t jets with radius parameter $R = 0.4$. Three η intervals are shown [87].

for clusters in the EM calorimeter using a sliding window algorithm [82]. The EM calorimeter is divided into a grid of $\Delta\eta \times \Delta\phi = 0.025 \times 0.025$ elements. The longitudinal cells within an element are summed to produce energy "towers." Cells which fall in multiple towers have their energy shared. A 3×5 window in units of $\Delta\eta \times \Delta\phi$ is translated from node to node. At each node, the transverse energy contained within the window is summed. If this energy exceeds 2.5 GeV, a pre-cluster is formed. The position of the pre-cluster is computed using a smaller 3×3 window around the pre-cluster center. The position is defined as the energy-weighted barycenter of all contained towers. If multiple pre-clusters fall within 2×2 of each other, only the pre-cluster with the largest traverse energy is kept. Clusters are formed centered on each remaining pre-cluster, which consist of all cells contained within a 3×7 (5×5) rectangular window, in the barrel (end-cap) region. The difference in window size is due to different shower distributions in the two regions. In the barrel region the rectangle is wider in the bending direction to account for bremstrahlung radiation. A track from the ID must be matched to this cluster to be considered an electron candidate. Tracks from the ID are extrapolated to the second layer of the calorimeter. If the track is associated to Pixel and/or SCT hits, then the track is required to match the cluster position within $\Delta\eta \leq 0.05$, and $\Delta\phi \leq 0.1$ in the direction toward which it bends and $\Delta\phi \leq 0.05$ in the opposite direction. If the track consists of TRT hits only, the track and cluster are required to match in ϕ only.

A second "softe" algorithm [88, 89], responsible for reconstructing low p_T and non-isolated electrons with $|\eta| \leq 2.47$, is seeded by ID tracks. Track preselection is performed, requiring a minimum p_T and hit multiplicity in each of the three ID systems. Tracks passing these criteria are then extrapolated to the calorimeter and a cluster is formed around the track. Overlap removal is performed on these electron candidates; if multiple electron candidates fall within $\Delta\eta < 0.05$ and $\Delta\phi < 0.1$, only the candidate with larger p_T is kept. It is possible for an electron to be reconstructed by both the egamma and softe algorithms. Electron candidates which share a common track are considered duplicates. In this case, the electron candidate resulting from the softe algorithm is discarded.

In the forward region, $2.5 \leq |\eta| \leq 4.9$, no tracking information is available. A third algorithm [89] is used in this region to reconstruct electrons and photons using calorimeter information only. This algorithm is seeded by topological clusters, discussed in Section 3.3, and requires small hadronic energy content in the cluster.

For electrons reconstructed in the central region $|\eta| < 2.47$, the four momentum is determined from both calorimeter and track information. The

energy is taken from the cluster. If the track contains at least four Si tracking hits, the direction is taken from the track, otherwise it is also taken from the cluster.

A set of cut based identification requirements [90] are imposed on electron candidates to reject background electrons from photon conversions and Dalitz decays ($\pi^0 \to e^+e^-\gamma$), and jets faking electrons. For central electrons, three sets of baseline identification cuts are collectively referred to as loose, medium, and tight. Hadronic jets sometimes contain real electrons from semi-leptonic decays, and can also occasionally mimic EM shower shapes. The baseline identification cuts offer jet rejection of ∼500, ∼5000, and ∼50000 respectively. The medium (tight) criteria yields an efficiency of 92%-97% (75%-86%) for electrons with E_T = 20-50 GeV, as measured in $Z \to ee$ events in data. The loose criteria impose restrictions on the lateral width of the EM shower, the ratio of the energy in a 3×7 window to the energy in a 7×7 window (both centered on the electron position), and the leakage of the shower into the hadronic calorimeter. The medium criteria add a requirement on the total EM shower width, and require at least one hit in the Pixel Detector, at least seven hits in the Pixel Detector and SCT combined, transverse impact parameter $|d_0|$ less than 5 mm, and difference in η between the cluster position and the extrapolated track $|\Delta\eta|$ less than 0.01. The tight criteria impose stricter track quality and track-cluster matching restrictions, as well as particle identification information from the TRT. The d_0 and $\Delta\eta$ cuts are reduced to 1 mm and 0.005 respectively. The difference in ϕ between the cluster position and the extrapolated track $|\Delta\phi|$ is required to be less than 0.02 and at least one hit is required in the Pixel Detector b-layer. Additional requirements on the ratio of the cluster energy to the track momentum, the total number of TRT hits, and the ratio of the number of high-threshold TRT hits to the total number of TRT hits are imposed. Requirements for which explicit cut values were not specified above are optimized in 10 $|\eta|$ bins and 11 E_T bins ranging from 5-80 GeV.

Forward electrons have only two sets of identification requirements, loose and tight. These criteria are based on shower shapes and moments, defined by $\langle x^n \rangle = \sum_i E_i x_i^n / \sum_i E_i$, where i runs over all cells in a cluster and x_i could be the distance of cell i to the shower center in the transverse or longitudinal directions. No discrimination is available between electrons and photons in this region.

Electron energy scale (EES) calibration was performed using the 2010 dataset and the well known Z mass [90]. For calibration, events are selected with two electrons, where the electrons have $E_T > 20$ GeV and $|\eta| < 2.47$. The dielectron invariant mass is required to fall in a window around the Z

mass, 80 GeV $< m_{ee} <$ 100 GeV. Calibration constants α_i are defined by $E^{meas} = E^{true}(1+\alpha_i)$, where E^{meas} (E^{true}) is the measured (true) electron energy. Each of the 58 α_i corresponds to a region of η, and are determined by minimizing the negative log-likelihood

$$-\ln L_{tot} = \sum_{k=1}^{N_{events}} -\ln L_{ij}\left(\frac{m_k}{1+\frac{\alpha_i+\alpha_j}{2}}\right), \tag{3.7}$$

where k labels the event, i and j correspond to the two η regions containing the electrons, m_k is the measured dielectron mass, and $L_{ij}(m)$ is the probability distribution function which specifies the compatibility of mass m_k with the known Z lineshape. By this procedure, the α_i are found to be within $\pm 2\%$ ($\pm 5\%$) in the barrel (end-cap) region. A similar procedure was applied using the known J/ψ mass, and the results found to be consistent to within $\sim$1%.

3.5 Muon Reconstruction

Muon reconstruction begins by attempting to find tracks in the MS. An outside-in approach is taken, starting with the outermost chambers [91]. First, nearly-straight track segments are found based on hits within the outermost chambers that roughly point back to the IP. If enough hits within a chamber are associated to a track segment, and the segment is sufficiently straight, the segment is extrapolated back to the next chamber. A loose estimate of the momentum can be determined from the track segment, and several momentum hypotheses around this estimate are tried. If a track segment is found in this chamber which matches any of the extrapolated track candidates, it is added to the track candidate and it is refit. Using the improved momentum estimate, this track candidate is extrapolated to the next chamber and the process is repeated. All track candidates which now contain at least two track segments are refit, and track candidates with a large χ^2 are discarded. The remaining track candidates are then extrapolated to the IP, accounting for energy loss in the various detector components.

ATLAS defines several types of muon candidates [92]. Standalone muon candidates consist solely of tracks in the MS. Segment tagged muons consist of track segments from the MS combined with ID tracks. However, only combined muon candidates are used in this analysis. Combined muon candidates are composed of full MS tracks matched with ID tracks. The combination of the two tracks is done through a statistical average, making use of the covariance matrices for each of the two individual track fits. If P_{ID} (P_{MS}) is the vector of track fit parameters and C_{ID} (C_{MS}) is the covariance matrix from the ID

(MS) fit alone, then the combined covariance matrix C and track match χ^2 is given by

$$C = \left(C_{ID}^{-1} + C_{MS}^{-1}\right)^{-1} \tag{3.8}$$

and

$$\chi^2_{match} = \left(P_{ID} - P_{MS}\right)^T \left(C_{ID} + C_{MS}\right)^{-1} \left(P_{ID} - P_{MS}\right). \tag{3.9}$$

This combination is performed for all ID and MS track pairs in an event which match crudely in η-ϕ space. The pair with the lowest χ^2_{match} is removed from the list of tracks. If $\chi^2_{match} < 25$, the pair is deemed a muon candidate. The pairing of ID and MS tracks is then repeated with all remaining tracks and the process is repeated until no suitable pairs remain.

3.6 Missing Transverse Energy Reconstruction

Neutrinos produced within the detector escape undetected. Many additional weakly interacting particles have been proposed, for which this would also be the case. Production of such particles can be inferred through the exploitation of transverse momentum conservation. The initial pp collision has zero momentum transverse to the beam axis. If the final state particles exhibit a momentum imbalance transverse to the beam, this is a sign that some particle(s) escaped undetected. However, mis-measurement, inactive detector regions, and non-hermetic coverage of the IP in η can also lead to an artificial momentum imbalance. Due to the composite nature of protons, the partonic initial state generally does contain net longitudinal momentum, which is unknown. Therefore, only the transverse momentum imbalance is a useful quantity, and not the longitudinal imbalance as well.

The negative vector sum of the momentum of all final state physics objects is defined as the missing transverse energy $\not{E}_T$. Calorimeter cells associated to reconstructed objects are calibrated according to the object type to which they are associated. If a cell is associated to more than one reconstructed object type, the calibration order of precedence is: electron, photon, τ, jet, muon. These cells are then included in the sum only once; there is no double counting of cells. Calorimeter cells within topoclusters not associated to any reconstructed physics object are included as well. If no track is matched to the topocluster, the cluster E_T is used in the sum, otherwise the track p_T is used. The p_T of tracks not matched to topoclusters are included in the sum as well. Finally, the p_T of muons is included in the sum. For $|\eta| < 2.5$, only combined muons are used, whereas for $2.5 < |\eta| < 2.7$ the standalone MS p_T is used.

Chapter 4

Event Generation

Generally speaking, the search for new physics is a search for small deviations from the SM. Therefore, extremely accurate signal and SM model background predictions are required. These predictions take the form of samples of events representing various physics scenarios, as they would be seen by the ATLAS detector. Monte Carlo (MC) event generators are used to simulate pp interactions resulting in a variety of final states. The passage of these final state particles through the ATLAS detector is then simulated, and the resulting detector level data is determined. The nominal reconstruction algorithms are then run on this simulated detector data, allowing direct comparison with real data.

4.1 Event Generators

The simulation of an event begins with event generation [93–95]. Event generators are software packages which take as input a desired initial state. They simulate all possible outcomes, or a selected subset of outcomes, from an interaction between the specified initial state particles. Bare partons produced in the hard scattering undergo gluon radiation or splitting, and subsequently undergo hadronization to form colorless hadrons. Unstable particles produced in the hard interaction or parton shower are made to decay to stable particles according to their known, or imposed, branching fractions and lifetimes.

Partons which take part in hard scattering interactions with large momentum transfer can be considered free due to asymptotic freedom, discussed in Section 1.1.4. The large energy scale involved allows treatment of the interaction using perturbative methods. Therefore, the pp cross section at the LHC

for a given N particle final state is given by

$$\sigma_N = \sum_{a,b} \int_0^1 \mathrm{d}x_1 \int_0^1 \mathrm{d}x_2 \, f_a\left(x_1, \mu^2\right) f_b\left(x_2, \mu^2\right) \hat{\sigma}_N^{ab}, \tag{4.1}$$

where the sum is over all parton species a and b within protons 1 and 2, $f_i\left(x_j, \mu^2\right)$ is the probability (calculated at renormalization scale μ^2) of finding parton species i carrying a momentum fraction x_j of the parent proton j, and $\hat{\sigma}_N^{ab}$ is the partonic cross section for initial state $a+b$. The function $f_i\left(x_j, \mu^2\right)$ is referred to as a parton distribution function (PDF). The main task involved in simulation of the hard interaction is the evaluation of this integral. The partonic cross section is itself given by

$$\hat{\sigma}_N^{ab} = \int \mathrm{d}\hat{\sigma}_N^{ab} = \frac{(2\pi)^4 S}{4\sqrt{(p_1 \cdot p_2)^2 - m_1^2 m_2^2}} \times \int \left[\prod_{i=1}^{N} \frac{\mathrm{d}^3 \mathbf{q}_i}{(2\pi)^3 2E_i}\right] \delta^4\left(p_1 + p_2 - \sum_{i=1}^{N} q_i\right) \left|\mathscr{M}_{p_1 p_2 \to \{q_i\}}^{ab}\right|^2, \tag{4.2}$$

where p_i are the incoming particle four-momenta, q_i (E_i) are the outgoing particle four-momenta (energies), S is a product of factors $1/j!$ for each set of j identical particles in the final state, and $\mathscr{M}_{p_1 p_2 \to \{q_i\}}^{ab}$ is the parton level matrix element (ME) for the process [96]. The event generator must build and evaluate all Feynman diagrams associated with the given process to determine the parton level ME, or these must be hardcoded by the package authors. For large multiplicity final states this can include a huge number of diagrams, and its simulation becomes a very complicated problem even at tree level. NLO event generators have recently been developed [97] which include loop diagrams. The inclusion of loops complicates the matter enormously as divergences arise in real and virtual contributions which must cancel. Once the MEs have been evaluated, the evaluation of the multidimensional phase space integration required for the random sampling is performed using MC techniques [98]. The spectator partons which did not take part in the initial hard interaction can undergo semi-hard interactions with each other, which is referred to as the underlying event (UE). Because these spectator interactions are typically soft, they are not calculable by perturbative methods and empirical models are invoked to describe them.

Bare partons may be produced as a result of the hard interaction. These partons are perturbatively evolved from the scale of the hard interaction through succesive branchings down to a lower O(GeV) energy scale at which

they combine to form colorless hadrons, the hadronization scale. These successive branchings are the origin of hadronic jets, whereby individual partons lead to a cascade of partons moving in the general direction of the original parton and sharing its momentum. The probability for a parton to branch into two partons as it evolves from scale t to $t' < t$ and the kinematics of such a branching can be calculated from first principles, accurate to fixed order in the strong coupling; the results of which are known as the DGLAP evolution equations [99–101]. Thus, the partons are recursively evolved down to the hadronization scale through successive branchings. Care must be taken to avoid double counting of regions of phase space. After showering of an $N-1$ particle final state, an additional hard parton can be radiated, thus producing overlap with an N particle hard interaction final state. The colored proton remnants which did not take part in the hard interaction can produce showers as well.

At the hadronization scale, the showering ceases and the colored partons group to form colorless hadrons. This regime is not amenable to perturbative calculations, and no first-principle theory is available. Various phenomenological methods have been developed to model hadronization, including the Lund string model [102, 103] and the cluster hadronization model [104, 105]. In the Lund model, color strings attach to a pair of quarks, and as these strings stretch energy is built up in the chromomagneitc field until vacuum excitation of a quark-antiquark pair becomes possible. Ultimately, color connected pairs of quarks form hadrons. The cluster hadronization model assumes a local parton-hadron duality, thus hadronic quantum numbers result from the quantum numbers of local partons with minimal disruption needed to produce colorless hadrons. Regardless of the hadronization model choice, the produced hadrons are often unstable, and are then decayed to stable hadrons.

4.1.1 HERWIG

HERWIG [106] is a general purpose, tree level, partonic ME generator which also performs parton showering, hadronization, and UE simulation. It is capable of simulating many SM and SUSY processes. Decays of unstable resonances are treated including full spin correlations. Parton showering is performed for both initial and final state particles using a coherent branching algorithm, with leading log (LL) accuracy. The parton branchings are ordered in angle, meaning that emission angles get successively smaller as the shower evolves. Exact LO MEs are used to populate regions of phase space with larger angle emmision. Hadronization is performed using a cluster model. A minimum bias event generator is used to simulate the soft interaction between proton remnants, and an external package JIMMY [107, 108] simulates multi-

ple parton interactions. HERWIG is used in this analysis to produce diboson (WW, WZ, ZZ) MC samples, as well to perform showering and hadronization for W and Z boson and top quark samples, and is used to assess systematic uncertainties in the case of the top quark background.

4.1.2 PYTHIA

PYTHIA [109] is a general purpose, tree level partonic ME generator capable of performing parton showering, hadronization, and UE simulation. A variety of $2 \to 1, 2, 3$ processes are included. Full spin correlations are included in the decays of unstable resonances. Unlike HERWIG, PYTHIA shower evolutions proceeds in terms of decreasing timelike virtuality, and imposes angular ordering by veto. Shower evolution is accurate to the LL level. The Lund string model [102, 103] is used for hadronization. UE interactions are described perturbatively as multiple nearly-independent $2 \to 2$ scatterings. PYTHIA is used in this analysis to simulate signal samples, and for parton showering and hadronization of the top samples used for the assessment of systematic uncertainty arising from the choice of event generator.

4.1.3 SHERPA

SHERPA [110] is a tree level partonic ME generator which can also perform parton showering, hadronization, and UE simulation. A range of SM, SUSY, and other BSM processes can be generated. Parton showering is virtuality ordered with an angular ordering veto. Shower evolutions is accurate to the LL level. The Lund string model is used for the simulation of hadronization. SHERPA is used in this analysis to produce the W boson samples for the assessment of systematic uncertainty arising from the choice of event generator.

4.1.4 ALPGEN

ALPGEN [111] is a tree level partonic ME generator. It is designed for the calculation of exact LO partonic MEs for processes involving Higgs and gauge bosons or heavy quark pairs, in association with multiple additional partons. Mass effects of the t, b, and c quarks are included. Spin correlations in t and gauge boson decays are considered as well. ALPGEN does not perform parton showering or hadronization, but can be interfaced to a number of shower evolution and hadronization packages to perform these tasks. ALPGEN interfaced to HERWIG for showering and hadronization is used in this analysis to produce W and Z MC samples.

4.1.5 AcerMC

AcerMC [112] is a tree level partonic ME generator. It is only capable of generating 25 different SM processes, mostly containing gauge bosons or heavy quark pairs. AcerMC is relatively fast compared to other event generators. It can be interfaced to both HERWIG and PYTHIA for parton showering and hadronization. AcerMC interfaced to PYTHIA is used in this analysis to produce top samples for the assessment of systematic uncertainty arising from the choice of event generator.

4.1.6 MC@NLO

MC@NLO [113] is a NLO partonic ME generator. This allows improved cross section evaluation and enhanced modeling of hard parton emission. Many processes are included, among them are the production of Higgs, gauge bosons, and heavy quark pairs. Mass and spin correlation effects are included in particle decays. MC@NLO uses the subtraction method [113] to avoid double counting of NLO contributions. The subtraction method employs no approximation and introduces no unphysical parameters, unlike earlier NLO implementations. An interface is provided to HERWIG for parton showering and hadronization. MC@NLO interfaced to HERWIG is used in this analysis to simulate $t\bar{t}$ samples.

4.1.7 POWHEG

POWHEG [114] is a NLO partonic ME generator. It is based on a modification of typical LL shower simulation with improved simulation of the hardest branching to achieve NLO accuracy; POWHEG forces this hard emission to occur during the first branching step. Unlike MC@NLO, POWHEG can be interfaced to a variety of showering and hadronization packages, and does not produce any events with negative weight. POWHEG interfaced to HERWIG and PYTHIA is used in this analysis to produce $t\bar{t}$ samples for the assessment of systematic uncertainty arising from the choice of event generator.

4.2 Detector Simulation

The results from the event generation step, a collection of particles, their types, and four-vectors, are taken through the ATLAS detector simulation package [115], simulating the passage of the particles through the detector. This simulation package has access to the full ATLAS detector geometry and materials database, including changes that occurred over time, such as dead

regions of the detector, and simulates the interactions of the generated particles with the detector based on the known or expected particle properties. The detector description, as well as the interactions between the particles and detector material, are simulated using the object-oriented toolkit GEANT4 [116]. GEANT4 simulates a variety of EM and hadronic processes which particles may undergo while in matter, covering energies from ∼250 eV to over a PeV. The modeling of these processes is taken directly from data if available. Otherwise, theoretical models or parameterizations and extrapolations from measured data are used. A detailed geometrical description of the detector is implemented in the form of a hierarchical tree structure of volumes. Particles produced at the IP are gradually stepped through the detector, with a step size dependent on the material and the possible types of interactions and associated energy losses. Numerical calculation is performed to determine the particle trajectory through the detector, simulating energy loss and interactions along the way. Radiation and interaction length, Bethe-Bloch coefficients, etc. are all calculated locally from material properties. Continuous processes such as ionization are performed along the length of each step. After each step, random numbers determine if any of the allowed discrete processes, such as pair production, should be performed. Special sensitive regions are defined where interactions with active detector elements are recorded as "hits." These hits are later converted to "digits," the detector output which would be expected from these interactions. The simulation process takes O(10 min) per event. The produced digits are equivalent to the raw detector level data which is read out for real data events selected by the trigger system for storage. Thus, the nominal reconstruction framework can be applied to reconstruct these simulated events.

Chapter 5

Leptoquark Analysis

Data collected with the ATLAS detector at the LHC is analyzed for the presence of pair production of scalar leptoquarks decaying to the $e\not{E}_T jj$ final state. Signal and background Monte Carlo samples are used to determine appropriate object and event selection criteria. Backgrounds are modeled using a combination of Monte Carlo and data-driven techniques. A multivariate discriminant is defined which distinguishes between signal-like and background-like events. The distribution of this discriminant observed in data is compared to that expected from SM backgrounds.

5.1 Data and Monte Carlo

The collected data is compared to signal and background expectations to test for the presence of LQ production. Quality criteria are applied to ensure the data is of sufficient quality for analysis. MC is used to derive the signal expectation, while a combination of MC and data-driven techniques are used to model the SM backgrounds.

5.1.1 Data

The data used in this analysis was collected during run periods B and D-H of 2011 LHC operation. During this time, a total integrated luminosity of $\int L dt = 1.270 \pm 0.047$ fb^{-1} was delivered to the ATLAS detector. Of this, 1.035 ± 0.038 fb^{-1} was delivered while all detector subsystems were functioning sufficiently well, so that the data is suitable for this analysis. A good runs list (GRL) is used to reject data for analysis which was recorded while detector subsystems were non-operational or behaving abnormally. Data is rejected if any of the following criteria are not met:

- Data has been evaluated and approved by the ATLAS Data Quality working group.
- Magnet systems functioning and stable.
- Central trigger system working at expected efficiency. Also, no timing, consistency, or synchronization problems.
- Luminosity monitoring system on-line and functioning properly.
- Tracking systems on-line and functioning properly.
- Calorimeter systems on-line and functioning properly.
- Muon systems on-line and functioning properly.

5.1.2 Monte Carlo

All electroweak backgrounds are simulated using MC. Many software packages are available to simulate event generation, parton showering, hadronization, etc. Each package has specific strengths and weaknesses, modeling some processes better than others. For each background process, a combination of software packages is chosen which is perceived to yield the most accurate predictions. For all backgrounds, the assumed vector boson branching ratios to a single lepton flavor are BR($W \to \ell\nu$)=0.1088 and BR($Z \to \ell\ell$)=0.0336 [117].

Vector boson production in association with jets, referred to as "V+jets," is a major background. The V+jets MC samples were produced using the ALPGEN event generator with LO CTEQ6L1 PDF, interfaced to HERWIG for parton showering and hadronization, and normalized to their NNLO cross section [117]. Separate samples were generated for a W/Z produced in association with 0, 1, 2, 3, 4, and 5+ partons in the hard interaction. The $t\bar{t}$ (single top) background was produced using the MC@NLO event generator with NLO CTEQ6.6 PDF, interfaced to HERWIG for parton showering and hadronization, and normalized to its NNLO (NLO) cross section. Separate single top samples were generated for s-channel production, t-channel production, and production in association with a W boson. Diboson (WW, WZ, ZZ) samples were produced using the HERWIG event generator with a modified LO MRST2007 PDF, and normalized to their NLO cross section. The modified LO PDF uses the NLO coupling and a relaxed momentum sum rule [118]. Signal samples were produced using the PYTHIA event generator with the LO CTEQ6L1 PDF, with cross sections scaled to their NLO values. A summary of the MC samples and cross sections used can be found in Tables 5.1 and 5.2.

Process	Cross Section × BR [pb]	Generator Filter Efficiency	Equivalent Lumi [pb^{-1}]
$W \to e\nu + 0p$	8288.1	1	416.87
$W \to e\nu + 1p$	1550.1	1	413.75
$W \to e\nu + 2p$	452.09	1	8335.2
$W \to e\nu + 3p$	120.96	1	8346.9
$W \to e\nu + 4p$	30.331	1	8238.1
$W \to e\nu + 5p$	8.2722	1	8456.4
$W \to \tau\nu + 0p$	8288.1	1	412.21
$W \to \tau\nu + 1p$	1550.1	1	414.04
$W \to \tau\nu + 2p$	452.09	1	8336.3
$W \to \tau\nu + 3p$	120.96	1	8346.1
$W \to \tau\nu + 4p$	30.331	1	8237.5
$W \to \tau\nu + 5p$	8.2722	1	7699.5
$Z \to ee + 0p$	830.12	1	7965.4
$Z \to ee + 1p$	166.24	1	8023.0
$Z \to ee + 2p$	50.282	1	8052.0
$Z \to ee + 3p$	13.922	1	7897.0
$Z \to ee + 4p$	3.6156	1	8295.2
$Z \to ee + 5p$	0.94179	1	9547.8
$Z \to \tau\tau + 0p$	830.12	1	7973.3
$Z \to \tau\tau + 1p$	166.24	1	8028.5
$Z \to \tau\tau + 2p$	50.282	1	8051.6
$Z \to \tau\tau + 3p$	13.922	1	7897.1
$Z \to \tau\tau + 4p$	3.6156	1	8292.4
$Z \to \tau\tau + 5p$	0.94179	1	10611.
WW	44.9	0.39720	14010.
WZ	18.0	0.3085	45010.
ZZ	5.96	0.2123	197510
$t\bar{t}$	164.6	0.54258	90870
single top (t-channel)	$63.0 \times 1/9$	1	42842.
single top (s-channel)	$4.212 \times 1/9$	1	640660
single top (Wt)	13.00	1	69180.

Table 5.1: The MC samples used to model the SM backgrounds [119].

Process	Cross Section × BR [pb]	Equivalent Lumi [pb^{-1}]
$LQ\overline{LQ} \to eeqq$ ($m_{LQ} = 300$ GeV)	1.21	1.65×10^4
$LQ\overline{LQ} \to eeqq$ ($m_{LQ} = 350$ GeV)	0.477	4.19×10^4
$LQ\overline{LQ} \to eeqq$ ($m_{LQ} = 400$ GeV)	0.206	9.69×10^4
$LQ\overline{LQ} \to eeqq$ ($m_{LQ} = 450$ GeV)	0.0949	2.10×10^5
$LQ\overline{LQ} \to eeqq$ ($m_{LQ} = 500$ GeV)	0.0462	4.32×10^5
$LQ\overline{LQ} \to eeqq$ ($m_{LQ} = 550$ GeV)	0.0235	8.49×10^5
$LQ\overline{LQ} \to eeqq$ ($m_{LQ} = 600$ GeV)	0.0124	1.61×10^6
$LQ\overline{LQ} \to eeqq$ ($m_{LQ} = 650$ GeV)	0.00676	2.95×10^6
$LQ\overline{LQ} \to eeqq$ ($m_{LQ} = 700$ GeV)	0.00377	5.29×10^6
$LQ\overline{LQ} \to eeqq$ ($m_{LQ} = 750$ GeV)	0.00214	9.32×10^6
$LQ\overline{LQ} \to eeqq$ ($m_{LQ} = 800$ GeV)	0.00124	1.61×10^7
$LQ\overline{LQ} \to eeqq$ ($m_{LQ} = 850$ GeV)	0.000732	2.72×10^6
$LQ\overline{LQ} \to eeqq$ ($m_{LQ} = 900$ GeV)	0.000436	4.57×10^6
$LQ\overline{LQ} \to eeqq$ ($m_{LQ} = 950$ GeV)	0.000263	7.58×10^6
$LQ\overline{LQ} \to eeqq$ ($m_{LQ} = 1000$ GeV)	0.000160	1.25×10^7
$LQ\overline{LQ} \to e\nu qq$ ($m_{LQ} = 300$ GeV)	$1.21 \times 1/2$	3.30×10^4
$LQ\overline{LQ} \to e\nu qq$ ($m_{LQ} = 350$ GeV)	$0.477 \times 1/2$	8.38×10^4
$LQ\overline{LQ} \to e\nu qq$ ($m_{LQ} = 400$ GeV)	$0.206 \times 1/2$	1.94×10^5
$LQ\overline{LQ} \to e\nu qq$ ($m_{LQ} = 450$ GeV)	$0.0949 \times 1/2$	4.21×10^5
$LQ\overline{LQ} \to e\nu qq$ ($m_{LQ} = 500$ GeV)	$0.0462 \times 1/2$	8.64×10^5
$LQ\overline{LQ} \to e\nu qq$ ($m_{LQ} = 550$ GeV)	$0.0235 \times 1/2$	1.70×10^6
$LQ\overline{LQ} \to e\nu qq$ ($m_{LQ} = 600$ GeV)	$0.0124 \times 1/2$	3.22×10^6
$LQ\overline{LQ} \to e\nu qq$ ($m_{LQ} = 650$ GeV)	$0.00676 \times 1/2$	5.61×10^6
$LQ\overline{LQ} \to e\nu qq$ ($m_{LQ} = 700$ GeV)	$0.00377 \times 1/2$	1.06×10^7
$LQ\overline{LQ} \to e\nu qq$ ($m_{LQ} = 750$ GeV)	$0.00214 \times 1/2$	1.87×10^7
$LQ\overline{LQ} \to e\nu qq$ ($m_{LQ} = 800$ GeV)	$0.00124 \times 1/2$	3.22×10^7
$LQ\overline{LQ} \to e\nu qq$ ($m_{LQ} = 850$ GeV)	$0.000732 \times 1/2$	5.45×10^6
$LQ\overline{LQ} \to e\nu qq$ ($m_{LQ} = 900$ GeV)	$0.000436 \times 1/2$	9.15×10^6
$LQ\overline{LQ} \to e\nu qq$ ($m_{LQ} = 950$ GeV)	$0.000263 \times 1/2$	1.52×10^7
$LQ\overline{LQ} \to e\nu qq$ ($m_{LQ} = 1000$ GeV)	$0.000160 \times 1/2$	2.49×10^7

Table 5.2: The MC samples used to model the leptoquark signal [119].

5.2 Object Selection

The reconstruction algorithms described in Chapter 3 are designed to be flexible so that their results may be used for a variety of physics analyses. Therefore, they do not impose strict quality criteria. This leads to the reconstruction of many fake physics objects. This section describes the object selection criteria which are imposed on reconstructed electrons, muons, jets, and $\not{E}_T$. Only those object which pass these selection criteria are used throughout the analysis.

5.2.1 Electron

Electron candidates are reconstructed using the standard ATLAS cluster-based algorithm and are required to fulfill the tight identification requirements, described in Section 3.4. In addition, electron candidates must have $E_T \equiv E_{cluster}/\cosh(\eta_{track}) \geq 30$ GeV. Electron candidates must also satisfy $|\eta| \leq 2.47$. In order to remove electrons which fall in the region between the barrel and endcap calorimeters, whose energy may be poorly measured, electron candidates in the range $1.37 \leq |\eta| \leq 1.52$ are excluded. An energy isolation requirement is imposed on electron candidates in order to reduce the amount of non-prompt and fake electrons. Non-prompt electrons result from weak decays of long-lived particles and fake electrons are jets mis-identified as electrons. The isolation requirement is $E_T^{cone20}/E_T \leq 0.1$, where E_T^{cone20} is the amount of transverse energy falling in a cone of $\Delta R < 0.2$ around the electron, excluding the energy attributed to the electron itself. E_T^{cone20} is affected by two important factors, lateral leakage of the electron shower and calorimeter deposits from both in- and out-of-time pileup. Both of these effects have been studied in 2011 data [120], and the corrections derived are applied here.

5.2.2 Muon

Muon candidates are formed from the merged output of the STACO, Muonboy, and MuTag reconstruction algorithms, described in Section 3.5. In addition, muon candidates must fulfill the tight identification requirements and must be a combined muon. Muon candidates must also satisfy $p_T \geq 20$ GeV and $|\eta| \leq 2.4$. The isolation requirement $p_T^{cone20} \leq 0.2$ is applied to reduce non-prompt muons and jets which fake muons, where p_T^{cone20} is the sum of the p_T of all tracks within a cone of $\Delta R < 0.2$ around the muon track, excluding the muon p_T. To reduce muons from cosmic rays, cuts are applied to the muon candidate transverse and longitudinal impact parameters, $|d_0| < 0.1$ mm

and $|z_0| < 5$ mm. Finally, a number of quality cuts are imposed on the muon candidate ID track:

- The ID track is associated to a hit in the Pixel b-layer
  OR the track crossed an uninstrumented or dead region of the Pixel b-layer
- The number of Pixel hits plus dead Pixel sensors crossed is ≥ 2
- The number of SCT hits plus dead SCT sensors crossed is ≥ 6
- The number of sensitive Pixel and SCT layers crossed by the track but that recorded no hit is ≤ 2
- The number of TRT outlier hits $n_{TRT}^{outliers}$ must be sufficiently small compared to the number of TRT hits associated to the track n_{TRT}^{hits}
  - If $|\eta| < 1.9$
    Require: $n_{TRT}^{hits}+n_{TRT}^{outliers} > 5$ **AND** $n_{TRT}^{outliers} < 0.9 \cdot \left(n_{TRT}^{hits} + n_{TRT}^{outliers}\right)$
  - If $|\eta| \geq 1.9$ **AND** $n_{TRT}^{hits} + n_{TRT}^{outliers} > 5$
    Require: $n_{TRT}^{outliers} < 0.9 \cdot \left(n_{TRT}^{hits} + n_{TRT}^{outliers}\right)$

5.2.3 Jet

Jet candidates are reconstructed from topological clusters, using the anti-k_t reconstruction algorithm with a cone parameter of 0.4, as described in Section 3.3. Their energy is corrected to the hadronic energy scale. Jet candidates are required to satisfy $p_T \geq 30$ GeV and $|\eta| \leq 2.8$. Any jet reconstructed within a distance of $\Delta R < 0.4$ to an electron is discarded to avoid double counting.

Jets reconstructed from real in-time energy deposits in the calorimeter, but which fall in a region of the calorimeter with poor energy measurement ("ugly" jets) are discarded. These regions correspond to the transition between the barrel and endcap calorimeters, and also regions with known hardware problems.

In data, jets reconstructed from fake or out-of-time energy deposits in the calorimeter ("bad" jets) are discarded. These jets originate from detector malfunction and beam or cosmic backgrounds. The following are the common sources of bad jets, and the additional jet quality requirements that are imposed to reduce their number:

- HEC Spikes

- Less than half of the energy is deposited in the HEC
  OR more than half of the energy deposited in the HEC is found in cells with a pulse shape consistent with expectation for real jets
- Small amount of negative energy ($|E_{neg}| \leq 60$ GeV)

- EM Coherent Noise
  - Non-negligible fraction ($\geq$5%) of the energy is deposited in the hadronic calorimeters
    OR at least 80% of the energy deposited in the EMC is found in cells with a pulse shape consistent with expectation for real jets
    OR $|\eta| \geq 2.8$

- Non-collision backgrounds
  - Small ($\leq$25 ns) energy-squared-weighted cell mean time relative to the BC
  - Non-negligible fraction ($\geq$5%) of the energy is deposited in the EMC
    OR non-negligible fraction ($\geq$5%) of jet p_T is matched to charged particle tracks
    OR $|\eta| \geq 2$
  - Non-negligible fraction ($\geq$5%) of the energy is deposited in the EMC
    OR $|\eta| < 2$
  - No more than 99% of the total jet energy is deposited in a single calorimeter layer
    OR $|\eta| \geq 2$

5.2.4 Missing Transverse Energy

$\not\!\!E_T$ is reconstructed using the RefFinal algorithm, described in Section 3.6. In events with an ugly jet, significant $\not\!\!E_T$ mis-measurement can occur. Therefore, events which contain an ugly jet with $p_T \geq 20$ GeV and $|\eta| \leq 4.5$ are rejected as the $\not\!\!E_T$ measurement is unreliable.

5.3 Monte Carlo Corrections

Minor differences between the data and MC predictions are observed. Small corrections must therefore be applied to the electron selection efficiency and

energy resolution in order to accurately model the data. The pileup conditions in the MC must also be corrected to match those observed in data.

5.3.1 Electron Selection Efficiency

The electron selection efficiency can be factorized into a number of independent efficiencies, according to

$$\epsilon = \epsilon_{reco} \times \epsilon_{ID} \times \epsilon_{trigger} \times \epsilon_{iso}, \tag{5.1}$$

where ϵ_{reco} is the efficiency to reconstruct an electron ID track and loosely match it to its associated electromagnetic cluster, ϵ_{ID} is the efficiency for reconstructed electrons to pass identification criteria, $\epsilon_{trigger}$ is the efficiency for reconstructed and identified electrons to fire the electron trigger, and ϵ_{iso} is the efficiency of reconstructed, identified, trigger electrons to pass the isolation criteria. All of these individual efficiencies must be well modeled in MC to obtain an accurate description of the data. Small corrections are applied to MC to achieve this agreement. E_T- and/or η-dependent weights are applied to each event for each efficiency, defined as the ratio of the efficiencies observed in data and MC.

The electron efficiencies are evaluated independently using a data-driven tag and probe technique [90, 121]. An unbiased sample of electron probes are found by considering events consistent with a W or Z boson decay, containing a high-quality tag object. The tag object is $\not\!\!E_T$ (an electron) in events consistent with a W (Z) boson decay, satisfying strict quality requirements. Minimal requirements are imposed on the probe object in order to avoid biasing the measurement.

After selection of events consistent with W or Z decays, some residual background events will inevitably remain. A discriminating variable is chosen which is uncorrelated with the desired efficiency. A function or template is then fit to the observed distribution of the discriminating variable in a region dominated by background and extrapolated to the region dominated by the signal. The efficiency is then calculated in the signal region after subtracting off this background contribution, by applying the cut to the probe objects. The results are summarized in Tables 5.3 and 5.4.

Selection	Data [%]	MC [%]	Ratio
Reconstruction	$98.7 \pm 0.1 \pm 0.2$	98.3	$1.005 \pm 0.001 \pm 0.002$
Identification	$80.7 \pm 0.5 \pm 1.5$	78.5	$1.028 \pm 0.006 \pm 0.016$
Trigger	99.02 ± 0.09	99.54	0.995 ± 0.001

Table 5.3: The electron reconstruction, identification, and trigger efficiencies observed in data, predicted by MC, and their ratio. The values specified were derived from electrons with $|\eta| < 2.47$ (excluding the transition region between barrel and end-cap calorimeters at $1.37 < |\eta| < 1.52$) and $20 < E_T < 50$ GeV. For the data measurements, the first (second) error corresponds to statistical (systematic) uncertainty. The statistical uncertainty is negligible for MC [90].

E_T [GeV]	Data [%]	MC [%]	Ratio
30-35	0.9762 ± 0.0008	0.9740	1.0023 ± 0.0008
35-40	0.9854 ± 0.0005	0.9837	1.0018 ± 0.0005
40-45	0.9933 ± 0.0003	0.9928	1.0006 ± 0.0003
45-50	0.9958 ± 0.0003	0.9963	0.9994 ± 0.0003
50-60	0.9969 ± 0.0004	0.9968	1.0001 ± 0.0003
60-80	0.9964 ± 0.0006	0.9977	0.9987 ± 0.0006
80-25	0.9968 ± 0.0012	0.9980	0.9989 ± 0.0011

Table 5.4: The electron isolation efficiencies observed in data, predicted by MC, and their ratio. The values specified were derived from electrons with $|\eta| < 2.47$ (excluding the transition region between barrel and end-cap calorimeters at $1.37 < |\eta| < 1.52$). For the data measurements, the errors represent combined statistical + systematic uncertainties. For MC, the statistical uncertainty is negligible [119, 122].

$\lvert\eta\rvert$	c_{data}	c_{MC}
$0 - 1.37$	$0.011 + 0.005 - 0.006$	0.007
$1.37 - 2.47$	$0.018 + 0.006 - 0.006$	

Table 5.5: The value of the EER constant term observed in data and predicted by MC. For the data measurements, the errors represent combined statistical + systematic uncertainties. The statistical uncertainty is negligible for MC [90].

5.3.2 Electron Energy Resolution

The electron energy resolution (EER) is measured in both data and MC [90]. The resolution σ_E is parameterized according to

$$\frac{\sigma_E}{E} = \frac{a}{\sqrt{E}} \oplus \frac{b}{E} \oplus c, \tag{5.2}$$

where a represents the sampling term, b represents the noise term, and c is the constant term. The noise term is only important for low energy electrons, and the sampling term is assumed to be well modeled in MC. The resolution is determined in events consistent with $Z \to ee$ decays in both data and MC. A Breit-Wigner function convolved with a Crystal Ball function [123] is fit to the m_{ee} distribution in data and MC for several η bins. The Breit-Wigner width is fixed to the known Z width, so that the Crystal Ball width gives the experimental resolution. The values of the constant term observed in data and predicted by MC are shown in Table 5.5. The resolution predicted by MC is better than that observed in data. Thus, energy smearing is applied in MC so that the energy resolution in data and MC agree; the energy is multiplied by a smearing factor sampled from a Gaussian distribution with a mean of one and a standard deviation chosen so that the MC energy resolution duplicates that observed in data.

5.3.3 Pileup Correction

The average number of pp interactions per bunch crossing $\langle\mu\rangle$ is related to the instantaneous luminosity, which varied over the course of data taking. Furthermore, the MC used in this analysis was produced before the data was taken, so the actual pileup conditions were unknown. Thus, the MC was generated assuming a broad range of $\langle\mu\rangle$ values would be experienced over time. Naturally, the anticipated $\langle\mu\rangle$ distribution does not match that observed in the data. In order to accurately model the data, the MC is reweighted so the $\langle\mu\rangle$ distribution matches the distribution observed in data.

5.4 LAr Hole

On April 30th, 2011, a hardware failure occurred in the EMC, affecting a 1.6×0.4 region in (η, ϕ), the so-called LAr hole. A problem with a controller board prevented readout from six front-end boards in this region, resulting in significant electron energy underestimation and poor jet energy resolution, which leads to degraded $\not\!\!E_T$ resolution. In order to accurately model the data, it is therefore necessary to simulate this hole in MC. Although the LAr hole was eventually repaired, approximately 84% of the data used in this analysis was recorded with the LAr hole present, so the following prescription was applied to a randomly selected 84% of all MC events:

- Electrons - Veto electrons which fall in the LAr hole region.
- Jets - Veto events with a jet in the LAr hole, if the jet $p_T > 30$ GeV. In data, a correction is applied to the jet p_T which attempts to account for the fraction of jet energy which went unmeasured.

5.5 Background Modeling

Accurate modeling of the SM backgrounds is essential. This section describes the techniques used to model the various SM backgrounds, and the control regions which are used to verify the accuracy of the modeling.

5.5.1 Background Control Regions

Three control regions are defined in order to check, and also improve, the accuracy of the background modeling and normalization. Control regions are defined on top of the nominal event selection for the dominant W+jets and $t\bar{t}$ backgrounds, with additional requirements designed to enhance background purity and reduce signal contamination. The control region definitions are summarized in Table 5.6. Two important variables used in the CR definitions, S_T and the transverse mass m_T, are defined in Equations 5.3 and 5.4 respectively.

$$S_T = E_T^e + \not\!\!E_T + p_T^{j_1} + p_T^{j_2} \tag{5.3}$$

$$m_T = \sqrt{2E_T^e \not\!\!E_T \left(1 - \cos\Delta\phi_{e,\not\!\!E_T}\right)} \tag{5.4}$$

V+2 Jets Exclusive CR

- $N_{jets} = 2$
- $m_T \leq 120$ GeV
- $S_T \leq 225$ GeV

The most significant background to this analysis is W boson production in association with two jets, where the W decays to an electron and an electron neutrino. This gives the identical $e\not{E}_T jj$ final state as the $LQ\overline{LQ}$ production and decay considered here. However, there are several kinematic distributions which differ significantly for W and signal events, as shown in Figures 5.11, 5.13, and 5.15. These are exploited to preferentially select W+jets events, and reject $t\bar{t}$ and signal events. For W+jets events, the m_T distribution broadly peaks around the W mass, whereas for signal this distribution is essentially flat over the range from zero to m_{LQ}. Also, due to the low mass of the W as compared to the top quark and LQ, the decay products generally have less transverse momentum in W events. These two facts are exploited to define the V+2 jets exclusive CR. The m_T and S_T distributions, as well as the LQ invariant and transverse masses, are shown in Figure 5.1. The LQ invariant and transverse masses are determined for both possible jet-electron and jet-$\not{E}_T$ combinations, and the pairing which minimizes the mass difference is kept. Background predictions agree well with observed data yields, as shown in Table 5.8.

V+3 Jets Inclusive CR

- $N_{jets} \geq 3$
- $m_T \leq 120$ GeV
- $S_T \leq 225$ GeV

V+2 jets	V+3 jets	$t\bar{t}$
passes event selection		
$m_T \leq 120$ GeV		
$S_T \leq 225$ GeV		$p_T(j_1, j_2) \geq 50, 40$ GeV
$N_{jets} = 2$	$N_{jets} \geq 3$	$N_{jets} \geq 4$

Table 5.6: Definitions of the the V+jets and $t\bar{t}$ control regions.

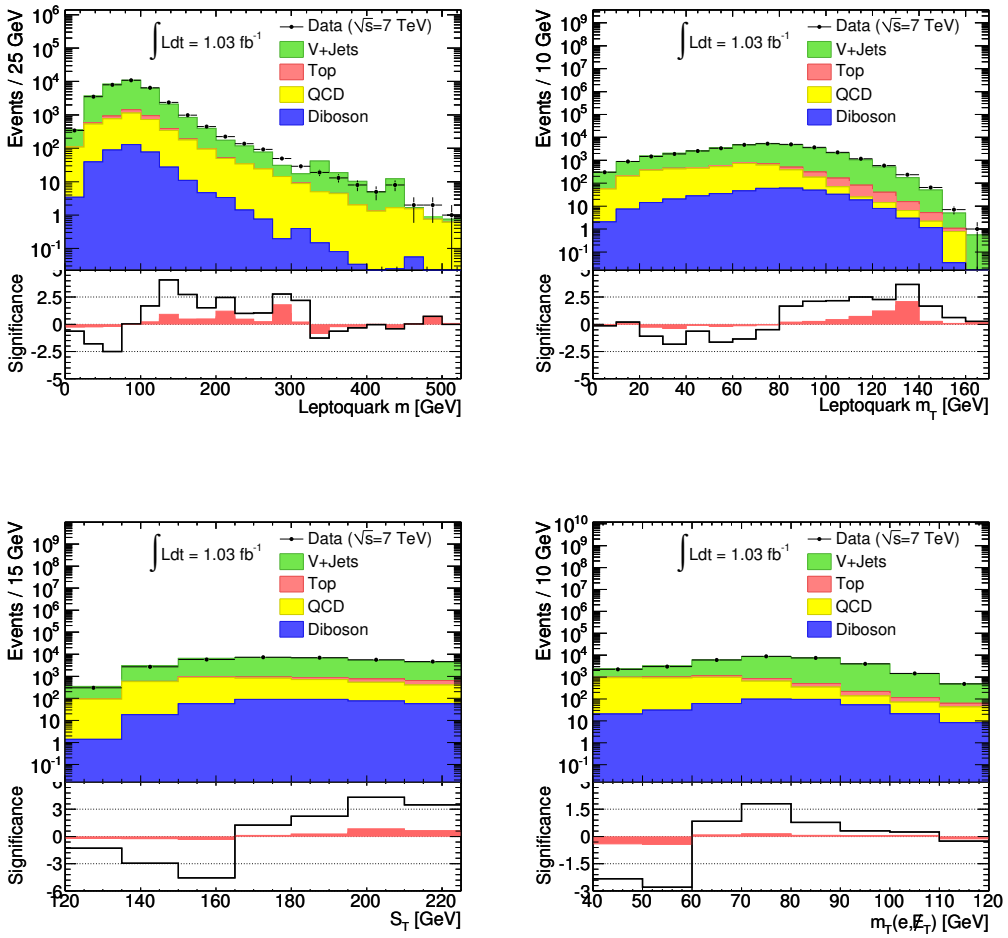

Figure 5.1: Kinematic distributions for the V+2 jets exclusive control region. LQ mass (upper left), LQ transverse mass (upper right), S_T (lower left), m_T (lower right). Backgrounds are represented by filled histograms, with colors as shown in the legend. Data corresponding to 1.03 fb^{-1} is represented by black dots. Signal is not shown as its yield is negligible. The solid line (band) in the lower plot shows the Gaussian statistical (statistical + systematic) significance of the deviation between data and predicted backgrounds.

The production of W bosons in association with three or more jets is also an important background to this analysis. Although good agreement is found in the exclusive two jet CR, a mis-modeling of the jet multiplicity, due for instance to an inadequate modeling of parton splitting or showering, could lead to poor modeling of W production in association with three or more jets. It is therefore important to check that this background is also well modeled by the MC. The same kinematic features as for V+2 jets CR are exploited here to obtain a high purity W+3 jets inclusive sample, with the only difference being the jet multiplicity requirement. The LQ invariant and transverse masses, S_T, and m_T distributions are shown in Figure 5.2. Background predictions agree well with observed data yields, as shown in Table 5.8.

$t\bar{t}$ CR

- $N_{jets} \geq 4$
- $m_T \leq 120$ GeV
- $p_T\,(j_1, j_2) \geq 50$, 40 GeV

The last of the major backgrounds is $t\bar{t}$. Semi-leptonic $t\bar{t}$ decay gives the same $e\not{E}_T jj$ final state as the signal investigated in this analysis, with extra jets. Fully hadronic $t\bar{t}$ decay can also fake this final state if one of the jets is reconstructed as an electron, as well as fully leptonic $t\bar{t}$ decay if one of the electrons falls outside the detector acceptance or fails reconstruction for some other reason. Differences between $t\bar{t}$, W+jets, and signal events, shown in Figures 5.11, 5.13, and 5.15, are exploited to obtain a CR with relatively high purity of $t\bar{t}$ events, and negligible signal contamination. $t\bar{t}$ events have high jet multiplicity, and the jets have relatively high p_T compared to those from W events. An m_T cut is again used to reject signal events. The LQ invariant and transverse masses, S_T, and m_T distributions for this CR are shown in Figure 5.3. Background predictions agree well with observed data yields, as shown in Table 5.8.

5.5.2 QCD

Jets from QCD interactions are occasionally reconstructed as electrons. In order to estimate the background contribution from QCD, fully data-driven methods are employed. The shape and an estimate of the QCD background normalization is obtained through a matrix method (MM). The shape from the MM is then used in an alternative fit method to determine a second estimate of

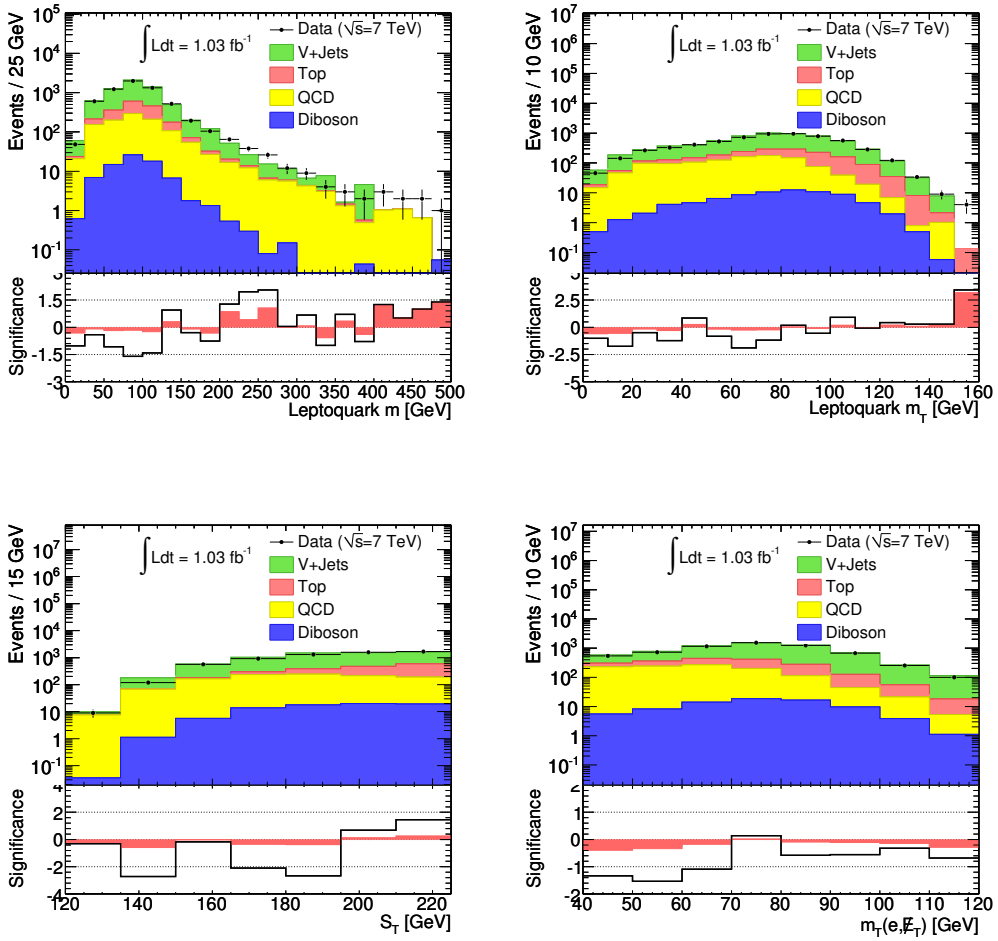

Figure 5.2: Kinematic distributions for the V+3 jets inclusive control region. LQ mass (upper left), LQ transverse mass (upper right), S_T (lower left), m_T (lower right). Backgrounds are represented by filled histograms, with colors as shown in the legend. Data corresponding to 1.03 fb^{-1} is represented by black dots. Signal is not shown as its yield is negligible. The solid line (band) in the lower plot shows the Gaussian statistical (statistical + systematic) significance of the deviation between data and predicted backgrounds.

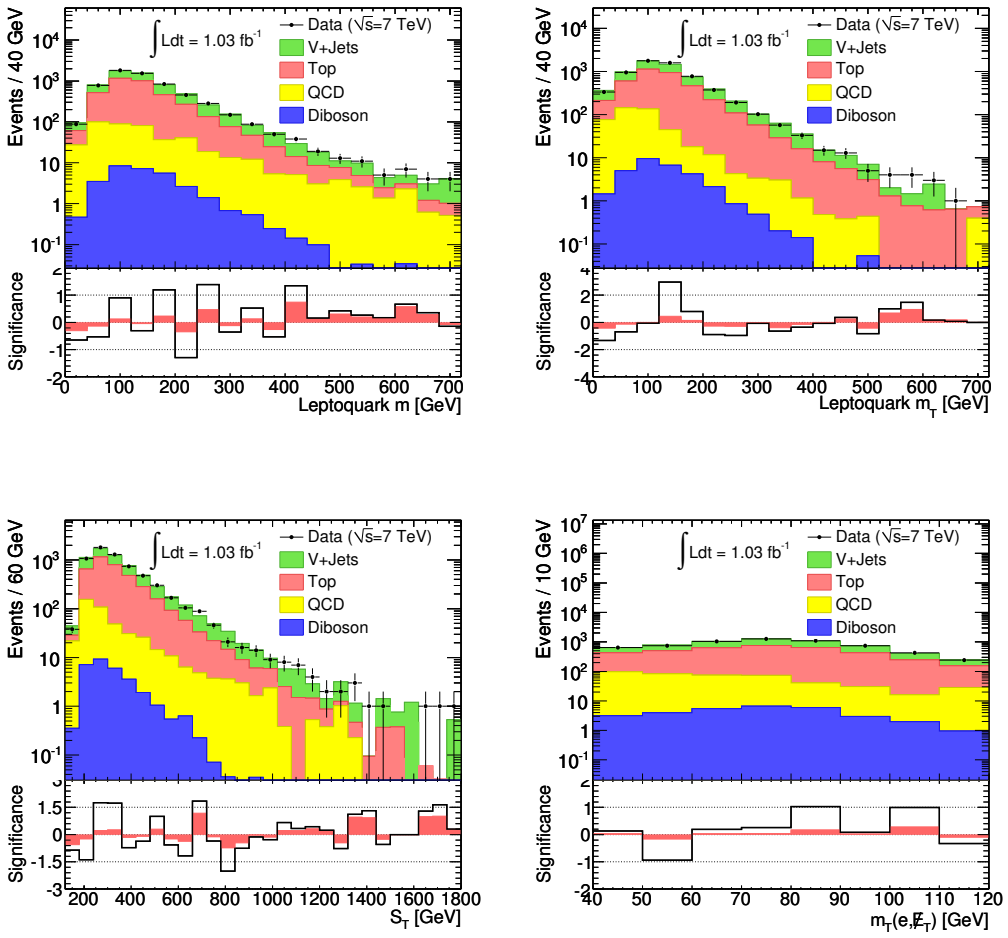

Figure 5.3: Kinematic distributions for the $t\bar{t}$ control region. LQ mass (upper left), LQ transverse mass (upper right), S_T (lower left), m_T (lower right). Backgrounds are represented by filled histograms, with colors as shown in the legend. Data corresponding to 1.03 fb^{-1} is represented by black dots. Signal is not shown as its yield is negligible. The solid line (band) in the lower plot shows the Gaussian statistical (statistical + systematic) significance of the deviation between data and predicted backgrounds.

the normalization. The final normalization used in the analysis is the average of the two estimates.

A sample of electrons enriched with fakes is obtained by relaxing the nominal electron definition, described in section 3.4. Rather than requiring electrons to fulfill the tight reconstruction requirements, only the medium electron requirements are imposed. This sample is composed of both real and fake electrons.

$$N_{medium} = N_{real} + N_{fake}^{QCD} \tag{5.5}$$

A fraction ϵ_{real} $\left(\epsilon_{fake}^{QCD}\right)$ of these real (fake) electrons will also fulfill the tight electron definition.

$$N_{tight} = \epsilon_{real} N_{real} + \epsilon_{fake}^{QCD} N_{fake}^{QCD} \tag{5.6}$$

Equations 5.5 and 5.6 can be solved to yield the expected number of electron fakes from QCD which would fulfill the nominal electron definition.

$$\epsilon_{fake}^{QCD} N_{fake}^{QCD} = \epsilon_{fake}^{QCD} \frac{\epsilon_{real} N_{medium} - N_{tight}}{\epsilon_{real} - \epsilon_{fake}^{QCD}} \tag{5.7}$$

ϵ_{real} is measured in data, binned in η. It is estimated using a tag and probe method [90, 121]. ϵ_{real} is taken as the fraction of probe electrons that pass the medium quality requirements which also pass the tight requirements, and is shown in Figure 5.4. N_{medium} and N_{tight} are determined within the analysis.

ϵ_{fake}^{QCD} is also measured in data, using a sample of events with an enhanced contribution from QCD [124]. Events are selected with exactly one electron, well separated from any jets, and small $\not{E}_T$, a signature not typically produced by the EW interaction. The number of tight electrons and the number of medium-only electrons as a function of E_T is shown in Figure 5.5. Four distinct η regions are considered separately, and the bin-by-bin ratio of the tight electron distribution to the medium-only distribution is taken as the fake rate. The observed fake rate versus electron E_T is fit with an error function as in Equation 5.8. The result of the fit for all four η regions is shown in Figure 5.6. The observed fake rates are highly symmetric in η, so the error function parameters for complimentary η regions are averaged to obtain ϵ_{fake}^{QCD} as a function of $|\eta|$.

$$\epsilon_{fake}^{QCD} = A + \frac{B}{2}\left[1 + \text{erf}\left(\frac{E_T - C}{D}\right)\right] \tag{5.8}$$

The MM gives not only the shape of the QCD background, but also the normalization. An alternative method, which is equally as valid as the MM,

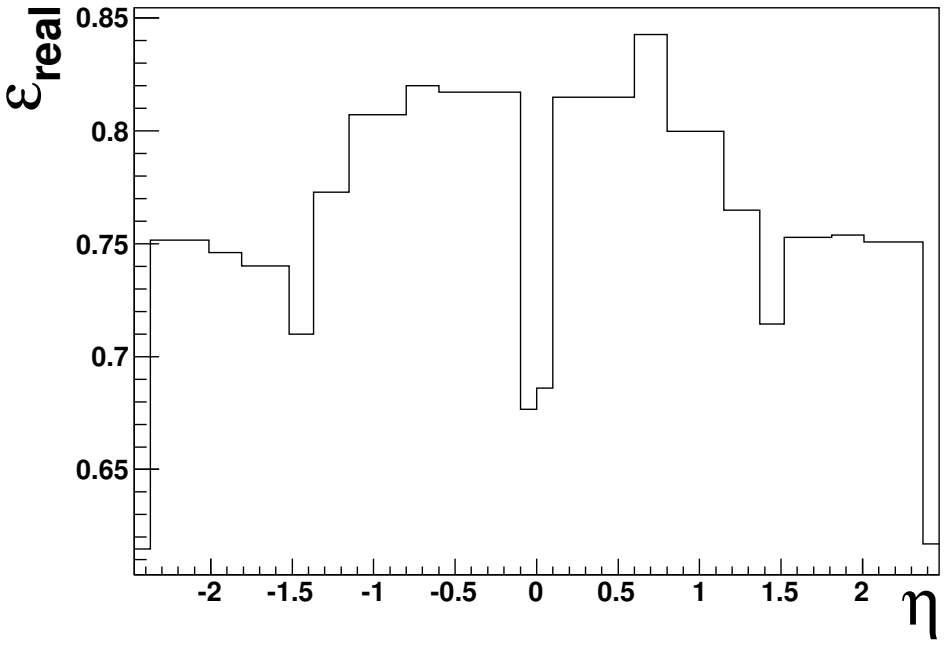

Figure 5.4: The efficiency for real electrons that pass the medium quality criteria to also pass the tight quality cuts, ϵ_{real}, as a function of η, as measured in data using a tag and probe technique in W and Z data events.

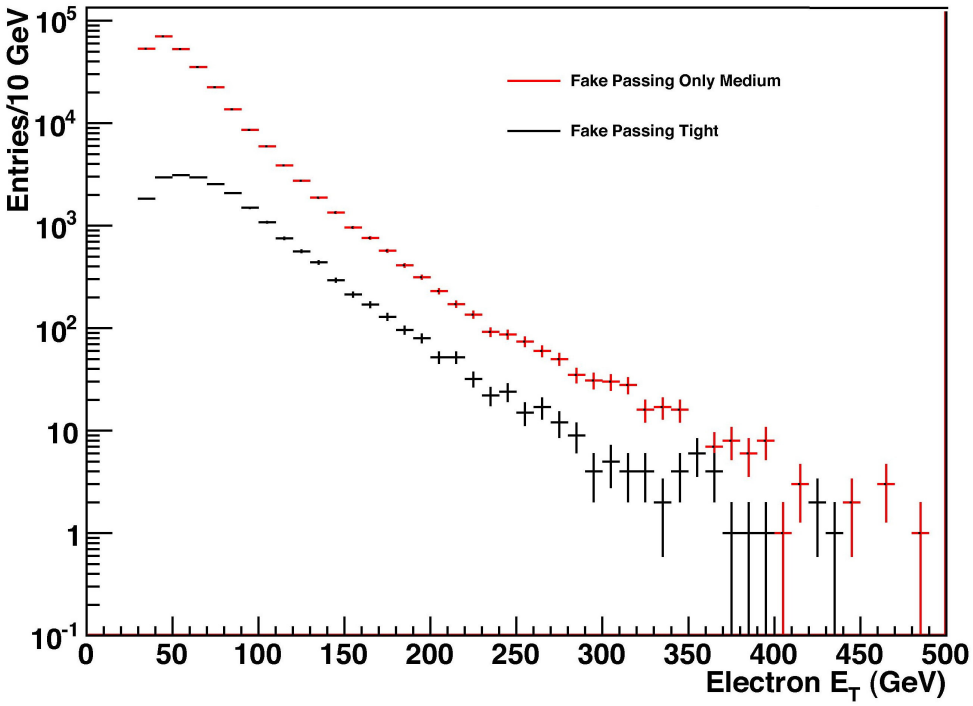

Figure 5.5: Distribution of tight and medium-only electron E_T found in a QCD enhanced data sample [124].

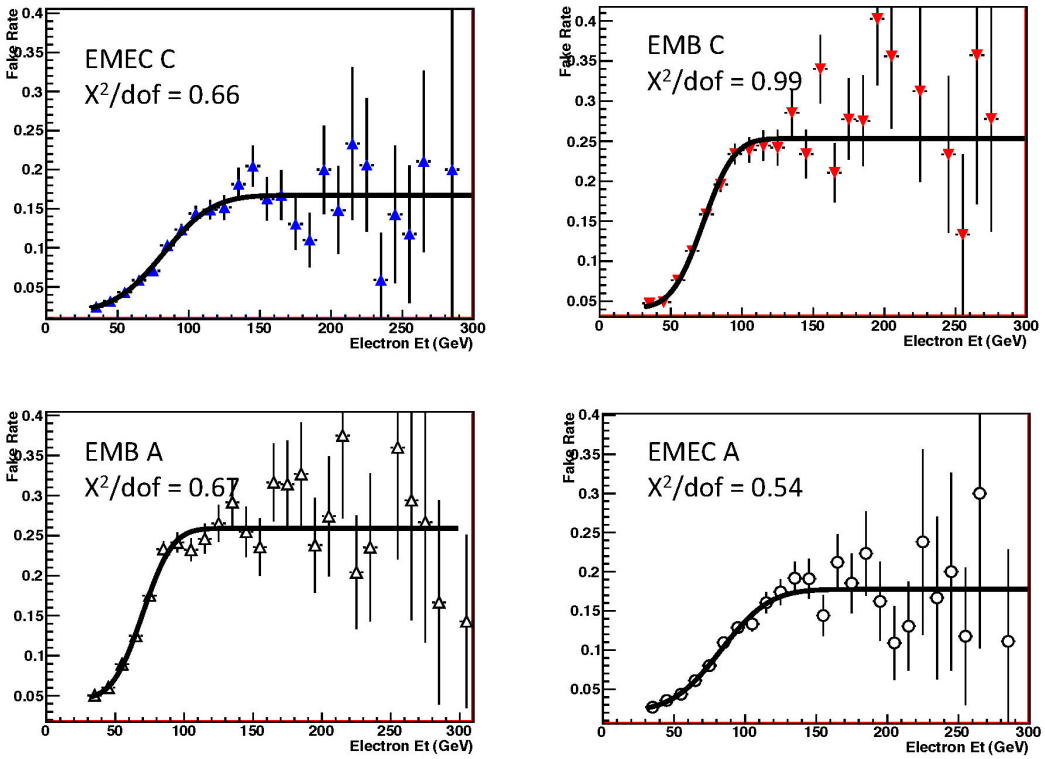

Figure 5.6: The efficiency for fake electrons that pass the medium quality criteria to also pass the tight quality cuts, ϵ_{fake}^{QCD}, as a function of electron E_T, as measured in a QCD enhanced data sample. The solid lines show the result of the fit to data. Endcap side C (upper left), barrel side C (upper right), barrel side A (lower left), endcap side A (lower right) [124].

is also used to derive a QCD normalization. The normalizations from the two methods are averaged to determine the final QCD normalization used throughout the analysis. The alternative method consists of using the QCD shape obtained from the MM to perform a binned likelihood fit to the $\not\!\!E_T$ distribution observed in data. The sum of QCD plus all other backgrounds is constrained to equal that of the data. However, the relative proportion of the QCD background is allowed to float. The QCD fraction which minimizes the log-likelihood

$$LL = -\sum_{bins} \log[P(N_i^{data}; N_i^{expected})], \tag{5.9}$$

where $P(N_i^{data}; N_i^{expected})$ is the probability to observe a fluctuation in data at least as extreme as N_i^{data} ($\geq N_i^{data}$ for an upward fluctuation, $\leq N_i^{data}$ for a downward fluctuation) assuming a Poisson distribution with a mean of $N_i^{expected}$, is taken as the alternative QCD normalization. Since the fake rate is quite different in the central and endcap regions, the fits are performed separately for each region. The derivation of the QCD shape and normalization is done separately for selected events and each CR since the QCD contribution varies considerably. The resulting fits for the $t\bar{t}$ CR are shown in figure 5.7, and yields for each CR are shown in Table 5.8.

5.5.3 V+jets and $t\bar{t}$ Scale Factors

In order to constrain the normalizations of the major backgrounds, a simultaneous χ^2 fit is performed to the predicted and observed event yields across all three CRs. The χ^2, given by

$$\chi^2\left(SF^{t\bar{t}}, SF^{V+jets}\right) = \sum_{CR}\left[\frac{O_i - P_i}{\sigma_i}\right]^2, \tag{5.10}$$

where O_i is the number of data events observed in CR i, $P_i \equiv SF^{t\bar{t}} \times MC_i^{t\bar{t}} + SF^{V+jets} \times MC_i^{V+jets} + MC_i^{other\ backgrounds}$ is the number of predicted events in CR i, and $\sigma_i = \sqrt{O_i}$, is minimized by simultaneously varying the $t\bar{t}$ and V+jets scale factors, $SF^{t\bar{t}}$ and SF^{V+jets} respectively. The resulting scale factors are shown in Table 5.7.

The V+jets SF deviates significant from unity. This is due to mis-modeling of pileup interactions in the MC, which increases the W+jets acceptance above its true value. As a cross-check, the SFs were also derived by considering only events with the S_T or the second leading jet p_T above a given threshold, thereby reducing sensitivity to pileup modeling. As these thresholds are increased, the V+jets SF tends toward unity until the statistics become scarce and the results

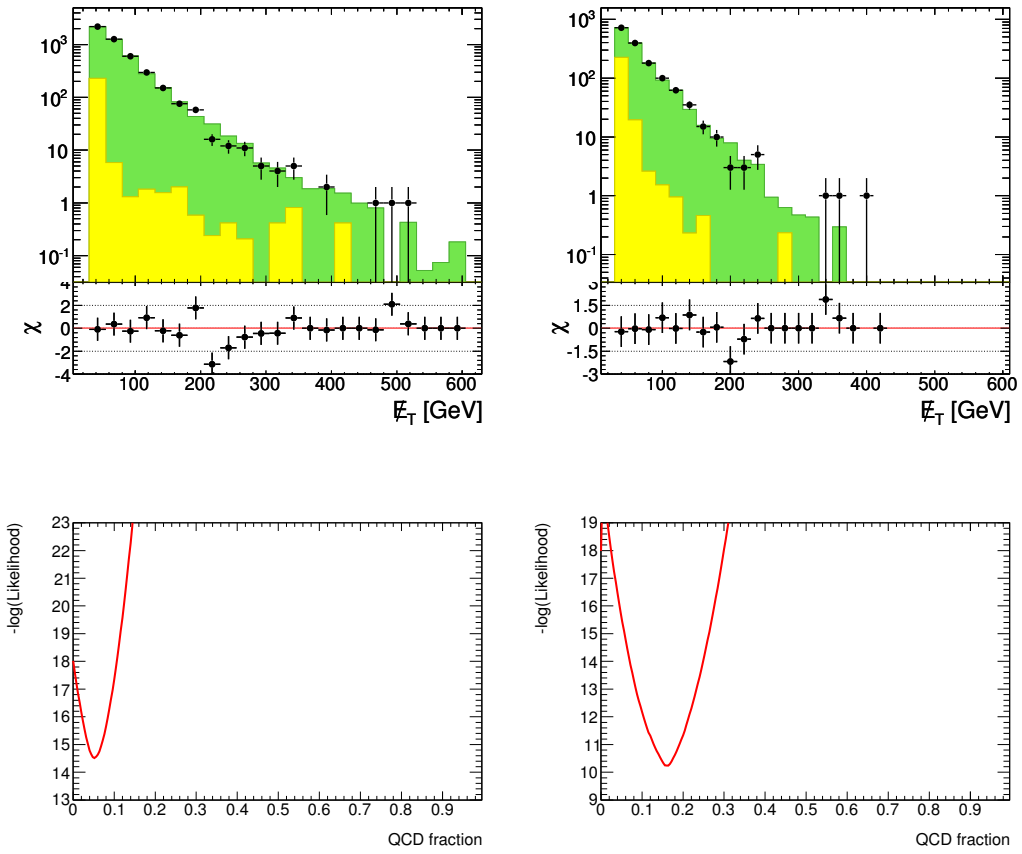

Figure 5.7: The $\not\!\!E_T$ distributions used to determine the QCD normalization for the $t\bar{t}$ CR. The QCD shape template derived from the MM is represented by the yellow filled histogram. The MC backgrounds are represented by the green filled histogram. Data is represented by black dots. The χ distribution shows the Gaussian statistical significance of the deviation between data and predicted backgrounds. The lower plots show the the log-likelihood distribution for various choices of QCD normalization. The left (right) plots are for events where the electron falls in the central (endcap) region.

$SF^{t\bar{t}}$	1.035 ± 0.026
SF^{V+jets}	0.884 ± 0.005
$\frac{\chi^2}{dof}$	$\frac{6.5}{1}$
correlation	-0.30

Table 5.7: Background scale factors derived from a simultaneous χ^2 fit. Also shown is the χ^2 of the fit and correlation between V+jets and $t\bar{t}$ scale factors.

become unstable, as seen in Figure 5.8.

The $t\bar{t}$ SF is less sensitive to pileup modeling due to the larger jet multiplicity, and thus does not deviate significantly from unity.

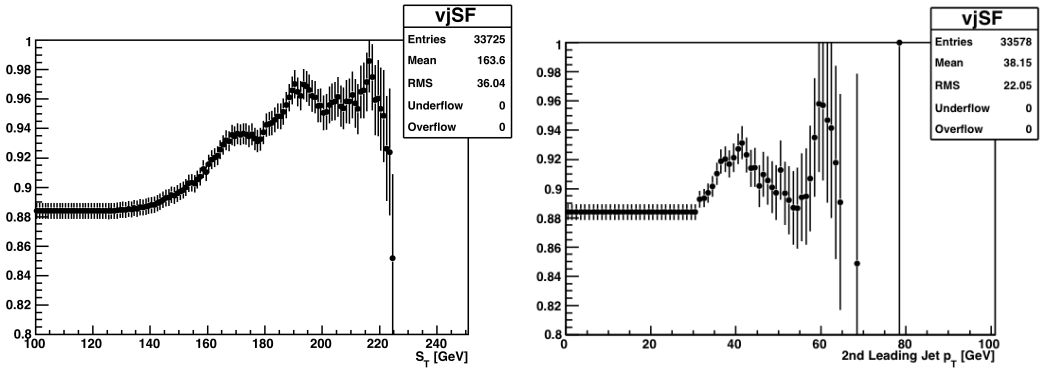

Figure 5.8: V+jets SF vs S_T threshold (left) and second leading jet p_T threshold (right) used to derive SF. As the thresholds are increased, the SF becomes less sensitive to pileup modeling, and tends toward unity (until statistics become scarce and the results become unreliable) [125].

5.6 Event Selection

Event selection requirements, listed below, are defined to ensure high signal acceptance. The final cuts, on the $\not\!\!E_T$ isolation, are designed to reduce the contribution of events from QCD in which jet energy mis-measurement leads to significant fake $\not\!\!E_T$. The effect of these cuts on signal and the QCD background are shown in Figure 5.9. Selected event yields are dominated by backgrounds, and data yields are found to agree well with expectations, as shown in Table 5.9. The QCD prediction is derived according to the procedure described in Section 5.5.2. SFs for the V+jets and $t\bar{t}$ backgrounds, as

Source	V+2 Jets	V+3 Jets	$t\bar{t}$
$W \to e\nu$+jets	[30424 ± 122]	[4575 ± 40]	[2422 ± 23]
	26895 ± 108	4044 ± 35	2141 ± 20
$W \to \tau\nu$+jets	[445 ± 14]	[64 ± 15]	[57 ± 21]
	393 ± 13	56 ± 13	51 ± 18
$Z \to ee$+jets	[1327.4 ± 8.9]	[328.5 ± 4.3]	[187.0 ± 3.7]
	1173.4 ± 7.9	290.4 ± 3.8	165.3 ± 3.3
$Z \to \tau\tau$+jets	[77.9 ± 2.8]	[18.0 ± 1.4]	[13.5 ± 1.3]
	68.9 ± 2.4	15.9 ± 1.2	12.0 ± 1.1
$t\bar{t}$	[363.2 ± 1.2]	[720.0 ± 1.6]	[3075.2 ± 3.3]
	375.8 ± 1.2	744.9 ± 1.7	3181.6 ± 3.4
Single Top	394.9 ± 1.9	126.7 ± 1.2	171.6 ± 1.3
Diboson	385.6 ± 1.9	77.18 ± 0.81	30.86 ± 0.50
QCD	3642 ± 487	1040 ± 34	412 ± 82
Total Background	[37060 ± 502]	[6949 ± 55]	[6369 ± 88]
	33329 ± 499	6395 ± 49	6165 ± 85
Data	33500	6164	6216
LQ (550 GeV)	0.0 ± 0.0	0.0 ± 0.0	0.30 ± 0.01
LQ (600 GeV)	0.0 ± 0.0	0.0 ± 0.0	0.13 ± 0.00
LQ (650 GeV)	0.0 ± 0.0	0.0 ± 0.0	0.07 ± 0.00

Table 5.8: Predicted and observed event yields in the background control regions. Values enclosed by square brackets do not include the background SFs. Uncertainties are statistical only.

described in Section 5.5.3, are applied to selected events. Basic kinematic observables for selected events, including electron E_T and η, $\not\!\!E_T$, jet multiplicity, and the p_T and η of the first and second leading jets, are shown in Figures 5.10 and 5.12.

- Good detector status
- Primary vertex with $N_{tracks} \geq 3$
- 20 GeV electron trigger
- $N_{electrons} = 1$
- $N_{muons} = 0$
- $\not\!\!E_T \geq 30$ GeV
- $m_T \geq 40$ GeV
- $N_{jets} \geq 2$
- $\Delta\phi\left(\not\!\!E_T, jet_i\right) \geq 4.5\left(1 - \frac{\not\!\!E_T}{45\text{ GeV}}\right)$

5.7 Log-Likelihood Ratio Discriminant

A multivariate technique is used to determine if the LQ signal is present in the data. A set of variables is chosen which discriminate between signal and background, shown in Figure 5.14. Probability distribution functions are formed for each of these variables, separately for signal and background events. On an event-by-event basis, a signal (background) likelihood is calculated as the product of the probabilities for a signal (background) event to posses the observed values of the four discriminating variables, as shown in Equations 5.11 and 5.12. Due to low statistics in the tails of the background probability distribution functions, an exponential function is fit to the tails, and the contents of any bins whose relative uncertainty is greater than 10% are replaced with the value of the fit, as shown in Figure 5.16. For each LQ mass hypothesis m_{LQ}, signal likelihoods L_S are derived, allowing a mass-dependent optimization.

$$L_S\left(m_{LQ}\right) \equiv \prod_{i=1}^{4} P_S^i\left(m_{LQ}\right) \tag{5.11}$$

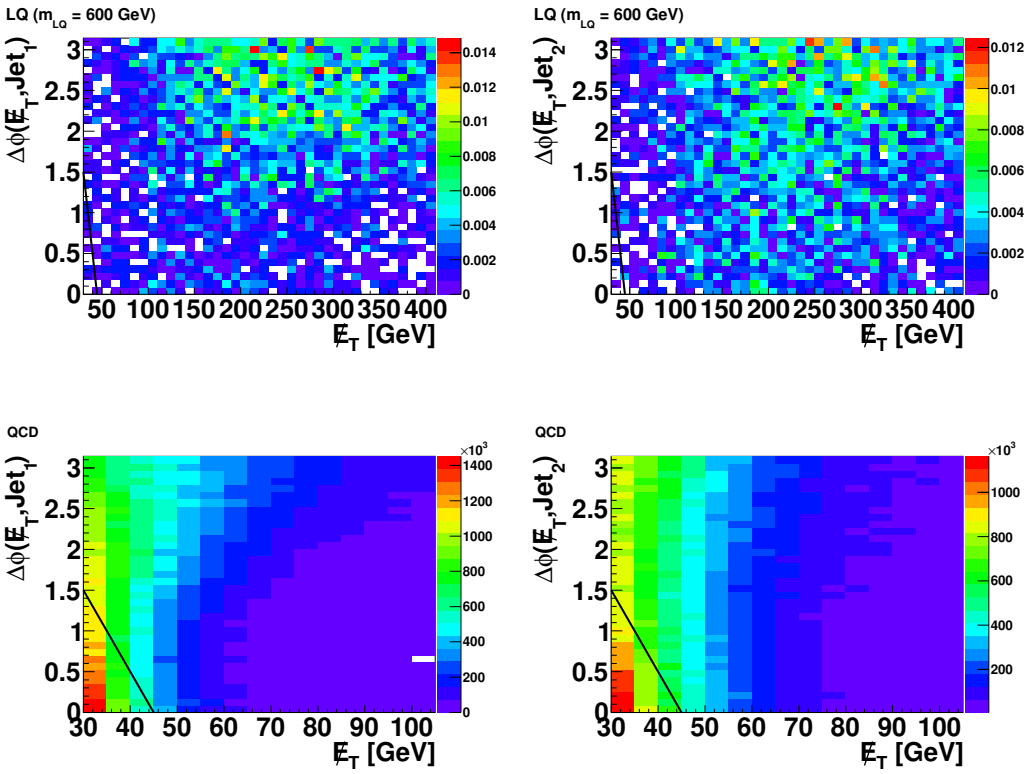

Figure 5.9: The effect of the $\not\!\!E_T$ isolation cuts on a $m_{LQ} = 600$ GeV signal (top) and the QCD background (bottom). The effect of the $\Delta\phi\left(\not\!\!E_T, jet_1\right)$ cut is shown on the left, after having applied the jet multiplicity cut. The effect of the $\Delta\phi\left(\not\!\!E_T, jet_2\right)$ cut is shown on the right, after having applied the $\Delta\phi\left(\not\!\!E_T, jet_1\right)$ cut. Events falling in the region below the black line in the $\Delta\phi\left(\not\!\!E_T, jet_i\right)$ versus $\not\!\!E_T$ plane are removed by these cuts.

Source	Trigger	Electron	$\not\!\!E_T$	m_T	Full Selection
$W \to e\nu$+jets	4830741	2476124	1770384	1748602	53703
	± 2271	± 1980	± 1770	± 1768	± 128
$W \to \tau\nu$+jets	175949	31790	17865	13274	936
	± 587	± 241	± 174	± 160	± 15
$Z \to ee$+jets	683783	252215	20520	11012	2320
	± 156	± 147	± 34	± 25	± 11
$Z \to \tau\tau$+jets	44982	10382	3118	1374	151.4
	± 71	± 35	± 18	± 11	± 3.6
$t\bar{t}$	28031.9	16766.5	11915.7	9633.0	8137.2
	± 8.8	± 7.4	± 6.4	± 5.9	± 5.4
Single Top	7738.2	4558.7	3199.7	2775.4	1591.5
	± 6.6	± 5.9	± 5.1	± 4.8	± 3.9
Diboson	8818.7	4882.0	2875.2	2583.2	852.5
	± 7.8	± 6.5	± 5.1	± 4.9	± 2.8
QCD	—	—	—	—	6678
					± 821
Total Bkg.	5780044	2796717	1829879	1789254	74371
	± 2352	± 2000	± 1779	± 1775	± 832
Data	51168720	4052065	2172582	2088106	76855
LQ (550 GeV)	11.47	9.62	9.45	9.00	8.12
	± 0.02	± 0.04	± 0.04	± 0.04	± 0.04
LQ (600 GeV)	6.09	5.14	5.07	4.84	4.39
	± 0.01	± 0.02	± 0.02	± 0.02	± 0.02
LQ (650 GeV)	3.3	2.75	2.72	2.61	2.39
	± 0.0	± 0.01	± 0.01	± 0.01	± 0.01

Table 5.9: Predicted and observed event yields after select cuts in the cut flow, and for the full event selection. Not all cuts are listed. The total background prediction does not include QCD until the full selection has been applied, therefore predicted and observed yields do not agree earlier in the cut flow. Uncertainties are statistical only.

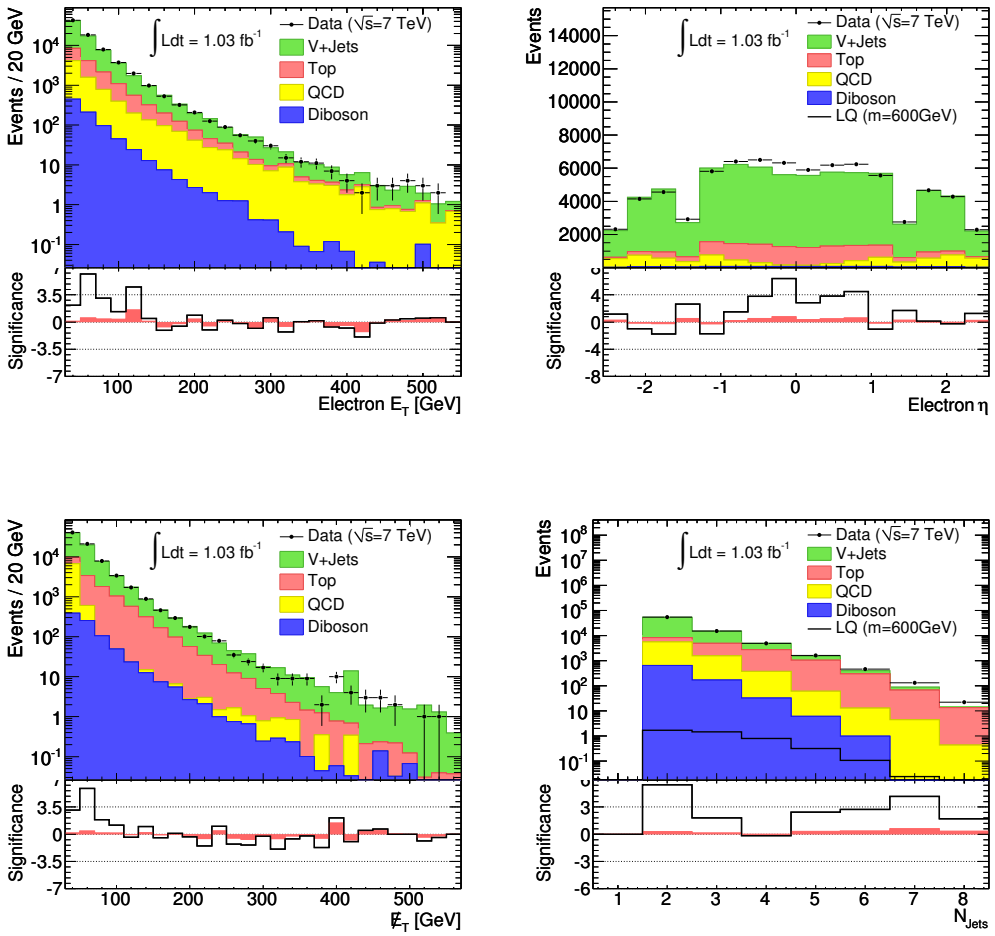

Figure 5.10: Basic kinematic distributions for selected events. Electron E_T (upper left), electron η (upper right), $\not\!\!E_T$ (lower left), and jet multiplicity (lower right) are shown. Backgrounds are represented by filled histograms, with colors as shown in the legend. Data corresponding to 1.03 fb^{-1} is represented by black dots. The 600 GeV LQ signal is represented by a solid line. The solid line (band) in the lower plot shows the Gaussian statistical (statistical + systematic) significance of the deviation between data and predicted backgrounds.

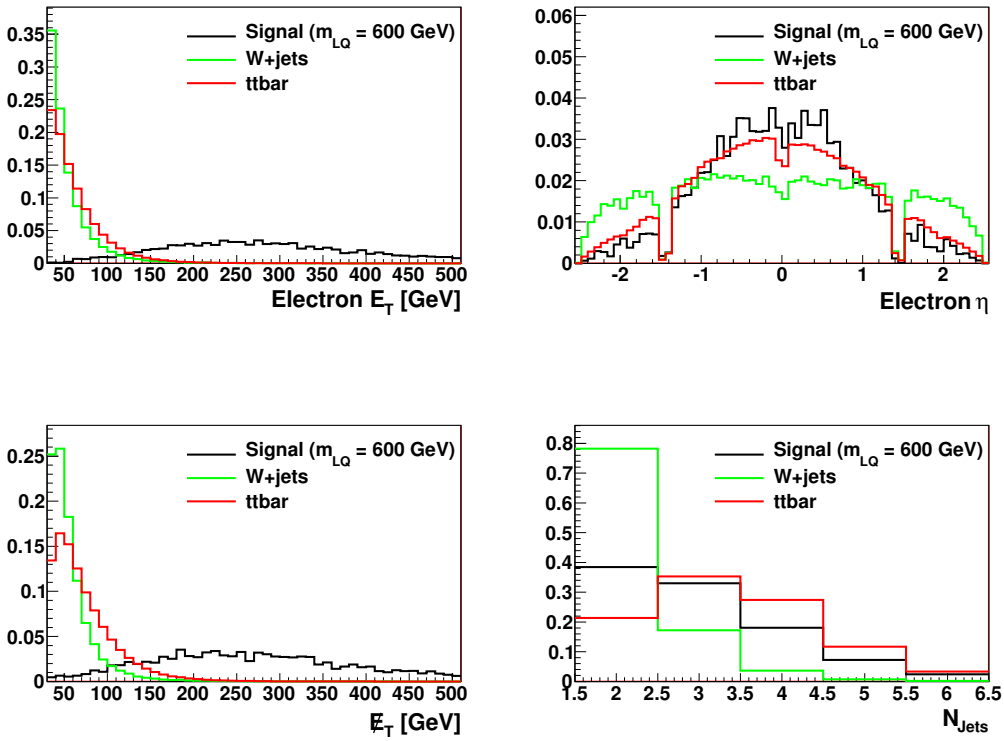

Figure 5.11: Basic kinematic distribution shapes for selected events. Electron E_T (upper left), electron η (upper right), $\not\!\!E_T$ (lower left), and jet multiplicity (lower right) are shown. The 600 GeV LQ signal is represented by a black histogram, and the W+jets ($t\bar{t}$) background is represented by a green (red) histogram. All distributions are normalized to unit area.

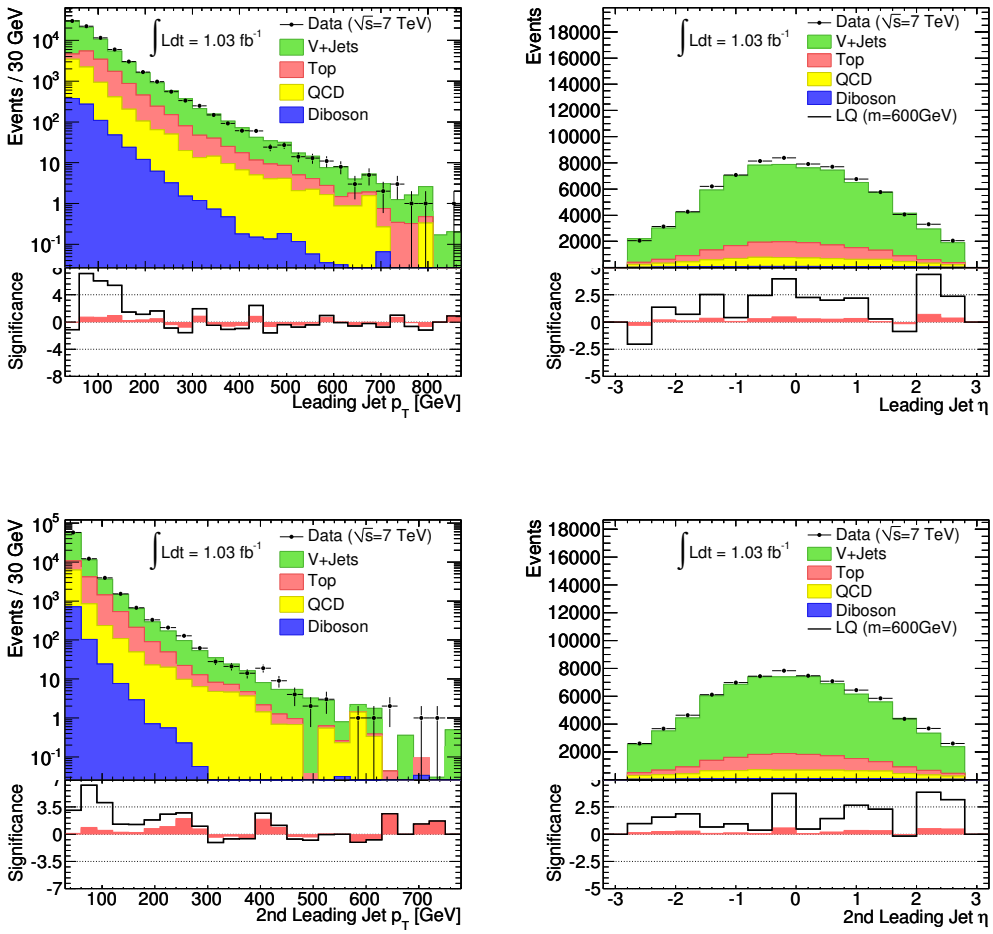

Figure 5.12: Basic jet related distributions for selected events. Leading jet p_T (upper left), leading jet η (upper right), second-leading jet p_T (lower left), and second-leading jet η (lower right) are shown. Backgrounds are represented by filled histograms, with colors as shown in the legend. Data corresponding to 1.03 fb^{-1} is represented by black dots. The 600 GeV LQ signal is represented by a solid line. The solid line (band) in the lower plot shows the Gaussian statistical (statistical + systematic) significance of the deviation between data and predicted backgrounds.

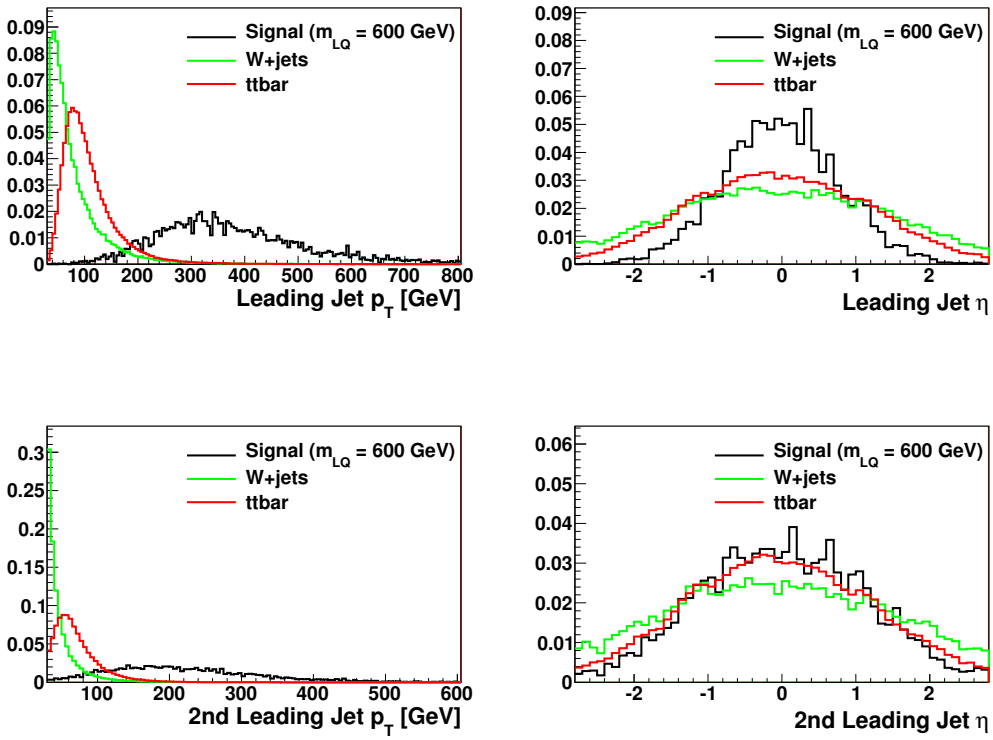

Figure 5.13: Basic jet related distribution shapes for selected events. Leading jet p_T (upper left), leading jet η (upper right), second-leading jet p_T (lower left), and second-leading jet η (lower right) are shown. The 600 GeV LQ signal is represented by a black histogram, and the W+jets ($t\bar{t}$) background is represented by a green (red) histogram. All distributions are normalized to unit area.

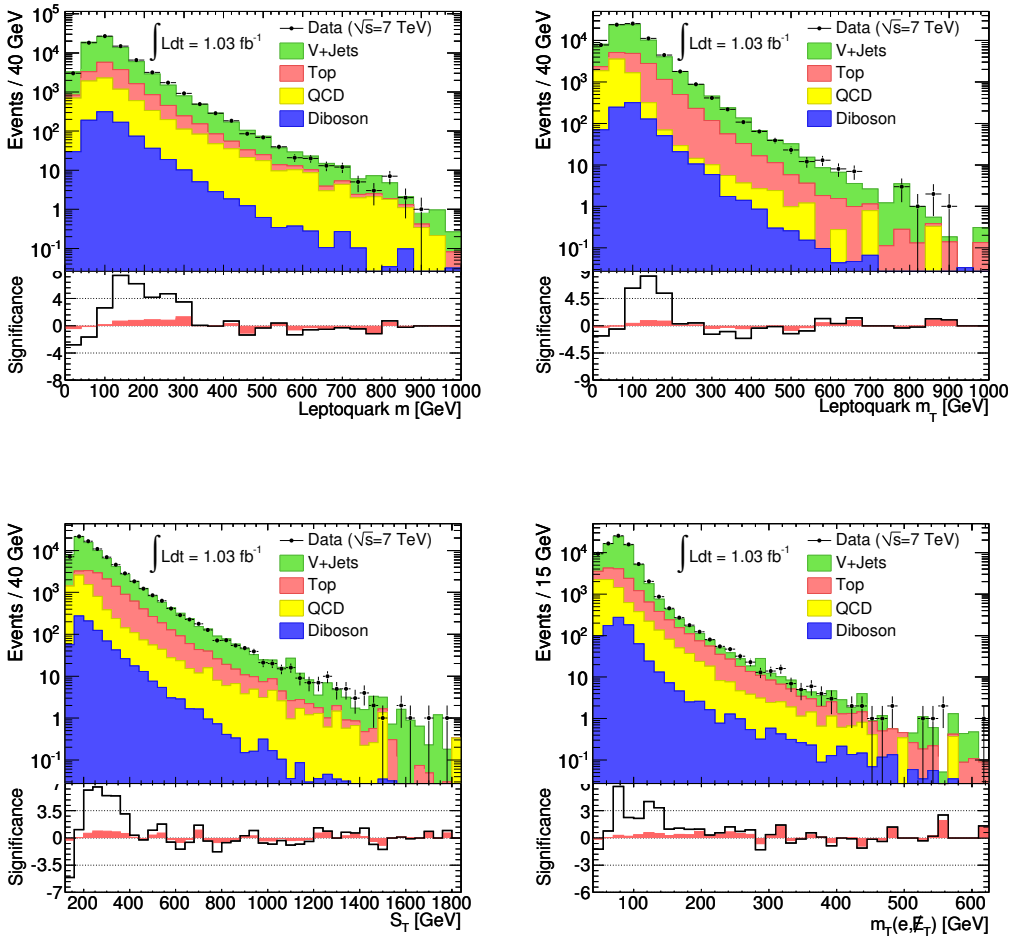

Figure 5.14: Additional kinematic distributions for selected events. LQ mass (upper left), LQ transverse mass defined in Equation 1.51 (upper right), S_T defined in Equation 5.3 (lower left), and m_T defined in Equation 5.4 (lower right) are shown. Backgrounds are represented by filled histograms, with colors as shown in the legend. Data corresponding to 1.03 fb^{-1} is represented by black dots. The 600 GeV LQ signal is represented by a solid line. The solid line (band) in the lower plot shows the Gaussian statistical (statistical + systematic) significance of the deviation between data and predicted backgrounds.

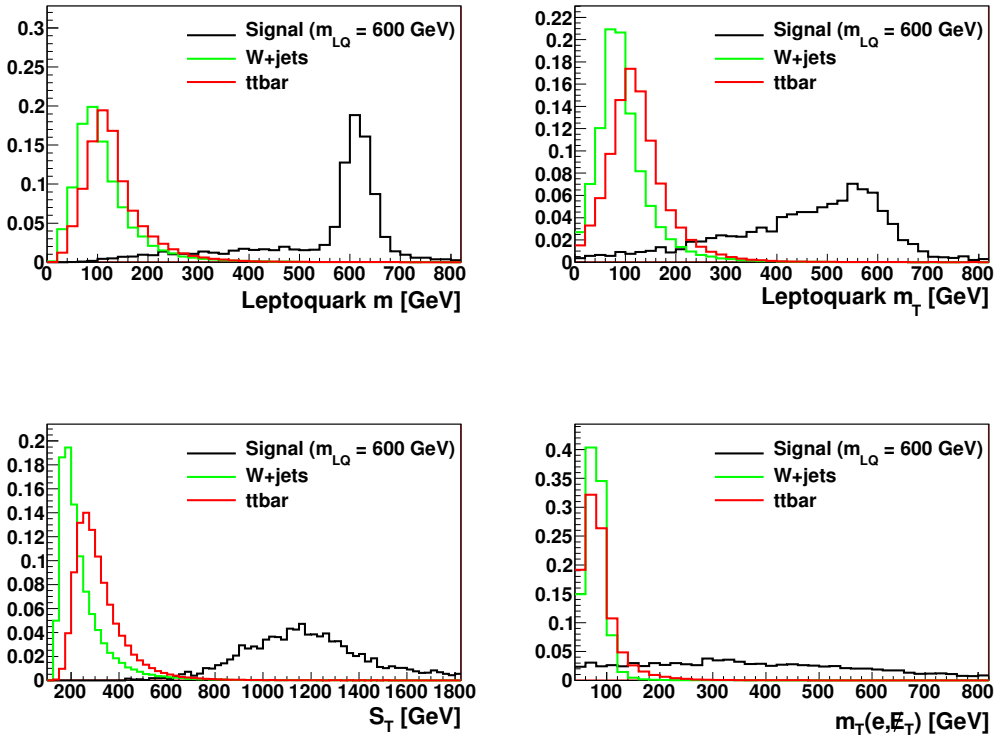

Figure 5.15: Additional kinematic distribution shapes for selected events. LQ mass (upper left), LQ transverse mass defined in Equation 1.51 (upper right), S_T defined in Equation 5.3 (lower left), and m_T defined in Equation 5.4 (lower right) are shown. The 600 GeV LQ signal is represented by a black histogram, and the W+jets ($t\bar{t}$) background is represented by a green (red) histogram. All distributions are normalized to unit area.

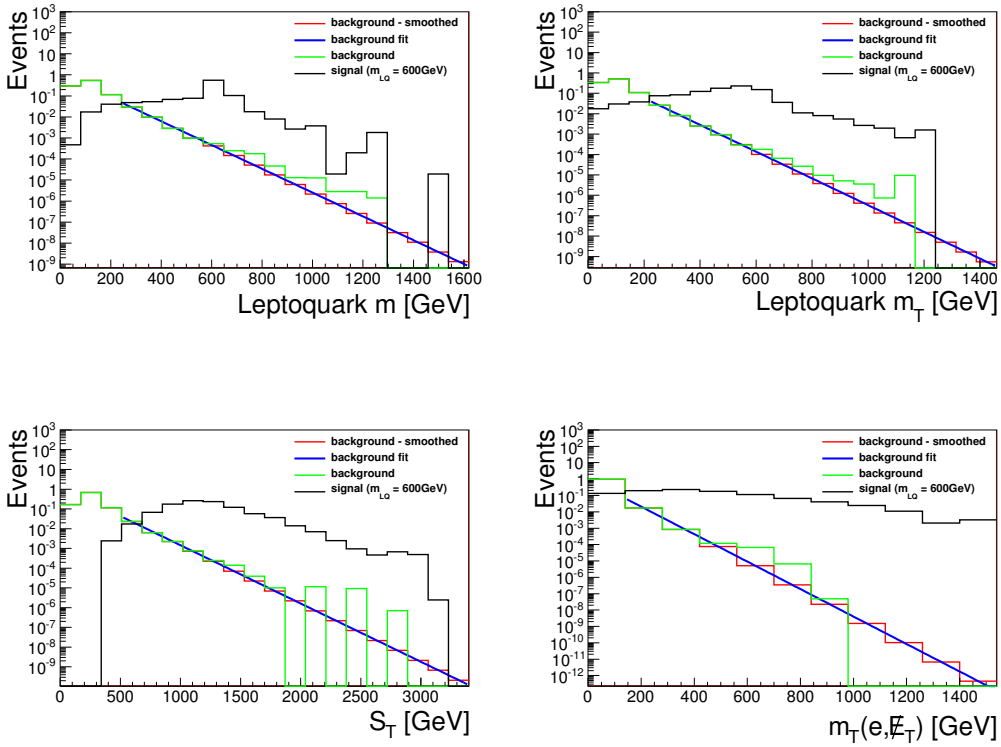

Figure 5.16: Probability distribution functions used to form signal and background likelihoods. The signal probability distribution functions are shown in black, and raw background distributions are shown in green. For the background probability distribution functions, an exponential function is fit in the tails, the result of which is shown in blue. The exponential fit is used to perform a smoothing of the background probability distribution functions, the result of which is shown in red.

$$L_B \equiv \prod_{i=1}^{4} P_B^i \tag{5.12}$$

From the signal likelihoods $L_S(m_{LQ})$ and background likelihood L_B, the log-likelihood ratio (LLR) is formed, as in Equation 5.13.

$$LLR\,(m_{LQ}) \equiv \log_{10}\left(\frac{L_S\,(m_{LQ})}{L_B}\right) \tag{5.13}$$

Signal-like events have large values of LLR, whereas background-like events have small values, as shown in Figure 5.17. The observed LLR distribution for $m_{LQ} = 600$ GeV is shown in Figure 5.18. It is these LLR distributions which are used as the final discriminant to determine if the LQ signal is present in the data. The discriminating variables for signal-like events (LLR ≥ 2) are shown in Figure 5.19, and an event display for a signal-like event is shown in Figure 5.20.

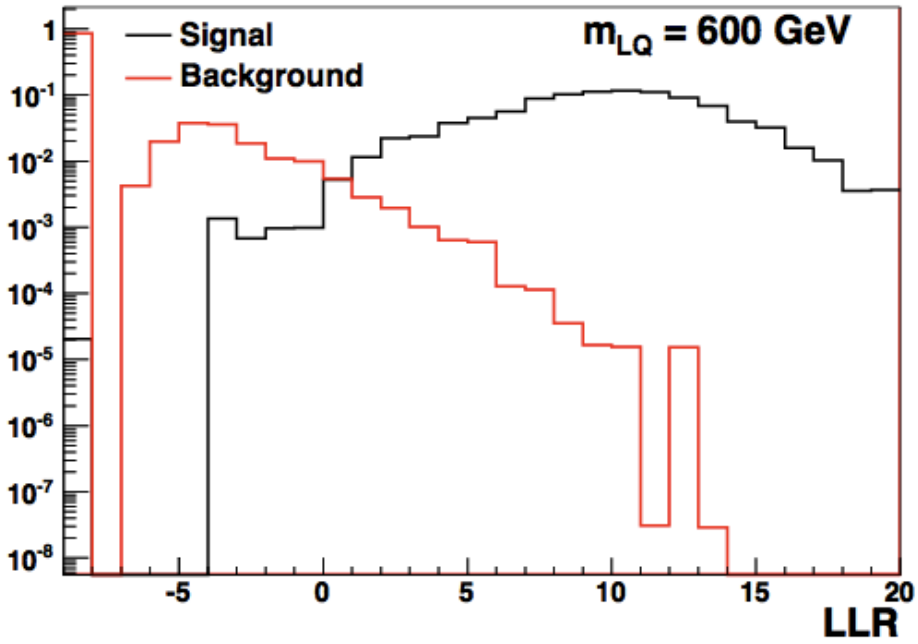

Figure 5.17: Log-likelihood ratio distribution shape assuming $m_{LQ} = 600$ GeV, for signal (black) and total background (red). The first bin is an underflow bin. Events in this bin fall in a region of phase space with no signal prediction, and therefore have $LLR = -\infty$.

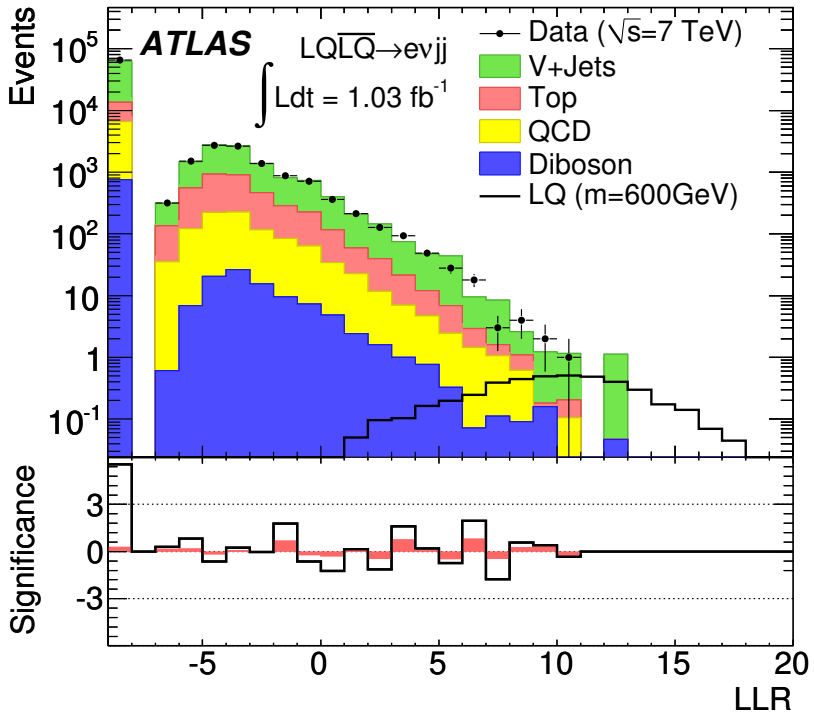

Figure 5.18: Log-likelihood ratio distribution assuming $m_{LQ} = 600$ GeV. Events in the first bin fall in a region of phase space with no signal prediction. Backgrounds are represented by filled histograms, with colors as shown in the legend. Data corresponding to 1.03 fb^{-1} is represented by black dots. The 600 GeV signal is represented by a solid line. The solid line (band) in the lower plot shows the Gaussian statistical (statistical + systematic) significance of the deviation between data and predicted backgrounds.

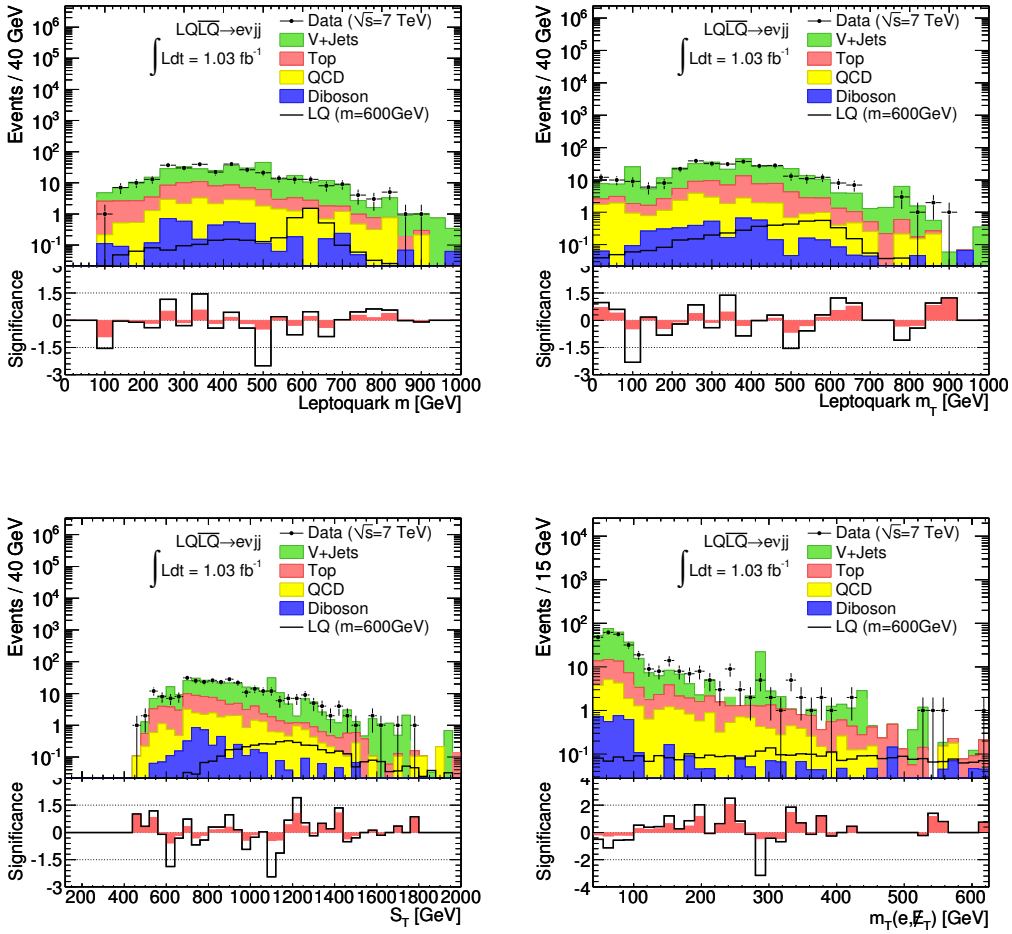

Figure 5.19: Kinematic distributions for signal-like ($LLR \geq 2$) selected events. LQ mass (upper left), LQ transverse mass defined in Equation 1.51 (upper right), S_T defined in Equation 5.3 (lower left), m_T defined in Equation 5.4 (lower right). Backgrounds are represented by filled histograms, with colors as shown in the legend. Data corresponding to 1.03 fb^{-1} is represented by black dots. The 600 GeV LQ signal is represented by a solid line. The solid line (band) in the lower plot shows the Gaussian statistical (statistical + systematic) significance of the deviation between data and predicted backgrounds.

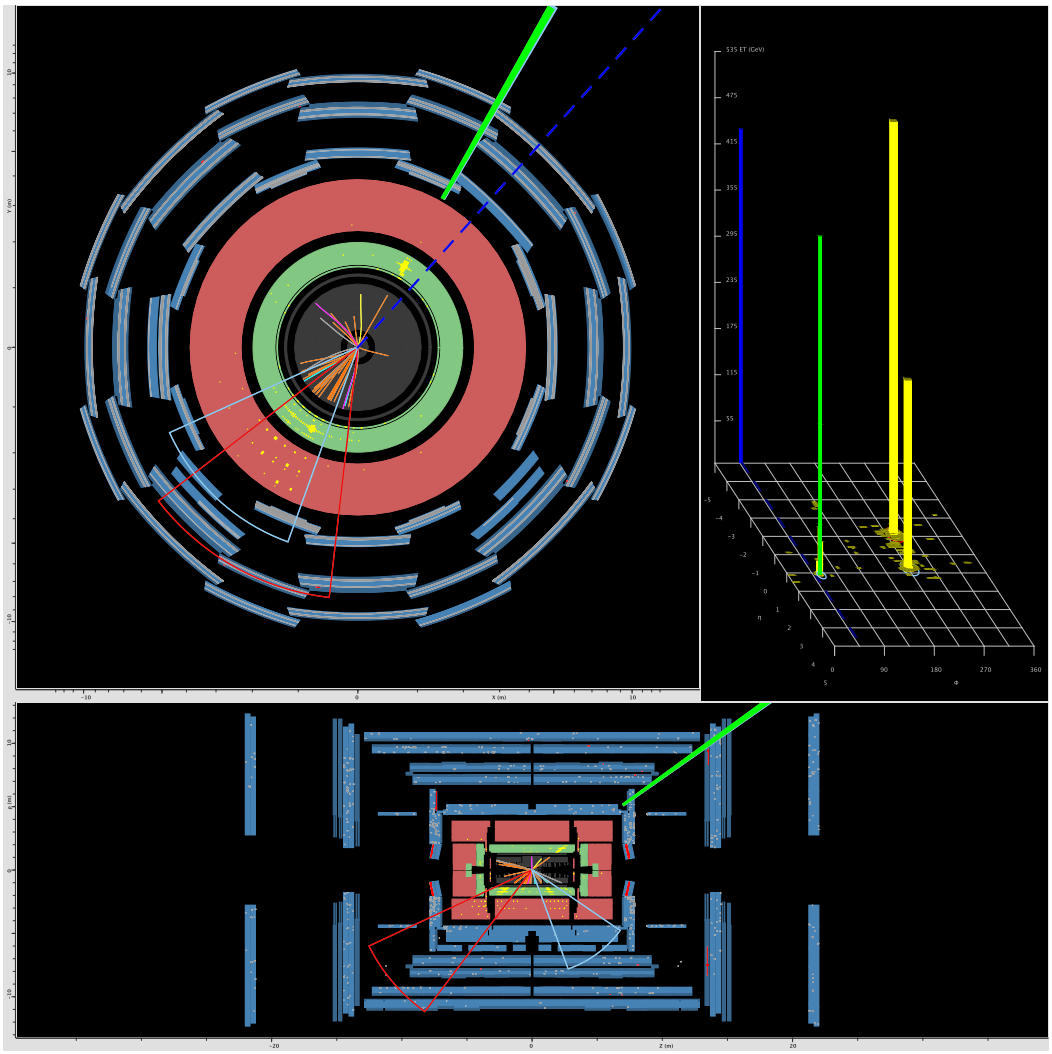

Figure 5.20: Event display for signal-like event number 58053223 from run 184169. The upper left (bottom) panel displays an R-ϕ (R-z) view of the detector. The upper right panel shows energy deposits in the η-ϕ plane. Tracks are colored according to the vertex to which they are associated, with tracks from the signal vertex in orange. Energy deposits in the calorimeter are shown in yellow. The (second) hardest jet in the event is demarcated by the (light blue) red wedge. The electron energy is represented by the green bar. The ϕ-direction of the $\not\!\!E_T$ is shown in dark blue. The observed values of the LQ mass, LQ transverse mass, S_T, and m_T are 663.5 GeV, 895.2 GeV, 1598.2 GeV, and 85.8 GeV respectively. For the $m_{LQ} = 600$ GeV mass hypothesis, these values yield $LLR = 8.8$.

Chapter 6

Systematic Uncertainties

A systematic mis-modeling of any aspect of the simulated MC events would lead to inaccurate signal and background predictions. Many potential sources of systematic uncertainty are considered in this analysis and accounted for in the final result. Systematic uncertainties related to the selection of electrons, and the scale and resolution of electron and jet energies are evaluated. Modeling uncertainty of the dominant W+jets and $t\bar{t}$ backgrounds is considered. The effect of the uncertainty in the background normalization is calculated. The systematic uncertainty related to the choice of signal PDF is evaluated. Statistical uncertainty in the probability distribution functions due to finite MC statistics is accounted for in the final result. Finally, an uncertainty related to the luminosity measurement is included.

For each source of uncertainty considered, a systematically varied LLR distribution is obtained. These alternate LLR distributions are used in the limit setting procedure to account for the various sources of systematic uncertainty, as described in Chapter 7. A convenient measure of the impact of the various systematics, but which is not used directly in the limit setting procedure, is given by the fractional change in the LLR distribution, defined by

$$\Delta LLR = \frac{\sum\limits_{bins} \frac{1}{2} \left(|\delta LLR_{+1\sigma}| + |\delta LLR_{-1\sigma}| \right)}{N_{events}}, \tag{6.1}$$

where $\delta LLR_{\pm 1\sigma}$ is the bin-by-bin change in the LLR distribution when calculated with a $\pm 1\sigma$ systematic variation. These ΔLLR values are summarized in Table 6.1 for signal and all background sources.

Systematic	W+jets	Z+jets	$t\bar{t}$	Single Top	Diboson	QCD	LQ Signal
Electron Eff. SF	0.027	0.031	0.025	0.030	0.030	–	0.060
Electron Energy Scale	0.027	0.032	0.014	0.022	0.024	–	0.060
Electron Energy Res.	<0.01	0.015	<0.01	0.012	<0.01	–	0.057
Jet Energy Scale	0.169	0.132	0.038	0.051	0.124	–	0.081
Jet Energy Res.	0.116	0.260	0.032	0.057	0.097	–	0.083
Top Mass	–	–	0.036	–	<0.01	–	–
ISR/FSR	–	–	0.061	–	<0.01	–	–
POWHEG/MC@NLO	–	–	0.068	–	<0.01	–	–
PYTHIA/HERWIG	–	–	0.037	–	<0.01	–	–
SHERPA/ALPGEN	0.022	0.010	–	–	–	–	–
MJ Normalization	–	–	–	–	–	0.200	–
PDF, signal	–	–	–	–	–	–	0.067
LLR Input pdf	0.024	0.025	0.073	0.045	0.032	0.043	0.025
Luminosity	–	–	–	0.037	0.037	–	0.037
Data Normalization	0.100	0.100	0.026	–	–	–	–
Total	0.23	0.31	0.14	0.10	0.17	0.20	0.17

Table 6.1: The fractional change in LLR distributions ΔLLR for all background sources and signal, assuming $m_{LQ} = 600$ GeV [119].

6.1 Electron Systematic Uncertainties

Three systematic uncertainties are associated with electrons; the efficiency of electron selection, the energy scale, and the energy resolution.

6.1.1 Electron Selection Efficiency

The electron selection efficiency corrections, described in Section 5.3.1, are associated with a number of sources of systematic uncertainty [90]. The dominant sources are related to the subtraction of background from the sample of probe electrons. To assess this systematic, the requirements on the electron tag are varied to change the amount of background present in the signal region. The background subtraction method is also varied. Several choices of discriminating variables are used, the background and signal regions are varied, and the background shape hypothesis is varied as well. A bias related to a possible correlation between the discriminating variable and selection efficiency is investigated as well. In all, around 100 distinct efficiency measurements are made with the above variations, for each of the efficiencies in Equation 5.1. The central value of the efficiency is taken from the mean of these measurements, and the systematic uncertainty is taken as the RMS of the observed values.

The impact of the electron selection efficiency uncertainty on the analysis is assessed by repeating the analysis with the electron selection scale factors varied by $\pm 1\sigma$ in MC. The LLR distribution is derived from these systematically varied events, using the nominal probability distribution functions to

evaluate the signal and background likelihoods, as described in Equations 5.11 and 5.12. The effect on the electron E_T, electron η, m_T, and LLR distributions for the total background is shown in Figure 6.1. The ΔLLR caused by the selection efficiency systematic for signal and background sources is shown in Table 6.1.

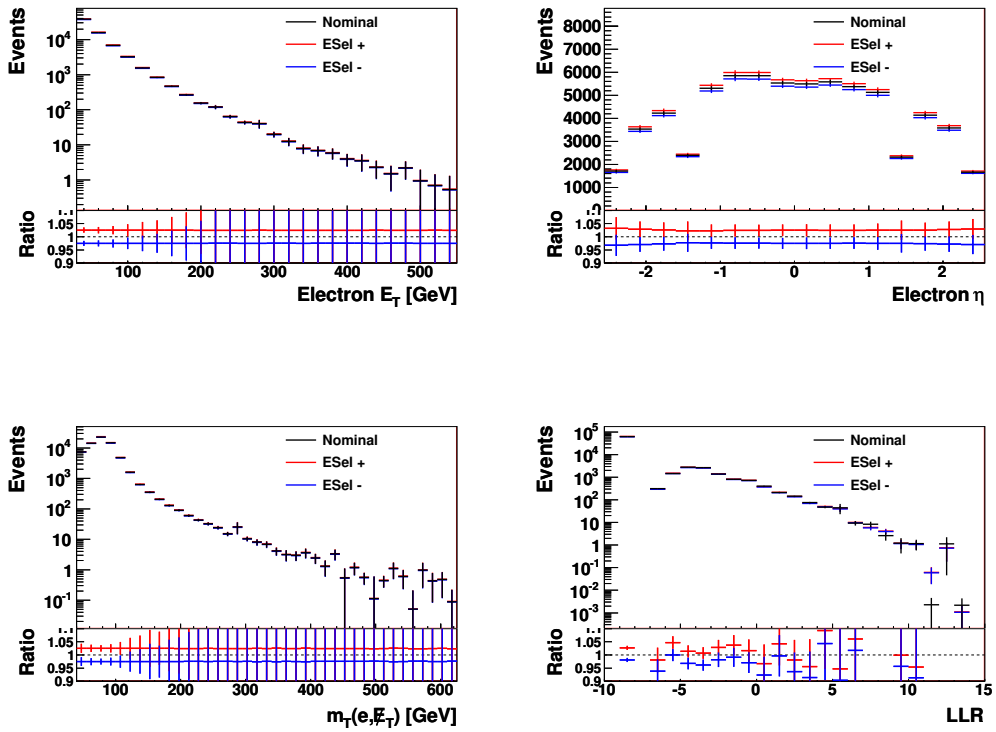

Figure 6.1: The electron E_T, electron η, m_T, and LLR distributions for the total background. The LLR distribution assumes $m_{LQ} = 600$ GeV. The nominal distributions are shown in black, and the distributions with a $+1\sigma$ (-1σ) change in the electron selection efficiency are shown in red (blue). The lower plots show the ratio of the systematically varied and nominal distributions.

6.1.2 Electron Energy Scale

The EES derivation, discussed in Section 3.4, is subject to a number of systematic uncertainties. The derivation of the EES systematic uncertainty is described in detail in Reference [90]. The dominant uncertainty is due to

imperfect knowledge of the detector material in front of the EMC. The uncertainty related to detector material modeling is assessed by recalculating the α_i calibration constants using a MC produced with an alternative detector model containing extra detector material. The observed systematic varies from -2% to +1.2%. Additional sources of systematic uncertainty include potential differences between the energy scales of the presampler and the EMC, potential differences between the energy scales of different EMC layers, potential nonlinearities in the readout electronics, systematics of the calibration constant determination, and uncertainties in the estimated effects from pileup interactions. The total electron energy scale uncertainty is parametrized in terms of η and E_T, and varies from 0.3% to 1.6% for the central electrons used in this analysis.

The impact of this systematic on the analysis is assessed by repeating the analysis with the energy of all electrons varied by $\pm 1\sigma$ in MC. These variations are also propagated to the $\not\!\!E_T$ calculation. The LLR distribution is derived from these systematically varied events, using the nominal probability distribution functions to evaluate the signal and background likelihoods, as described in Equations 5.11 and 5.12. The effect on the electron E_T, $\not\!\!E_T$, LQ mass, and LLR distributions for the total background is shown in Figure 6.2. The ΔLLR caused by the EES systematic for signal and background sources is shown in Table 6.1.

6.1.3 Electron Energy Resolution

The EER derivation, described in Section 5.3.2, is subject to a number of systematic uncertainties as well [90]. The dominant source of uncertainty results from the assumption that the sampling term of the resolution is well modeled in MC. The effect of this assumption was assessed by increasing the assumed sampling term by 10% and repeating the resolution determination. This leads to an η-dependent systematic of $\leq 0.4\%$. The chosen fit range was also varied to assess uncertainty related to the fit procedure. This systematic was found to be small. An uncertainty related to pileup was also considered and found to be negligible.

The impact of the EER uncertainty on the analysis is assessed by repeating the analysis in MC with the standard deviation of the Gaussian distribution used for electron energy smearing varied by the $\pm 1\sigma$ uncertainty on the EER measurement. These variations are also propagated to the $\not\!\!E_T$ calculation. The LLR distribution is derived from these systematically varied events, using the nominal probability distribution functions to evaluate the signal and background likelihoods, as described in Equations 5.11 and 5.12. The effect on the electron E_T, $\not\!\!E_T$, S_T, and LLR distributions for the total background

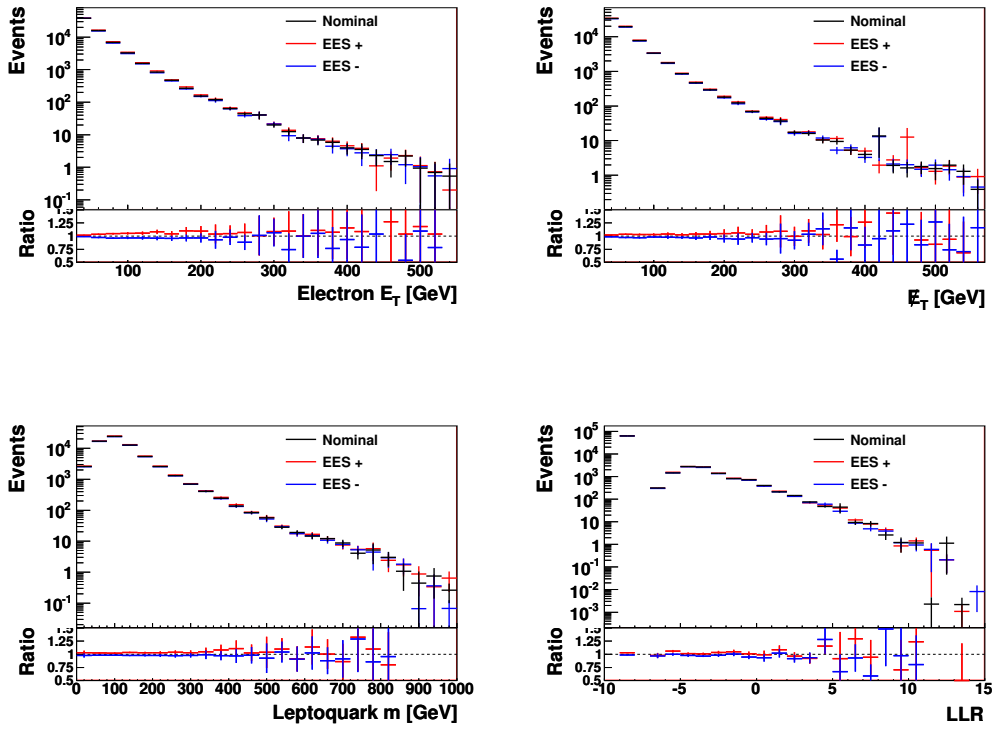

Figure 6.2: The electron E_T, $\not\!\!E_T$, LQ mass, and LLR distributions for the total background. The LLR distribution assumes $m_{LQ} = 600$ GeV. The nominal distributions are shown in black, and the distributions with a $+1\sigma$ (-1σ) change in the EES are shown in red (blue). The lower plots show the ratio of the systematically varied and nominal distributions.

is shown in Figure 6.3. The ΔLLR caused by the EER systematic for signal and background sources is shown in Table 6.1

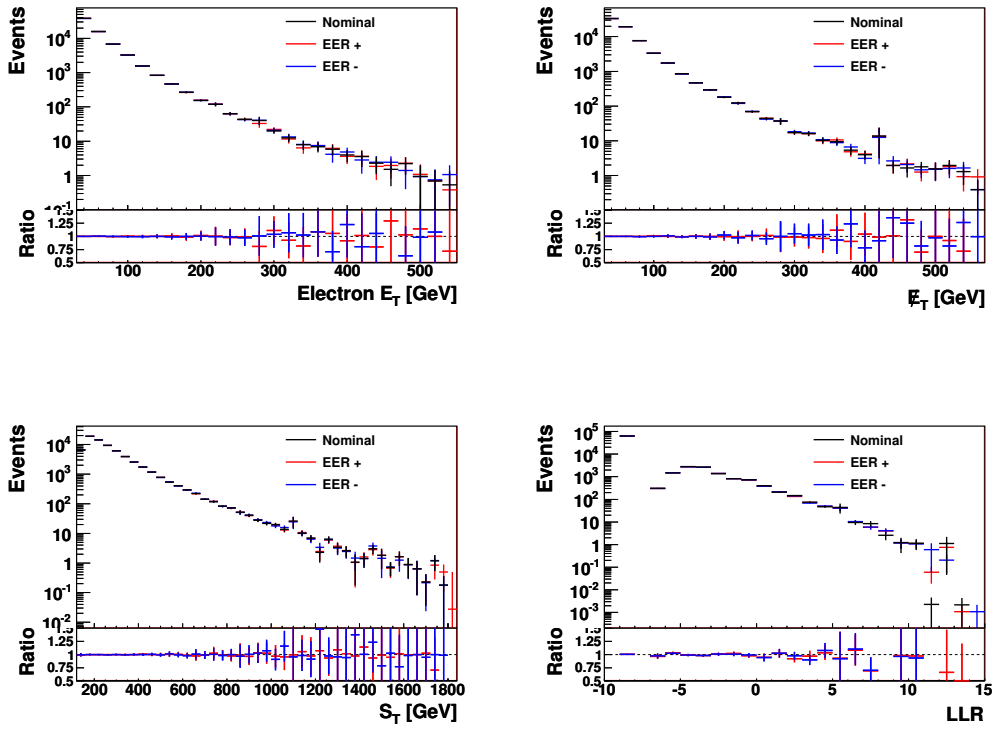

Figure 6.3: The electron E_T, $\not\!\!E_T$, S_T, and LLR distributions for the total background. The LLR distribution assumes $m_{LQ} = 600$ GeV. The nominal distributions are shown in black, and the distributions with a $+1\sigma$ (-1σ) change in the EER are shown in red (blue). The lower plots show the ratio of the systematically varied and nominal distributions.

6.2 Jet Energy Systematic Uncertainties

Two systematic uncertainties are associated with jet energy reconstruction. The first concerns the scale and the second the resolution.

6.2.1 Jet Energy Scale

The process of converting the energy of a hadronic shower from the EM scale to the JES, described in Section 3.3, is subject to a number of systematic uncertainties [87]. Uncertainty regarding the calorimeter response to hadronic jets is the dominant source. The calorimeter response to single hadrons and the associated uncertainty is measured in test-beams and MC, from which the response and uncertainty to multi-hadron jets can be inferred. This leads to a 1.5-4% p_T-dependent uncertainty. The electronic noise which is used to determine the thresholds used in topological cluster building may not be well modeled in the MC. The effect of noise mis-modeling is assessed by varying these thresholds and repeating jet reconstruction, which leads to a systematic which is $\sim$1% for jets in the range 30 GeV $\leq p_T \leq$ 40 GeV, and is negligible for jets with larger p_T. Imperfect knowledge of the detector material distribution also must be accounted for. MC samples simulated with additional detector material located in front of the calorimeter are used for this purpose.

A possible systematic due to MC modeling is also assessed. The JES as determined in PYTHIA MC samples is compared to the JES determined in samples produced with ALPGEN+HERWIG+JIMMY, and also with PYTHIA using an alternative parameter tune. The difference is treated as a systematic uncertainty. An additional p_T and $|\eta|$-dependent uncertainty is included to account for possible mis-modeling of pileup interactions, shown in Table 6.2. Finally, the JES determination, described in Section 3.3, is repeated with jets already calibrated at the JES. In this case, the average jet energy response $\langle \mathscr{R}^{jet}_{EM+JES} \rangle = E^{jet}_{EM+JES}/E^{jet}_{truth}$ should equal unity. Any deviation from unity is included as an additional systematic uncertainty.

	$p_T <$ 50 GeV	50 GeV$< p_T <$100 GeV	$p_T >$100 GeV
$\|\eta\| < 2.1$	5%	2%	0%
$\|\eta\| > 2.1$	7%	3%	0%

Table 6.2: The pileup systematic uncertainty for various jet p_T and η bins. This uncertainty is added in quadrature with the jet energy scale uncertainty.

The impact of the JES uncertainty on the analysis is assessed by repeating the analysis with the JES varied by $\pm 1\sigma$ in MC. These variations are also propagated to the $\not\!\!E_T$ calculation. The LLR distribution is derived from these systematically varied events, using the nominal probability distribution functions to evaluate the signal and background likelihoods, as described in Equations 5.11 and 5.12. The effect on the leading jet p_T, $\not\!\!E_T$, LQ mass, and LLR distributions for the total background is shown in Figure 6.4. The ΔLLR

caused by the JES systematic for signal and background sources is shown in Table 6.1

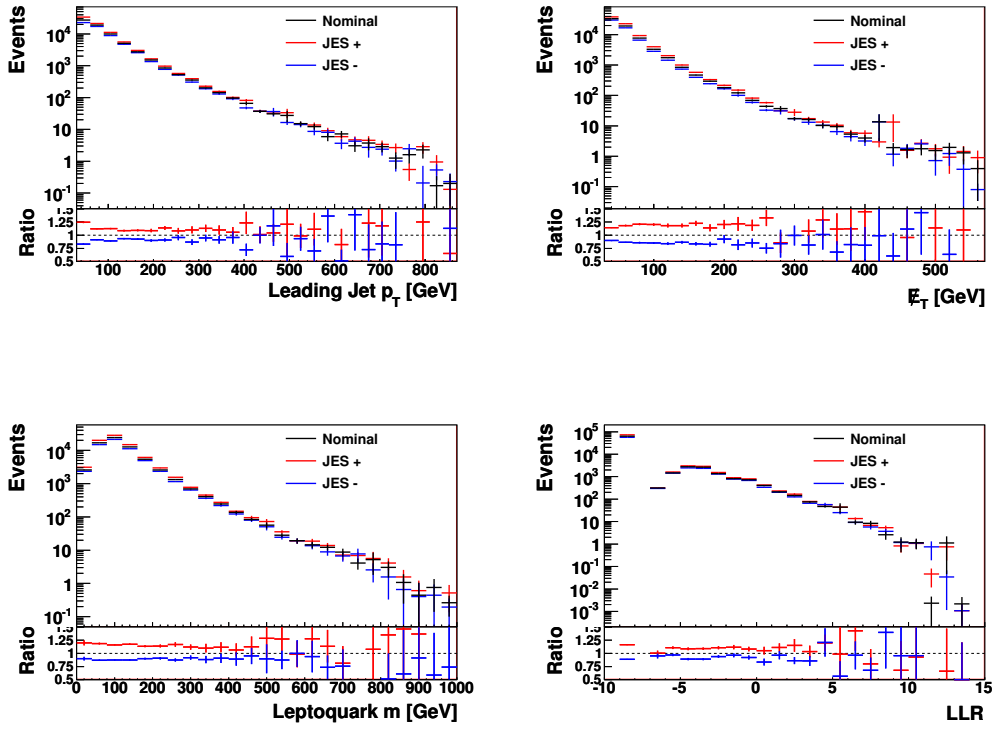

Figure 6.4: The leading jet p_T, $\not\!\!E_T$, LQ mass, and LLR distributions for the total background. The LLR distribution assumes $m_{LQ} = 600$ GeV. The nominal distributions are shown in black, and the distributions with a $+1\sigma$ (-1σ) change in the JES are shown in red (blue). The lower plots show the ratio of the systematically varied and nominal distributions.

6.2.2 Jet Energy Resolution

The jet energy resolution (JER) is measured in data and MC using two complementary methods [126]. Both methods are based on an examination of dijet events. The first method, referred to as the "p_T balance technique," requires events with exactly two, nearly back-to-back jets. The p_T asymmetry,

defined by

$$A(p_T^1, p_T^2) = \frac{p_T^1 - p_T^2}{p_T^1 + p_T^2}, \tag{6.2}$$

where p_T^i is the magnitude of the transverse momentum of jet i, is measured. The JER σ_{p_T} is related to the asymmetry resolution σ_A by $\sigma_A = \sigma_{p_T}/\sqrt{2}p_T$. In true dijet events the asymmetry should equal zero, aside from resolution effects. However, the presence of additional jets spoils this. The asymmetry resolution, and thus the jet energy resolution, is measured for a range of transverse momentum thresholds p_T^3 used to veto additional jets. The observed energy resolution is then extrapolated to $p_T^3 \to 0$ to obtain the true JER. A systematic uncertainty of ∼5% for $p_T = 30$ GeV is found in this method from the extrapolation to $p_T^3 = 0$. The $\Delta\phi$ cut applied to the two jets is also varied to obtain an additional systematic of 2-3% for p_T =30-60 GeV.

The second method, referred to as the "bisector method," also makes use of dijet events. The vector sum of the transverse momenta of the jets $\boldsymbol{p}_T = \boldsymbol{p}_T^1 + \boldsymbol{p}_T^2$ is decomposed into two orthogonal directions in the transverse plane, ψ and ϕ', where the direction of ϕ' is chosen to bisect $\Delta\phi_{12} = \phi_1 - \phi_2$. It can be shown that the JER is given by

$$\frac{\sigma_{p_T}}{p_T} = \frac{\sqrt{\sigma_\psi^2 - \sigma_{\phi'}^2}}{\sqrt{2}p_T\sqrt{|\cos\Delta\phi_{12}|}}, \tag{6.3}$$

where σ_ψ ($\sigma_{\phi'}$) is the measured rms of the ψ (ϕ') component of the $\mathbf{p_T}$ vector. A systematic uncertainty arises from the choice of transverse momentum threshold p_T^3 applied to reject additional jets. This is assessed by varying the threshold, and amounts to 3-4%.

The two methods described above yield consistent results. The JER measured in data and MC agree within systematic uncertainties, with a 2-3% discrepancy up to $p_T = 0.5$ TeV. The overall systematic uncertainty is ∼8% (∼4%) for $p_T = 30$ (60) GeV.

The impact of the JER uncertainty on the analysis is assessed by repeating the analysis with a jet energy smearing applied in MC. The jet energy is multiplied by a correction factor sampled from a Gaussian distribution with a mean of 1, and a standard deviation equal to the 1σ uncertainty on the JER measurement. These variations are also propagated to the $\not\!\!E_T$ calculation. The LLR distribution is derived from these systematically varied events, using the nominal probability distribution functions to evaluate the signal and background likelihoods, as described in Equations 5.11 and 5.12. The effect on the second leading jet p_T, jet multiplicity, LQ m_T, and LLR distributions for the total background is shown in Figure 6.5. The ΔLLR caused by the

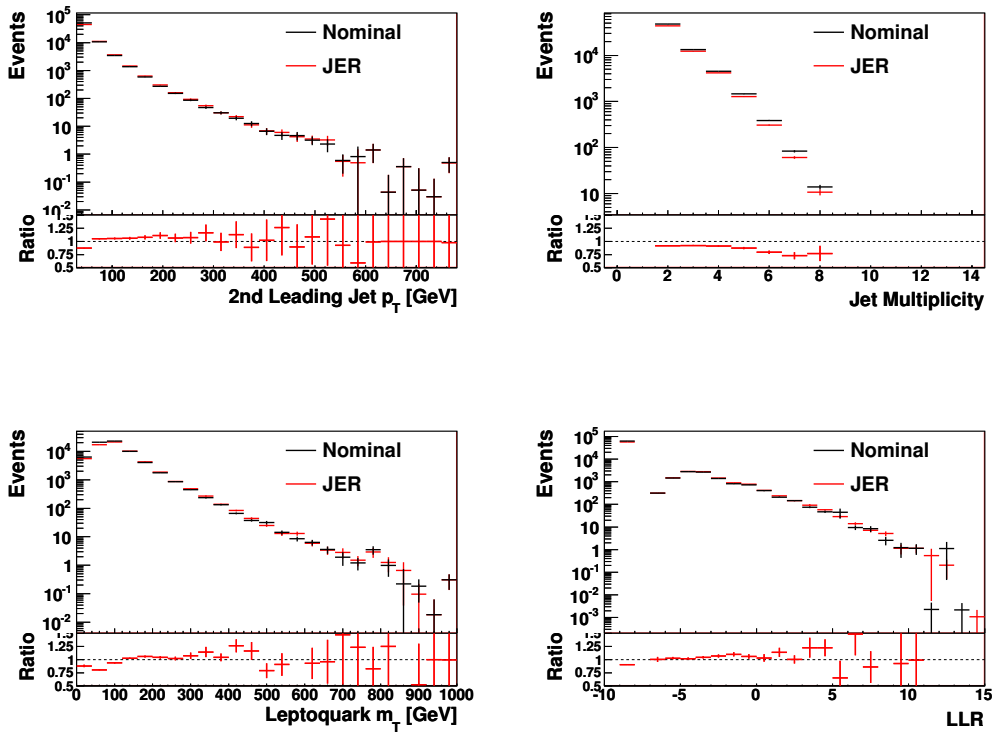

Figure 6.5: The second leading jet p_T, jet multiplicity, LQ m_T, and LLR distributions for the total background. The LLR distribution assumes $m_{LQ} =$ 600 GeV. The nominal distributions are shown in black, and the distributions with a $+1\sigma$ change in the JER are shown in red. The lower plots show the ratio of the systematically varied and nominal distributions.

JER systematic for signal and background sources is shown in Table 6.1.

6.3 Background Modeling Systematic Uncertainties

The generation of MC samples involves a number of choices regarding PDF, ME generator, showering, hadronization, etc. For each background, these choices are made based on current knowledge to achieve optimal modeling. However, there are often a number of other potential choices which are equally as reasonable. In this case, these other reasonable choices are used to assess a systematic uncertainty related to background modeling.

6.3.1 $t\bar{t}$

Several uncertainties must be considered related to the modeling of the $t\bar{t}$ background. These uncertainties are assessed by repeating the analysis using a MC produced with alternative simulation chains. The nominal $t\bar{t}$ samples are produced using the CTEQ6.6 PDF with MC@NLO for event generation and HERWIG for parton showering, hadronization, and UE modeling. Additional samples are produced using a modified LO MRST PDF, AcerMC or POWHEG for ME generation, PYTHIA or POWHEG for showering simulation, and PYTHIA for hadronization. The samples produced using AcerMC are also simulated with more/less radiation from the initial and final state partons than expected, in order to assess uncertainty related to initial and final state radiation (ISR and FSR). This was accomplished by varying several PYTHIA parameters. Finally, two samples are generated with the top mass varied by ± 2.5 GeV to account for uncertainty related to the top mass. In total, there are six alternative MC samples used to assess $t\bar{t}$ modeling uncertainty, which are summarized in table 6.3.

Name	PDF	ME	Showering and Hadronization	UE
Nominal	CTEQ6.6	MC@NLO	HERWIG	JIMMY
POWHEG-JIMMY	MRST2007	POWHEG	HERWIG	JIMMY
POWHEG-PYTHIA	MRST2007	POWHEG	PYTHIA	
ISR/FSR $\pm$	MRST2007	AcerMC	PYTHIA	
Top Mass $\pm$	CTEQ6.6	MC@NLO	HERWIG	JIMMY

Table 6.3: The nominal and systematic $t\bar{t}$ MC samples. Variations on the nominal simulation chain are used to assess systematic uncertainty related to $t\bar{t}$ modeling.

The analysis is repeated with these six alternative $t\bar{t}$ samples. Each time,

the nominal V+jets SF is kept, but the $t\bar{t}$ SF is recalculated. The LLR distribution is derived from these alternative MC samples, using the nominal probability distribution functions to evaluate the signal and background likelihoods, as described in Equations 5.11 and 5.12. The effect on the jet multiplicity, S_T, leading jet p_T and LLR distributions for the total background is shown in Figure 6.6. The ΔLLR values associated with the $t\bar{t}$ modeling systematics are shown in Table 6.1. An additional 2.6% systematic is included to account for uncertainty related to the $t\bar{t}$ normalization, which is chosen based on the deviation of the nominal $t\bar{t}$ SF from unity, shown in Table 5.7. This is listed in Table 6.1 as "Data Normalization."

6.3.2 V+jets

The nominal V+jets samples are produced using the CTEQ6L1 PDF with ALPGEN for ME generation and HERWIG for parton showering, hadronization, and UE modeling. An alternative sample is produced using the CTEQ6.6 PDF with SHERPA for ME generation, parton showering, hadronization, and UE modeling. The analysis is repeated using the SHERPA sample, keeping the nominal $t\bar{t}$ SF but recalculating the V+jets SF. The LLR distribution is derived from this alternative MC samples, using the nominal probability distribution functions to evaluate the signal and background likelihoods, as described in Equations 5.11 and 5.12. The effect on the electron E_T, $\not\!\!E_T$, m_T, and LLR distributions for the total background is shown in Figure 6.7. The ΔLLR caused by the V+jets modeling systematic is shown in Table 6.1. An additional 10% systematic is included to account for uncertainty related to the V+jets normalization, which is chosen based on the deviation of the nominal V+jets SF from unity, shown in Table 5.7. This is listed in Table 6.1 as "Data Normalization."

6.3.3 QCD

As discussed in Section 5.5.2, two alternative methods were utilized to determine the QCD normalization. The average of the two methods was used to determine the QCD normalization central value, separately for selected events and each of the three control regions. Half the difference between the normalizations from the two methods was used to determine the systematic uncertainty in the normalization. To be conservative, the $t\bar{t}$ control region was used to determine the systematic, because it showed the largest discrepancy between the two methods among all of the control regions and the selected events. The LLR distribution for the total background with the QCD normalization varied by $\pm 20\%$ is shown in Figure 6.8.

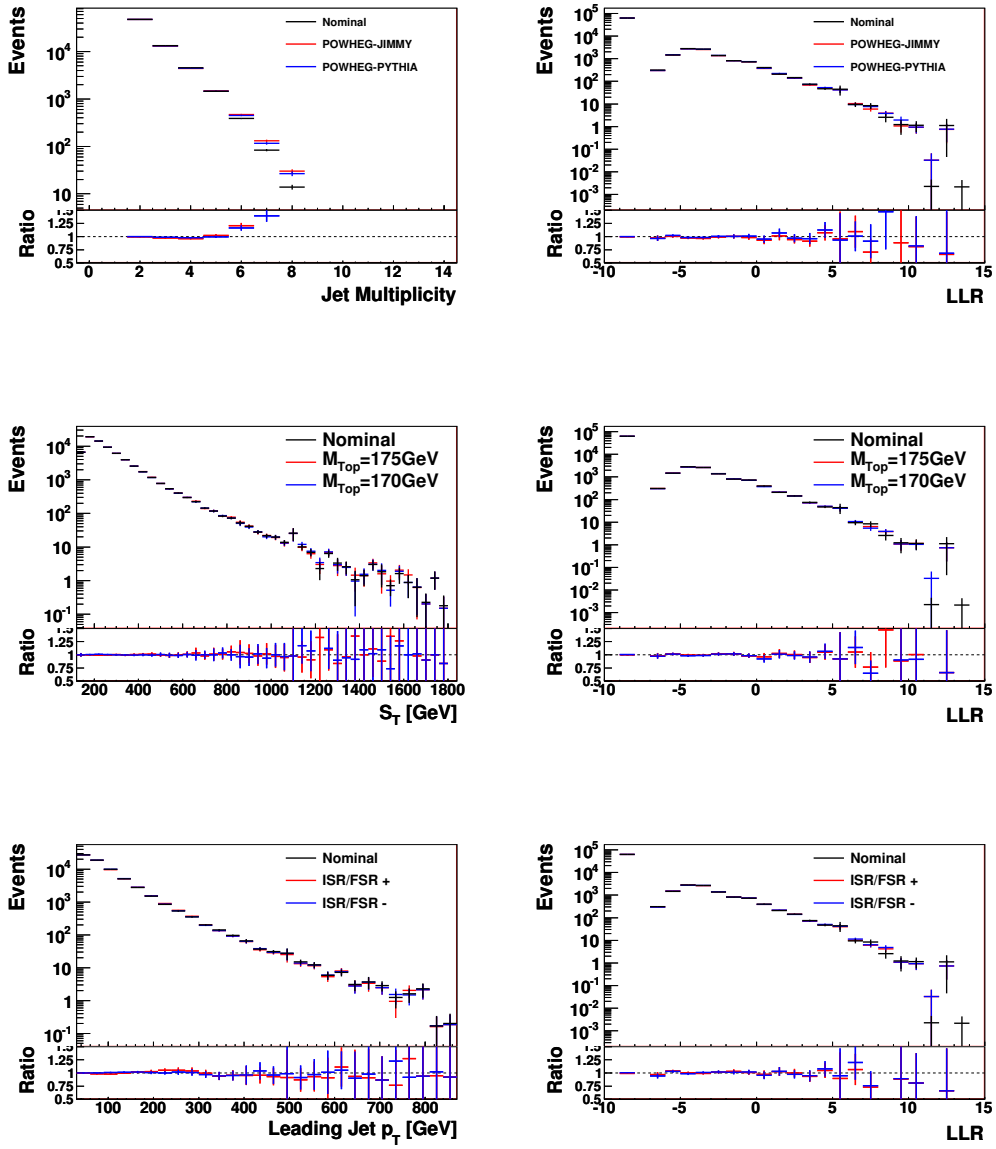

Figure 6.6: The jet multiplicity and LLR distributions using various event simulation packages (top), the S_T and LLR distributions for various values of the top quark mass (middle), and the leading jet p_T and LLR distributions with the amount of ISR/FSR varied (bottom). The LLR distributions assume $m_{LQ} = 600$ GeV. The nominal distributions are shown in black, and the systematic distributions are shown in red and blue. The lower plots show the ratio of the systematically varied and nominal distributions.

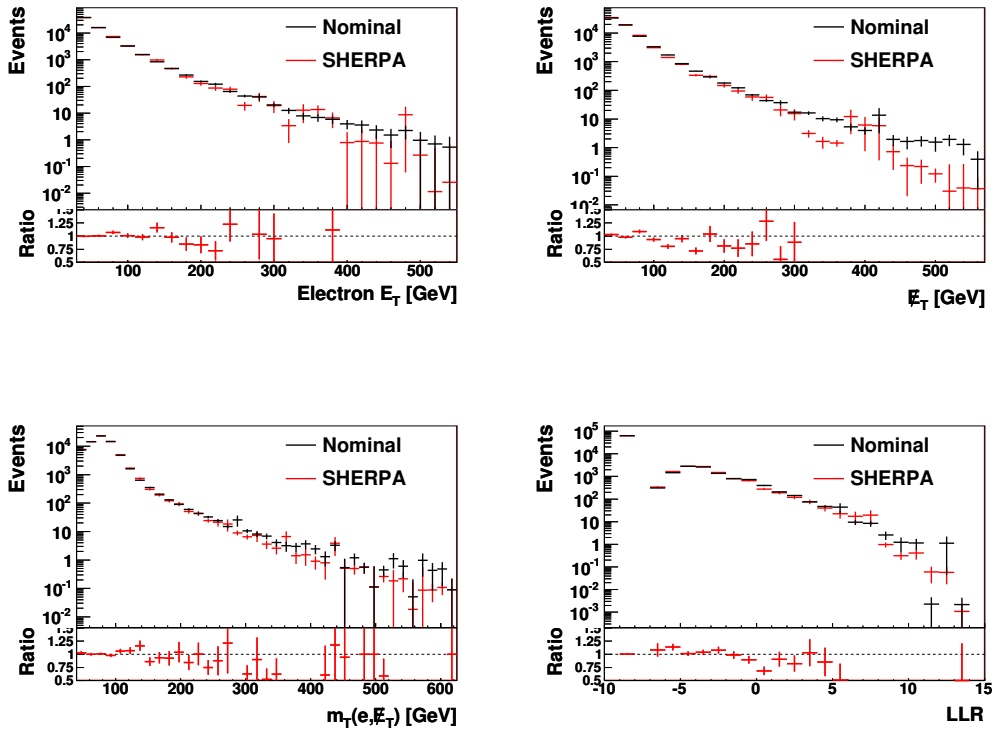

Figure 6.7: The electron E_T, $\not{E}_T$, m_T, and LLR distributions for the total background. The LLR distribution assumes $m_{LQ} = 600$ GeV. The nominal distributions are shown in black, and the distributions derived from the SHERPA sample are shown in red. The lower plots show the ratio of the systematically varied and nominal distributions.

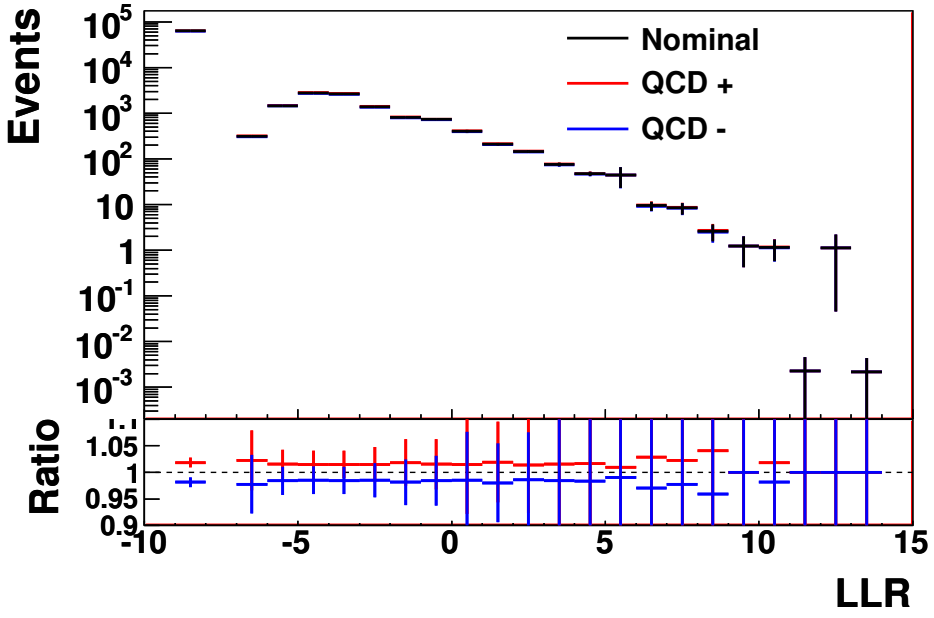

Figure 6.8: The LLR distribution for the total background, assuming $m_{LQ} = 600$ GeV. The nominal distribution is shown in black, and the distribution with a $+1\sigma$ (-1σ) change in the QCD normalization is shown in red (blue). The lower plot shows the ratio of the systematically varied and nominal distributions.

6.4 Parton Distribution Function Systematic Uncertainty

The choice of PDF has a significant impact on the event kinematics and cross section of the LQ signal. This systematic uncertainty is assessed by deriving the LLR distribution using selected events reweighted as if produced using the modified LO MRST2007 PDF, as opposed to the nominal LO CTEQ6L1 PDF. The effect on the signal LLR distribution is shown in Figure 6.9. The ΔLLR caused by the signal PDF systematic is shown in Table 6.1.

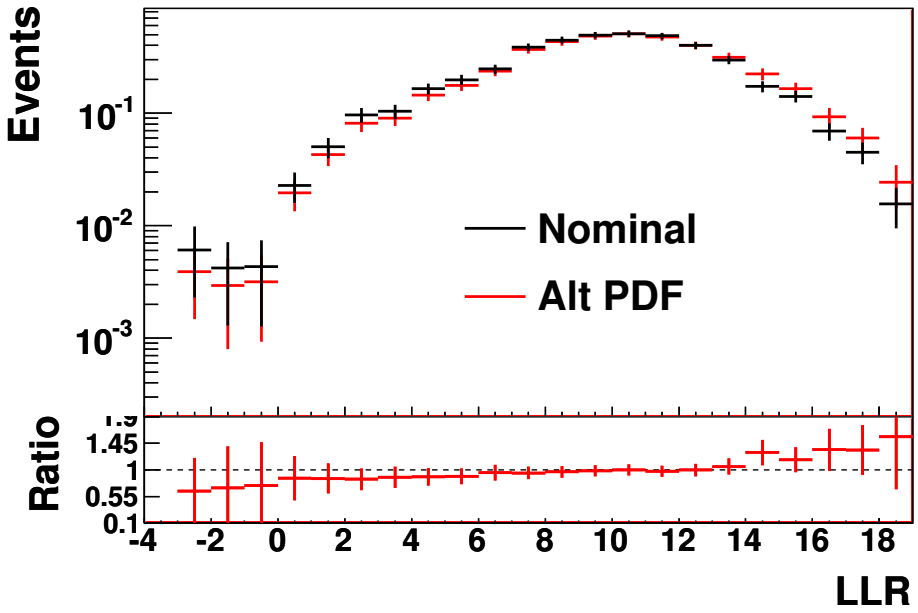

Figure 6.9: The LLR distribution for the signal, assuming $m_{LQ} = 600$ GeV. The nominal distribution is shown in black, and the distribution produced using an alternative PDF for signal modeling is shown in red. The lower plot shows the ratio of the systematically varied and nominal distribution.

6.5 Log-Likelihood Ratio Probability Distribution Functions

The finite statistics of signal and background MC samples leads to a systematic uncertainty. Based on the nominal LLR probability distribution functions for signal and background, an ensemble of alternate probability distribution functions is generated where the bin-by-bin contents is varied according to a Gaussian distribution with mean (standard deviation) taken as the nominal bin content (uncertainty). From this ensemble of probability distribution functions, an ensemble of LLR distributions is generated. The bin-by-bin mean of this ensemble is used to derive a systematically varied LLR distribution, whose bin-by-bin uncertainty is taken from the ensemble RMS. The ΔLLR associated with this systematic uncertainty is shown in Table 6.1 for signal and background sources.

6.6 Luminosity Systematic Uncertainty

The single top and diboson background normalizations are the only backgrounds whose normalization is not taken from data. Therefore, the standard ATLAS luminosity uncertainty of 3.7% is applied to these backgrounds [76]. The same uncertainty is applied to signal, as shown in Table 6.1.

Chapter 7

Limit Setting

In general, the results of a search for BSM physics can have two outcomes; either the signal is observed, or it is not. If no significant evidence is found in the data for the presence of the signal, then the results of the search are typically used to constrain one or more parameters of a model. This chapter begins with a description of a simple example of limit setting, a so-called "counting experiment." This example is then generalized to include the effect of systematic uncertainties and to take advantage of the additional information contained in a binned discriminant.

7.1 Counting Experiment

Counting experiments represent the simplest example of limit setting in high-energy physics [127]. Suppose a new physics process has been proposed which leads to enhanced production of event topology **T** with respect to background processes alone. In order to confirm or rule out the presence of the proposed process, two hypotheses must be tested against the data. The background-only hypothesis assumes there is no new physics, so $N^b = \sigma^b \times \varepsilon^b \times \int L\mathrm{d}t$ events are expected, where σ^b (ε^b) is the production cross section (selection efficiency) for background events with topology **T** and $\int L\mathrm{d}t$ is the integrated luminosity collected during the course of data taking. The signal+background hypothesis assumes the presence of the new process, so $N^s = \sigma^s \times \varepsilon^s \times \int L\mathrm{d}t$ additional events are expected with respect to the background prediction N^b, where σ^s (ε^s) is the production cross section (selection efficiency) for signal events with topology **T**.

To test these hypotheses against the data, a test statistic which discriminates between signal-like and background-like outcomes is defined. The opti-

mal test statistic is the likelihood ratio [128, 129], defined by

$$\Lambda(N^d) = \frac{L(N^d; N^s + N^b)}{L(N^d; N^b)}, \tag{7.1}$$

where N^d is the number of events observed in data and $L(x; y)$ is the Poisson probability distribution with a mean of y evaluated at x. For convenience, -2 times the ln of the likelihood ratio is used instead,

$$Q(N^d) = -2 \ln \Lambda(N^d). \tag{7.2}$$

A series of pseudo-experiments are performed to determine the probability distribution function of this test statistic for the background-only and signal+background hypotheses. In each pseudo-experiment, the number of observed pseudo-data events is sampled randomly from a Poisson distribution with mean N^b ($N^s + N^b$) for background-only (signal+background) hypothesis pseudo-experiments. Using the obtained value as N^d, the test statistic is evaluated using Equation 7.2. Example probability distribution functions are shown in Figure 7.1, assuming $N^s = 13$, $N^b = 20$, and $N^d = 22$.

The value of the test statistic observed in actual data $Q_{observed}$ is then compared to the calculated probability distribution functions to assess the degree of compatibility of the data with the background-only and signal+background hypotheses. Confidence levels (CL) are defined in terms of integrals of the probability distribution functions:

$$CL_b = \int_{Q_{observed}}^{\infty} P_b(Q(N^d))\mathrm{d}(Q(N^d)) \tag{7.3}$$

$$CL_{s+b} = \int_{Q_{observed}}^{\infty} P_{s+b}(Q(N^d))\mathrm{d}(Q(N^d)). \tag{7.4}$$

These confidence levels specify the probability to obtain an outcome more background-like than the one actually observed in the data, under the background-only and signal+background hypotheses. In this simple case, the integrals could be evaluated analytically. However, in more complex scenarios, such as described in Section 7.2, they are best evaluated numerically; hence the use of pseudo-experiments. In the case of the observation of an excess over background predictions, CL_b is used to assess the probability that the background would fluctuate upwards enough to account for the observed excess. If this probability is small, then the background-only hypothesis may be excluded.

Alternatively, when no statistically significant excess is observed, then it is useful to know the probability that the signal+background would fluctuate downwards enough to "hide" the presence of the signal. If this probability is small, then the signal+background hypothesis may be excluded. CL_{s+b} is not appropriate for this task, as it leads to a phenomenon known as "spurious exclusion," whereby a model can sometimes be excluded even if the search had no sensitivity to the model in question. The modified-frequentist approach resolves this issue by normalizing CL_{s+b} by CL_b to obtain

$$CL_s = \frac{CL_{s+b}}{CL_b}. \tag{7.5}$$

Using CL_s as opposed to CL_{s+b} gives more conservative and appropriate exclusions. The typical CL required for signal+background hypothesis exclusion is 95%, which corresponds to $1 - CL_s \geq 0.95$. These limits are usually interpreted in terms of some parameter of the signal model, such as σ_s.

The test statistic probability distribution functions can also be used to determine expected limits, assuming no signal will be observed. This is accomplished by taking the mean of the background-only hypothesis probability distribution function, and calculating confidence levels with respect to this value of the test statistic. This is useful for search optimization before examining actual data.

7.2 Inclusion of Systematic Uncertainty

In typical applications, the predictions of signal and background are associated with a number of sources of systematic uncertainty. In the simple example described above, $N^b = \sigma_b \times \varepsilon_b \times \int L\mathrm{d}t$ and $N^s = \sigma_s \times \varepsilon_s \times \int L\mathrm{d}t$ may be subject to uncertainties related to the background and signal cross sections and selection efficiencies, and the integrated luminosity. These are referred to as nuisance parameters. Nuisance parameter uncertainties are incorporated into the limit setting procedure by varying the mean of the Poisson probability distribution function used to determine the number of observed events in each pseudo-experiment. The mean of the Poisson distribution is sampled from a Gaussian distribution whose width is the fractional yield uncertainty. Correlated uncertainties are sampled together, whereas uncorrelated uncertainties are sampled separately. This procedure smears the test statistic probability distribution functions, ultimately reducing the discriminating power. Example probability distribution functions including the effect of systematic uncertainty are shown in Figure 7.2.

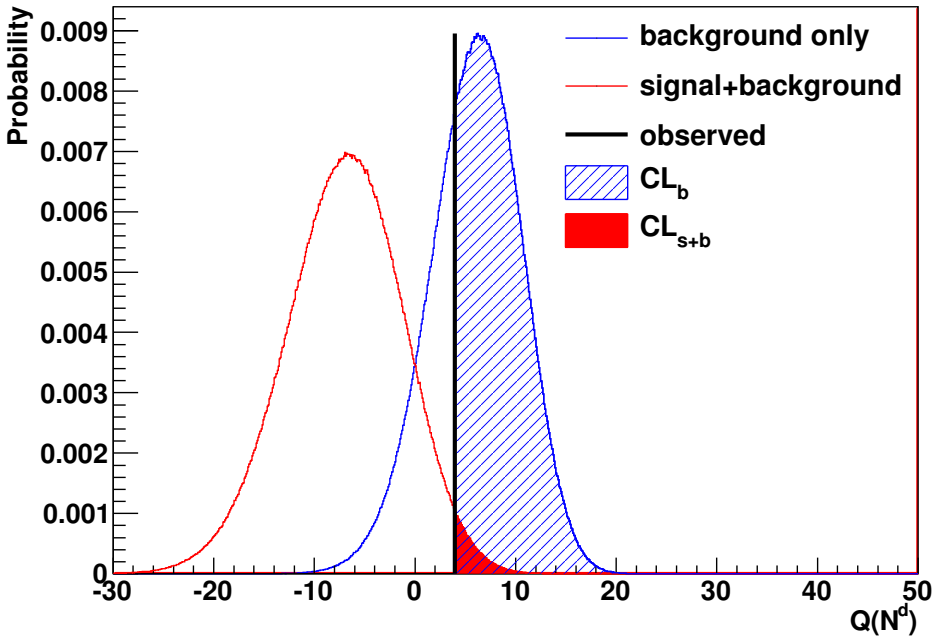

Figure 7.1: Example test statistic probability distribution functions, assuming $N^s = 13$, $N^b = 20$, and $N^d = 22$. The background-only (signal+background) test statistic probability distribution function is represented by the blue (red) histogram, the observed value of the test statistic is shown by the vertical black line, and CL_b (CL_{s+b}) is represented by the blue hatched (solid red) area. The resulting $1 - CL_s$ value is 0.966, which means the signal+background hypothesis is excluded at a 95% confidence level.

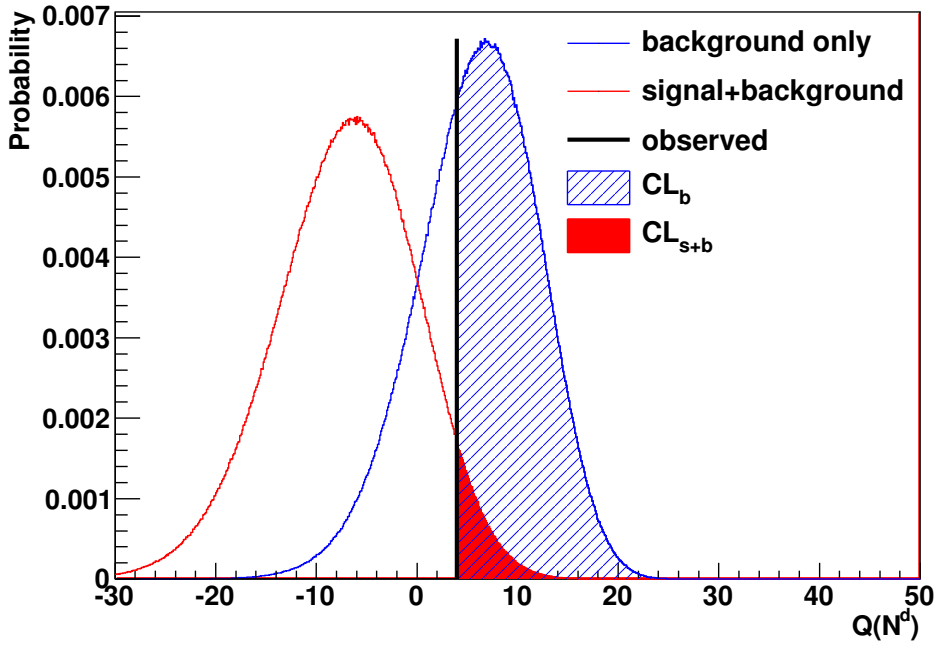

Figure 7.2: Example test statistic probability distribution functions including the effect of systematic uncertainty, assuming $N^s = 13$, $N^b = 20$, and $N^d = 22$. The signal (background) yield is assumed to have a 10% (5%) fractional uncertainty. The background-only (signal+background) test statistic probability distribution function is represented by the blue (red) histogram, the observed value of the test statistic is shown by the vertical black line, and CL_b (CL_{s+b}) is represented by the blue hatched (solid red) area. The resulting $1 - CL_s$ value is 0.921, which means the signal+background hypothesis is not excluded at a 95% confidence level, in contrast with the previous example where the systematic uncertainties were neglected.

7.3 Generalization

Better discrimination between the background-only and signal+background hypotheses can be achieved if a binned discriminant is used rather than simple event counting. The discriminant may be an invariant mass distribution or some other quantity that reflects the characteristics of the hypothetical signal. In this case, the generalization from a simple counting experiment is simple. Each bin of the discriminating distribution is treated as an independent counting experiment. The test statistic Q_i is evaluated separately for each bin, and the product of these individual test statistics gives the overall test statistic, so that

$$Q(\{N_i^d\}) = \prod_{bins} Q_i(N_i^d). \tag{7.6}$$

Multiple independent search channels may be easily combined as well. In this case, the test statistic includes a product over each channel as well, so that

$$Q(\{N_{i,j}^d\}) = \prod_{channels} \prod_{bins} Q_{i,j}(N_{i,j}^d). \tag{7.7}$$

The probability distribution function is then determined and the derivation of the confidence levels proceeds as described above. In this analysis, a software package known as COLLIE [130, 131] is used to perform the procedure described above and determine exclusion limits based on the observed and predicted LLR distributions.

Chapter 8

Results

In this chapter, results are presented for the analysis described in Chapter 5. In addition, results are presented for a similar analysis in the $eejj$ final state. Finally, these two analyses are combined, and the results presented.

8.1 $e\not{E}_T jj$ Channel

The observed event yields for a signal enhanced region with $LLR > 0$ are shown in Table 8.1 for the 400 GeV and 600 GeV LQ mass hypotheses. For these and all other LQ mass hypotheses considered, no statistically significant excess of events over the SM backgrounds is observed. Thus, the nominal and systematically varied LLR distributions, described in Chapters 5 and 6 respectively, are used to derive a 95% CL upper bound on the allowed LQ cross section $\sigma(pp \to LQ\overline{LQ})$ using the modified frequentist approach described in Chapter 7. The expected and observed limits assuming $\beta = 0.5$ are shown in Figure 8.1 as a function of m_{LQ}.

The cross section for scalar LQ pair production depends only on m_{LQ}. Thus, LQ masses for which the cross section would exceed the observed 95% CL upper bound may be excluded. The expected (observed) LQ mass lower bound is $m_{LQ} > 542$ (558) GeV, assuming $\beta = 0.5$. The m_{LQ} lower bound for the full range of β values is shown in Figure 8.2.

8.2 $eejj$ Channel

An orthogonal analysis was performed in the $eejj$ final state [132], typical of events where both leptoquarks decay to eq. The observed event yields for a signal enhanced region with $LLR > 0$ are shown in Table 8.2 for the 400 GeV and 600 GeV LQ mass hypotheses. Again, for these and all other LQ mass

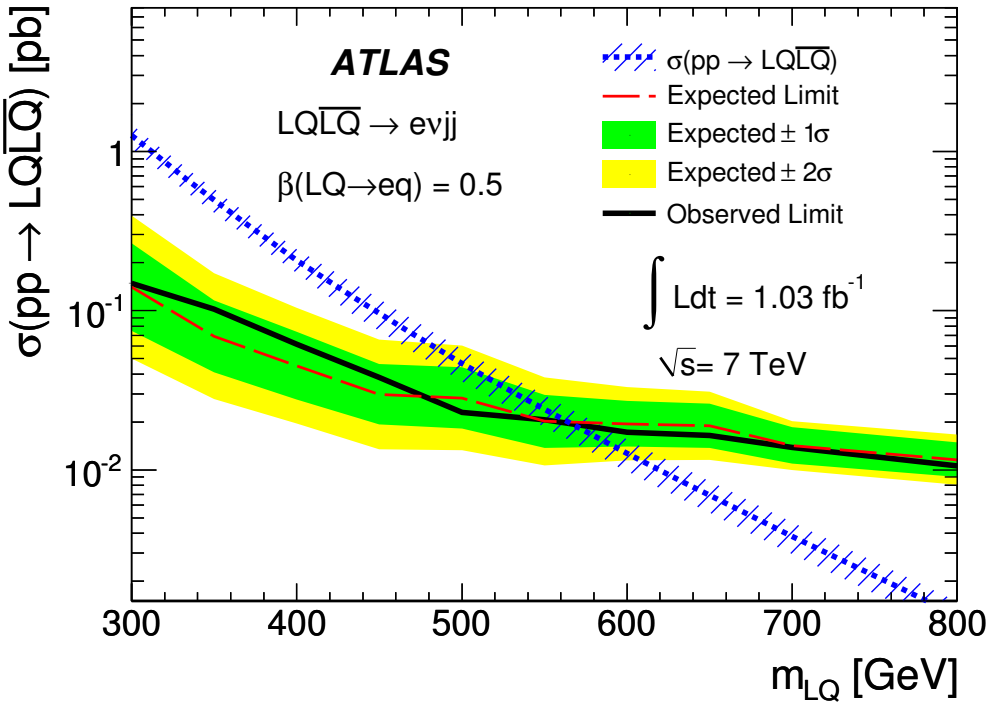

Figure 8.1: The 95% CL upper bound on $\sigma(pp \to LQ\overline{LQ})$, assuming $\beta = 0.5$, for the $e\not{E}_T jj$ channel. The expected (observed) exclusion limit is shown by the dashed red (solid black) line and the $\pm 1(2)\sigma$ uncertainty on the expected exclusion is shown by the green (yellow) band. The LQ pair production cross section is shown by the dotted blue line, with the associated uncertainty due to the choice of PDF and factorization/renormalization scales.

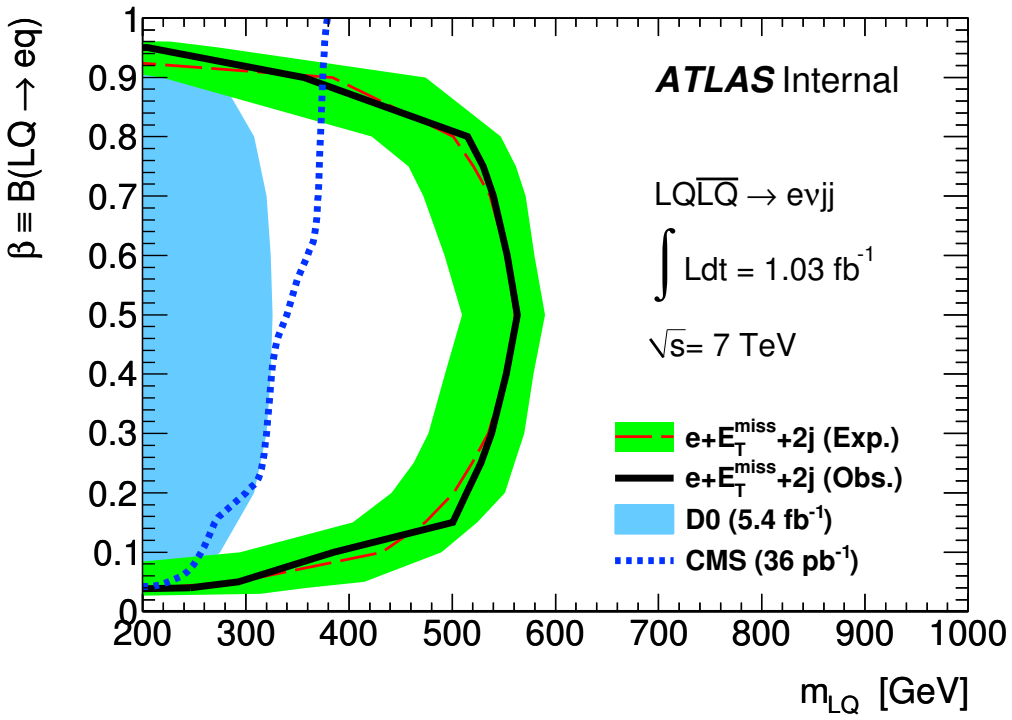

Figure 8.2: The 95% CL lower bound on the allowed LQ mass in the β vs. m_{LQ} plane for the $e\not{E}_T jj$ channel. The expected (observed) exclusion limit is shown by the dashed red (solid black) line and the $\pm 1\sigma$ error band on the expected exclusion is shown in green. The previously observed exclusion limit from DØ (CMS) is shown by the shaded blue area (dotted blue line).

	m_{LQ}	
Source	400 GeV	600 GeV
W+jets	1500 ± 670	670 ± 210
Z+jets	45 ± 41	18 ± 19
$t\bar{t}$	430 ± 180	150 ± 38
Single Top	53 ± 19	23 ± 4
Diboson	25 ± 11	11 ± 2
QCD	170 ± 35	75 ± 15
Total Background	2200 ± 690	950 ± 220
Data	2207	900
LQ	69 ± 4	4.5 ± 0.2

Table 8.1: Event yields in a signal enhanced region with $LLR > 0$ for the $e\not{E}_T jj$ channel, for the 400 GeV and 600 GeV LQ mass hypotheses. The data and background predictions agree within uncertainties; no excess of events is observed.

hypotheses considered, no systematically significant excess of events over SM backgrounds is observed. The expected and observed 95% CL $\sigma(pp \to LQ\overline{LQ})$ upper bounds are shown in Figure 8.3, assuming $\beta = 1.0$. The expected (observed) LQ mass lower bound is $m_{LQ} > 649$ (661) GeV. The m_{LQ} lower bound for the full range of β values is shown in Figure 8.4.

8.3 Combination of the $e\not{E}_T jj$ and $eejj$ Channels

The two channels are combined using the methodology described in Section 7.3 to obtain stronger m_{LQ} exclusions for a wide β range. For small values of β, the $eejj$ channel has marginal sensitivity, and its inclusion does not significantly affect the result obtained by the $e\not{E}_T jj$ channel alone. For large values of β, the $e\not{E}_T jj$ channel has marginal sensitivity, and its inclusion does not significantly affect the result obtained by the $eejj$ channel alone. The combined 95% CL $\sigma(pp \to LQ\overline{LQ})$ exclusion is shown in Figure 8.5, assuming $\beta = 0.5$. The m_{LQ} lower bound for the full range of β values is shown in Figure 8.6. The expected (observed) LQ mass lower bound is $m_{LQ} > 587$ (607) GeV, assuming $\beta = 0.5$.

The expected and observed LQ lower mass bounds are summarized in Table 8.3. These bounds are significantly stronger than those obtained by previ-

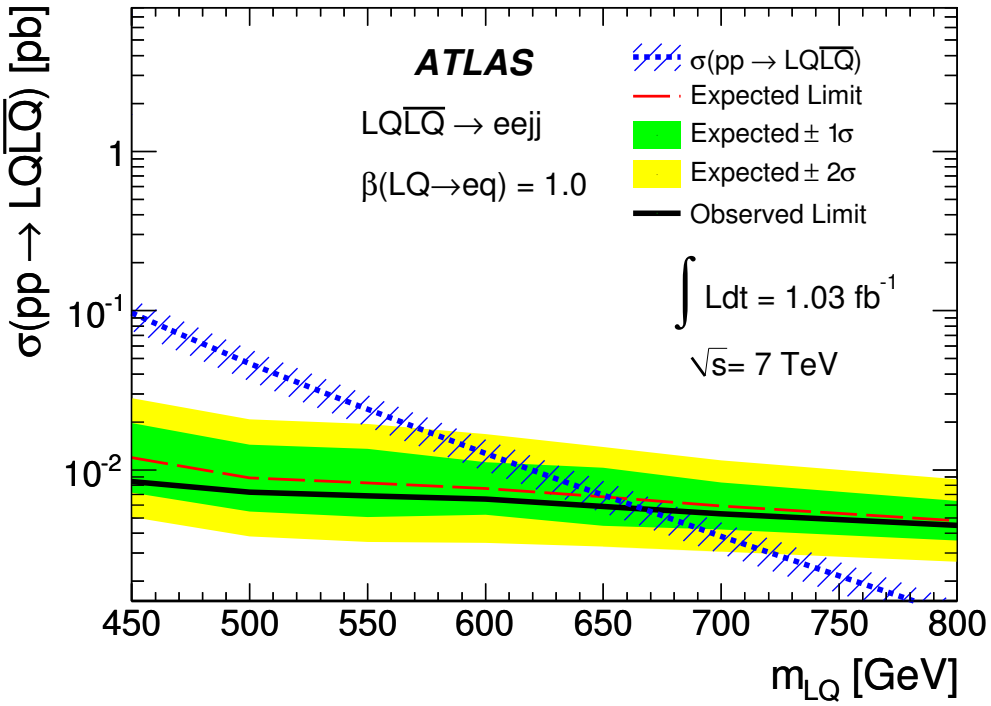

Figure 8.3: The 95% CL upper bound on $\sigma(pp \to LQ\overline{LQ})$ for the $eejj$ channel, assuming $\beta = 1.0$. The expected (observed) exclusion limit is shown by the dashed red (solid black) line and the $\pm 1(2)\sigma$ uncertainty on the expected exclusion is shown by the green (yellow) band. The LQ pair production cross section is shown by the dotted blue line, with the associated uncertainty due to the choice of PDF and factorization/renormalization scales.

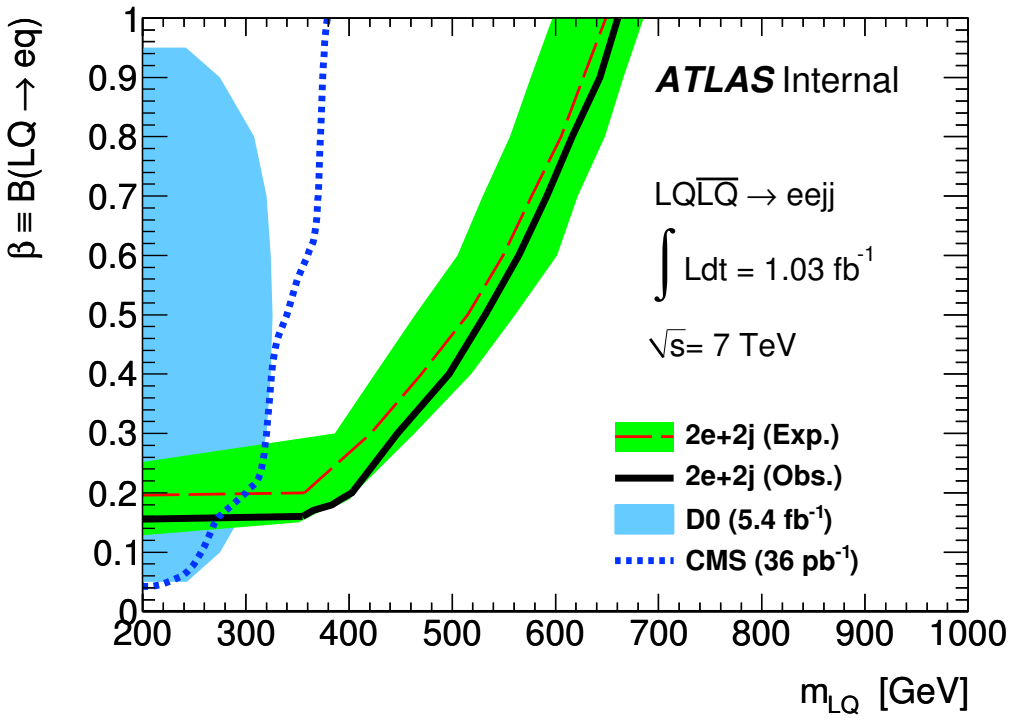

Figure 8.4: The 95% CL lower bound on the allowed LQ mass in the β vs. m_{LQ} plane, for the $eejj$ channel. The expected (observed) exclusion limit is shown by the dashed red (solid black) line and the $\pm 1\sigma$ error band on the expected exclusion is shown in green. The previously observed exclusion limit from DØ (CMS) is shown by the shaded blue area (dotted blue line).

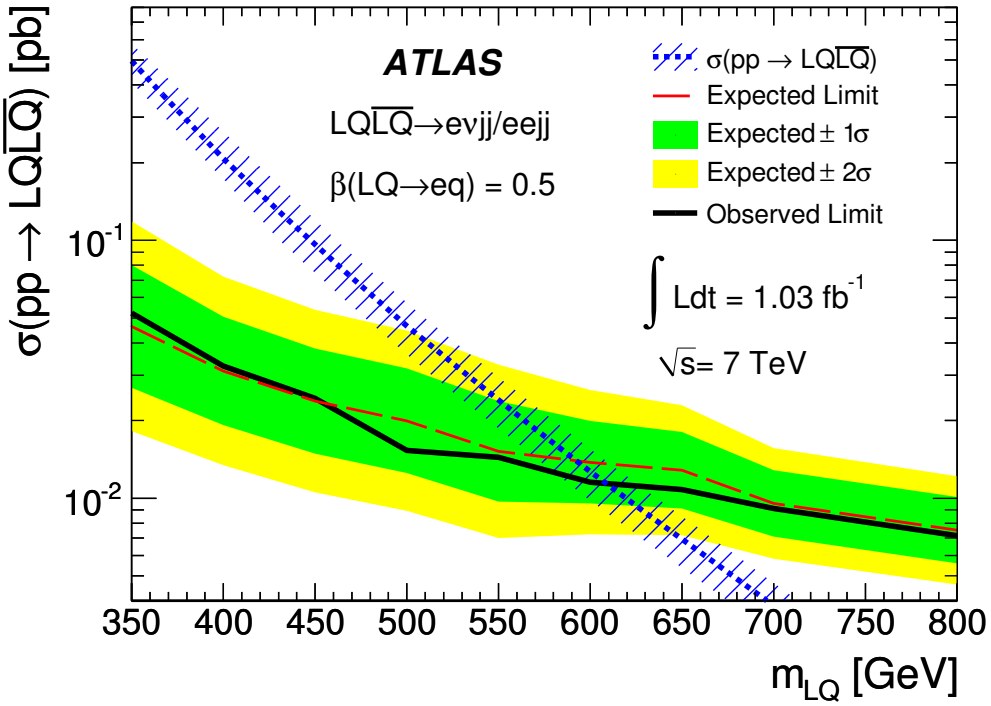

Figure 8.5: The 95% CL upper bound on $\sigma(pp \to LQ\overline{LQ})$ for the combination of the $e\not{E}_T jj$ and $eejj$ channels, assuming $\beta = 0.5$. The expected (observed) exclusion limit is shown by the dashed red (solid black) line and the $\pm 1(2)\sigma$ uncertainty on the expected exclusion is shown by the green (yellow) band. The LQ pair production cross section is shown by the dotted blue line, with the associated uncertainty due to the choice of PDF and factorization/renormalization scales.

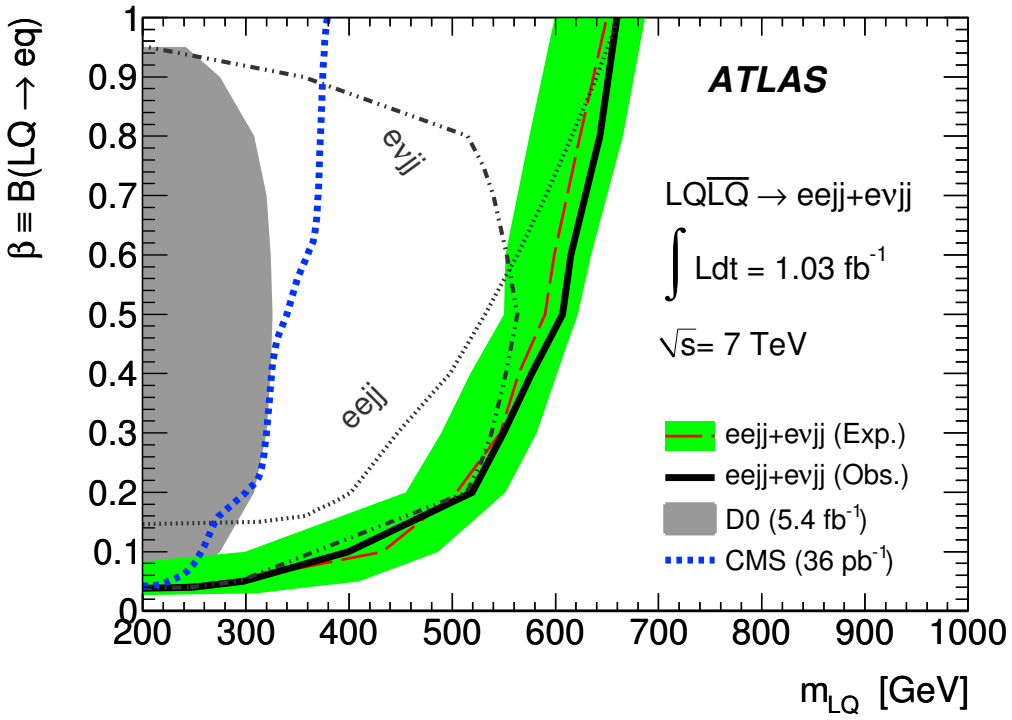

Figure 8.6: The 95% CL lower bound on the allowed LQ mass in the β vs. m_{LQ} plane, for the combination of the $e\not{E}_T jj$ and $eejj$ channels. The individual exclusions for the $e\not{E}_T jj$ and $eejj$ channels are shown as dot-dashed and dashed lines respectively. The expected (observed) combined exclusion limit is shown by the dashed red (solid black) line and the $\pm 1\sigma$ error band on the expected exclusion is shown in green. The previously observed exclusion limit from DØ (CMS) is shown by the shaded grey area (dotted blue line).

Source	m_{LQ} 400 GeV	600 GeV
Z+jets	98 ± 53	26 ± 14
$t\bar{t}$	15 ± 9	4.6 ± 2.2
Single Top	1.4 ± 0.9	0.7 ± 0.4
Diboson	1.5 ± 0.8	0.7 ± 0.3
QCD	9.2 ± 4.5	2.3 ± 1.5
Total Background	120 ± 55	34 ± 14
Data	82	22
LQ	120 ± 8	7.5 ± 0.5

Table 8.2: Event yields for the $eejj$ channel in a signal enhanced region with $LLR > 0$, for the 400 GeV and 600 GeV LQ mass hypotheses. The data and background predictions agree within uncertainties; no excess of events is observed.

ous direct searches at the LHC, Tevatron, and elsewhere.

	Channel	$e\not{E}_T jj$	$e\not{E}_T jj + eejj$	
	β	0.5	0.5	1.0
95% CL	Expected	542	587	650
Limit [GeV]	Observed	558	607	660

Table 8.3: The expected and observed mass limits for the $e\not{E}_T jj$ channel at $\beta = 0.5$, and the combination of the $e\not{E}_T jj$ and $eejj$ channels at $\beta = 0.5$ and 1.0.

Chapter 9

Conclusions

The SM, although remarkably successful at describing observations over a broad energy range, is an incomplete theory of nature. It is well known that a new theory is needed to describe phenomena at high energy. Many extensions of the SM have been proposed, of which a number hypothesize the existence of leptoquarks, color-triplet gauge bosons which carry both lepton and baryon number.

The LHC is a particle accelerator capable of producing highly energetic pp collisions. If leptoquarks do exist, and their mass is sufficiently small, they would be produced copiously in these collisions. In order to observe the production of leptoquarks, high-precision measurement of their decay products is necessary. ATLAS is a general purpose particle detector surrounding one of the interaction points at the LHC. It performs position and energy measurements of the particles produced in the collisions. From this series of position and energy measurements, highly sophisticated software is used to reconstruct electrons, muons, jets, $\not\!\!E_T$, etc.

A search for pair production of first generation scalar leptoquarks is performed in pp collisions with a center-of-mass energy of $\sqrt{s} = 7$ TeV, produced at the LHC and reconstructed with the ATLAS detector. The total dataset examined corresponds to $\int L\mathrm{d}t = 1.035 \pm 0.038$ fb^{-1}. Two of the potential decay modes of pair produced leptoquarks are examined, the $e\not\!\!E_T jj$ and $eejj$ final states. SM background predictions are derived using MC and data-driven techniques. The accuracy of SM background modeling is verified in dedicated background control regions. Event selection criteria are derived from considerations of the signal kinematics. A signal region is defined using a multivariate log-likelihood ratio (LLR) discriminant.

The observed event yields agrees with the expectation from SM background processes alone. No statistically significant excess is observed in the signal enhanced region with large LLR. 95% CL cross section upper bounds for LQ

pair production are derived using a modified frequentist approach, treating the systematic uncertainties as nuisance parameters. From these cross section limits, 95% CL lower bounds on the potential LQ mass are derived. A LQ mass $m_{LQ} < 607$ (660) GeV is excluded, assuming $\beta \equiv BR(LQ \to eq) = 0.5$ (1.0). These are the most stringent LQ mass bounds ever obtained from a direct search.

Bibliography

[1] K. J. Barnes, "Group theory for the standard model of particle physics and beyond," 2010.

[2] C. P. Burgess and G. Moore, "The Standard Model: A Primer," Cambridge University Press, 2007.

[3] S. Weinberg, "A Model of Leptons," *Phys. Rev. Lett.* **19** (1967) 1264–1266.

[4] A. Salam, "Weak and Electromagnetic Interactions," *Conf.Proc.* **C680519** (1968) 367–377.

[5] S. Dawson, "Introduction to electroweak symmetry breaking," `arXiv:hep-ph/9901280`.

[6] Particle Data Group, "Review of particle physics," *J.Phys.G* **G37** (2010) 075021.

[7] M. Maltoni, T. Schwetz, M. Tortola, and J. Valle, "Status of global fits to neutrino oscillations," *New J.Phys.* **6** (2004) 122, `arXiv:hep-ph/0405172`.

[8] T. Blum, T. Doi, M. Hayakawa, T. Izubuchi, and N. Yamada, "Determination of light quark masses from the electromagnetic splitting of pseudoscalar meson masses computed with two flavors of domain wall fermions," *Phys.Rev.* **D76** (2007) 114508, `arXiv:0708.0484`.

[9] MILC Collaboration, "Light pseudoscalar decay constants, quark masses, and low energy constants from three-flavor lattice QCD," *Phys.Rev.* **D70** (2004) 114501, `arXiv:hep-lat/0407028`.

[10] M. Shifman, A. Vainshtein, and V. Zakharov, "QCD and resonance physics. theoretical foundations," *Nuclear Physics B* **147** (1979), no. 5, 385 – 447.

[11] N. Isgur and M. B. Wise, "Weak Decays of Heavy Mesons in the Static Quark Approximation," *Phys.Lett.* **B232** (1989) 113.

[12] M. Kobayashi and T. Maskawa, "CP-Violation in the Renormalizable Theory of Weak Interaction," *Progress of Theoretical Physics* **49** (1973), no. 2, 652–657.

[13] R. Streater and A. Wightman, "PCT, spin and statistics, and all that," 1989.

[14] H. Rothe, "Lattice gauge theories: An Introduction," *World Sci.Lect.Notes Phys.* **74** (2005) 1–605.

[15] D. J. Gross and F. Wilczek, "Ultraviolet Behavior of Non-Abelian Gauge Theories," *Phys. Rev. Lett.* **30** Jun (1973) 1343–1346.

[16] J. D. Hobbs, M. S. Neubauer, and S. Willenbrock, "Tests of the Standard Electroweak Model at the Energy Frontier," *Rev.Mod.Phys.*, 2010 arXiv:1003.5733.

[17] F. Zwicky, "On the Masses of Nebulae and of Clusters of Nebulae," *Astrophys.J.* **86** (1937) 217–246.

[18] K. Garrett and G. Duda, "Dark Matter: A Primer," *Adv.Astron.* **2011** (2011) 968283, arXiv:1006.2483.

[19] G. Bertone, D. Hooper, and J. Silk, "Particle dark matter: evidence, candidates and constraints," *Physics Reports* **405** (2005) 279 – 390.

[20] S. Nussinov, "Solar Neutrinos and Neutrino Mixing," *Phys. Lett.* **B63** (1976) 201–203.

[21] A. Habig, "MINOS neutrino oscillation results," *Mod.Phys.Lett.* **A25** (2010) 1219–1231, arXiv:1004.2647.

[22] A. Hocker and Z. Ligeti, "CP violation and the CKM matrix," *Ann.Rev.Nucl.Part.Sci.* **56** (2006) 501–567, arXiv:hep-ph/0605217.

[23] Muon g-2 Collaboration, "Measurement of the negative muon anomalous magnetic moment to 0.7 ppm," *Phys.Rev.Lett.* **92** (2004) 161802, arXiv:hep-ex/0401008.

[24] K. Hagiwara, A. Martin, D. Nomura, and T. Teubner, "Improved predictions for g-2 of the muon and alpha(QED) (M**2(Z))," *Phys.Lett.* **B649** (2007) 173–179, arXiv:hep-ph/0611102.

[25] "Combination of Higgs Boson Searches with up to 4.9 fb-1 of pp Collisions Data Taken at a center-of-mass energy of 7 TeV with the ATLAS Experiment at the LHC," Tech. Rep. ATLAS-CONF-2011-163, CERN, Geneva, Dec 2011.

[26] C. Collaboration, "Combined results of searches for the standard model Higgs boson in pp collisions at sqrt(s) = 7 TeV," arXiv:1202.1488.

[27] D0 Collaboration, "Forward-backward asymmetry in top quark-antiquark production," *Phys.Rev.* **D84** (2011) 112005, arXiv:1107.4995.

[28] CDF Collaboration, "Evidence for a Mass Dependent Forward-Backward Asymmetry in Top Quark Pair Production," *Phys.Rev.* **D83** (2011) 112003, arXiv:1101.0034, 23 pages, 18 figures, submitted to Physical Review D.

[29] J. F. Gunion, "New (and Old) Perspectives on Higgs Physics," *AIP Conf.Proc.* **1030** (2008) 94–103, arXiv:0804.4460.

[30] Y. Golfand and E. Likhtman, "Extension of the Algebra of Poincare Group Generators and Violation of p Invariance," *JETP Lett.* **13** (1971) 323–326.

[31] D. Volkov and V. Akulov, "Is the Neutrino a Goldstone Particle?," *Phys.Lett.* **B46** (1973) 109–110.

[32] J. Wess and B. Zumino, "Supergauge Transformations in Four-Dimensions," *Nucl.Phys.* **B70** (1974) 39–50.

[33] J. Wess and B. Zumino, "Supergauge Invariant Extension of Quantum Electrodynamics," *Nucl.Phys.* **B78** (1974) 1.

[34] J.-L. Gervais and B. Sakita, "Generalizations of dual models," *Nucl.Phys.* **B344** (1971) 477–492.

[35] J. C. Pati and A. Salam, "Lepton Number as the Fourth Color," *Phys.Rev.* **D10** (1974) 275–289.

[36] H. Georgi and S. Glashow, "Unity of All Elementary Particle Forces," *Phys.Rev.Lett.* **32** (1974) 438–441.

[37] H. Harari, "A Schematic Model of Quarks and Leptons," *Phys.Lett.* **B86** (1979) 83.

[38] C. T. Hill and E. H. Simmons, "Strong dynamics and electroweak symmetry breaking," *Phys.Rept.* **381** (2003) 235–402, arXiv:hep-ph/0203079.

[39] A. Belyaev, C. Leroy, R. Mehdiyev, and A. Pukhov, "Leptoquark single and pair production at LHC with CalcHEP/CompHEP in the complete model," *JHEP* **0509** (2005) 005, arXiv:hep-ph/0502067.

[40] J. L. Hewett and T. G. Rizzo, "Much ado about leptoquarks: A Comprehensive analysis," *Phys.Rev.* **D56** (1997) 5709–5724, arXiv:hep-ph/9703337.

[41] G. Leontaris and J. Vergados, "Constraints on leptoquark masses and couplings from rare processes and unification," *Phys.Lett.* **B409** (1997) 283–287, arXiv:hep-ph/9703338.

[42] M. Leurer, "A Comprehensive study of leptoquark bounds," *Phys.Rev.* **D49** (1994) 333–342, arXiv:hep-ph/9309266.

[43] M. Kramer, T. Plehn, M. Spira, and P. Zerwas, "Pair production of scalar leptoquarks at the CERN LHC," *Phys.Rev.* **D71** (2005) 057503, arXiv:hep-ph/0411038.

[44] S. Kovalenko and I. Schmidt, "Proton stability in leptoquark models," *Phys.Lett.* **B562** (2003) 104–108, arXiv:hep-ph/0210187.

[45] D0 Collaboration, "Search for pair production of first-generation leptoquarks in p anti-p collisions at s**(1/2) = 1.96-TeV," *Phys.Lett.* **B681** (2009) 224–232, arXiv:0907.1048.

[46] CMS Collaboration, "Search for Pair Production of First-Generation Scalar Leptoquarks in pp Collisions at sqrt(s) = 7 TeV," *Phys.Rev.Lett.* **106** (2011) 201802, arXiv:1012.4031.

[47] ATLAS Collaboration, "Search for pair production of first or second generation leptoquarks in proton-proton collisions at sqrt(s)=7 TeV using the ATLAS detector at the LHC," *Phys.Rev.* **D83** (2011) 112006, arXiv:1104.4481.

[48] O. S. Brüning, P. Collier, P. Lebrun, S. Myers, R. Ostojic, *et al.*, "LHC Design Report," CERN, Geneva, 2004.

[49] e. Evans, Lyndon and e. Bryant, Philip, "LHC Machine," *JINST* **3** (2008) S08001.

[50] S. D. e. a. Holmes, "Tevatron Run II Handbook,".

[51] N. Siegel, "Overview of the LHC Magnets other than the Main Dipoles. oai:cds.cern.ch:466524," Sep 2000.

[52] `http://public.web.cern.ch/public/en/research/AccelComplex-en.html`.

[53] `https://twiki.cern.ch/twiki/bin/view/AtlasPublic/LuminosityPublicResults`.

[54] ATLAS Collaboration, "The ATLAS Experiment at the CERN Large Hadron Collider," *JINST* **3** (2008) S08003.

[55] C. Collaboration, "CMS physics: Technical design report,".

[56] "LHCb : Technical Proposal," CERN, Geneva, 1998.

[57] P. Cortese, "ALICE transition-radiation detector: Technical Design Report," CERN, Geneva, 2001.

[58] V. Berardi, M. G. Catanesi, E. Radicioni, R. Herzog, R. Rudischer, *et al.*, "Total cross-section, elastic scattering and diffraction dissociation at the Large Hadron Collider at CERN: TOTEM Technical Design Report," CERN, Geneva, 2004.

[59] O. Igonkina and B. Petersen, "Proposal and Motivations for 2011 Trigger Menu," Tech. Rep. ATL-COM-DAQ-2011-007, CERN, Geneva, Jan 2011.

[60] `http://www.atlas.ch/photos/index.html`.

[61] `https://twiki.cern.ch/twiki/bin/view/AtlasPublic`.

[62] L. Rossi, P. Fischer, T. Rohe, and N. Wermes, "Pixel detectors: From fundamentals to applications," Springer, 2006.

[63] F. Djama, "Commissioning and Operation of the ATLAS Pixel Detector at the CERN LHC Collider," Tech. Rep. ATL-INDET-PROC-2010-042, CERN, Geneva, Nov 2010.

[64] N. Barlow, "Operation of the ATLAS Semiconductor Tracker," Tech. Rep. ATL-INDET-PROC-2010-003, CERN, Geneva, Feb 2010.

[65] J. Degenhardt, "Performance of the ATLAS Transition Radiation Tracker with Cosmic Rays and First High Energy Collisions at the LHC," Tech. Rep. ATL-INDET-PROC-2010-040, CERN, Geneva, Nov 2010.

[66] L. Mandelli, "The ATLAS Electromagnetic Calorimeters: Features and Performance," 2009.

[67] F. Bertolucci, "The ATLAS Tile Calorimeter performance at LHC in pp collisions at 7 TeV," Tech. Rep. ATL-TILECAL-PROC-2012-001, CERN, Geneva, Jan 2012.

[68] B. Dowler, J. L. Pinfold, J. Soukup, M. G. Vincter, A. P. Cheplakov, *et al.*, "Performance of the ATLAS Hadronic End-Cap Calorimeter in Beam Tests. oai:cds.cern.ch:684257," Tech. Rep. ATL-LARG-2001-019, Max-Planck Inst., München, Oct 2001. revised version number 1 submitted on 2001-10-23 16:19:22.

[69] D. Gillberg, "Performance of the ATLAS Forward Calorimeters in First LHC Data," Tech. Rep. ATL-LARG-PROC-2010-006, CERN, Geneva, Aug 2010.

[70] E. Rezaie, "COMMISSIONING OF THE ATLAS LIQUID ARGON CALORIMETERS," Master's thesis, Simon Fraser University, 2008.

[71] `https://twiki.cern.ch/twiki/bin/view/AtlasPublic/MuonPerformancePublicPlotsSimulation`.

[72] D. Sampsonidis, C. Anastopoulos, A. Liolios, M. Manolopoulou, and C. Petridou, "Study of the performance of the ATLAS monitored drift tube chambers under the influence of heavily ionizing α-particles," 2004.

[73] M. Iodice, "Calibration and Performance of the Precision Chambers of the ATLAS Muon Spectrometer," Tech. Rep. ATL-MUON-PROC-2011-009, CERN, Geneva, Nov 2011.

[74] "Performance of the ATLAS Muon Trigger in p-p collisions at $\sqrt{s} = 7$ TeV," Tech. Rep. ATLAS-CONF-2010-095, CERN, Geneva, Oct 2010.

[75] `http://atlas-ma.web.cern.ch/atlas-ma/`.

[76] ATLAS Collaboration, "Luminosity Determination in pp Collisions at sqrt(s) = 7 TeV using the ATLAS Detector in 2011," Tech. Rep. ATLAS-CONF-2011-116, CERN, Geneva, Aug 2011.

[77] T. Sykora, "Physics program of ALFA and precision luminosity measurement in ATLAS," Tech. Rep. ATL-PHYS-PROC-2011-250, CERN, Geneva, Nov 2011.

[78] D. Casadei, "Performance of the ATLAS trigger system," Tech. Rep. ATL-DAQ-PROC-2012-004, CERN, Geneva, May 2012.

[79] C. Borer, "Overview of the ATLAS data acquisition system operating at the TeV scale," Tech. Rep. ATL-DAQ-PROC-2011-015, CERN, Geneva, Mar 2011.

[80] T. Cornelissen, M. Elsing, S. Fleischmann, W. Liebig, E. Moyse, *et al.*, "Concepts, Design and Implementation of the ATLAS New Tracking (NEWT)," Tech. Rep. ATL-SOFT-PUB-2007-007. ATL-COM-SOFT-2007-002, CERN, Geneva, Mar 2007.

[81] E. Bouhova-Thacker, P. Lichard, V. Kostyukhin, W. Liebig, M. Limper, *et al.*, "Vertex Reconstruction in the ATLAS Experiment at the LHC," Tech. Rep. ATL-INDET-PUB-2009-001. ATL-COM-INDET-2009-011, CERN, Geneva, May 2009. Note was a proceeding for IEEE/NSS Dresden 2008 and is now intended for possible publication in TNS.

[82] W. Lampl, S. Laplace, D. Lelas, P. Loch, H. Ma, *et al.*, "Calorimeter Clustering Algorithms: Description and Performance," Tech. Rep. ATL-LARG-PUB-2008-002. ATL-COM-LARG-2008-003, CERN, Geneva, Apr 2008.

[83] M. Cacciari, G. P. Salam, and G. Soyez, "The Anti-k(t) jet clustering algorithm," *JHEP* **0804** (2008) 063, `arXiv:0802.1189`.

[84] Y. L. Dokshitzer, G. Leder, S. Moretti, and B. Webber, "Better jet clustering algorithms," *JHEP* **9708** (1997) 001, `arXiv:hep-ph/9707323`.

[85] S. D. Ellis and D. E. Soper, "Successive combination jet algorithm for hadron collisions," *Phys.Rev.* **D48** (1993) 3160–3166, `arXiv:hep-ph/9305266`.

[86] ATLAS Collaboration, "Jet energy measurement with the ATLAS detector in proton-proton collisions at sqrt(s) = 7 TeV," `arXiv:1112.6426`.

[87] "Jet energy scale and its systematic uncertainty in proton-proton collisions at sqrt(s)=7 TeV in ATLAS 2010 data," Tech. Rep. ATLAS-CONF-2011-032, CERN, Geneva, Mar 2011.

[88] ATLAS Collaboration, "Expected electron performance in the ATLAS experiment," Tech. Rep. ATL-PHYS-PUB-2011-006, CERN, Geneva, Apr 2011.

[89] `https://twiki.cern.ch/twiki/bin/viewauth/AtlasProtected/ElectronReconstruction`.

[90] ATLAS Collaboration, "Electron performance measurements with the ATLAS detector using the 2010 LHC proton-proton collision data," Tech. Rep. CERN-PH-EP-2011-117, CERN, Geneva, 2011.

[91] ATLAS Collaboration, "ATLAS muon spectrometer: Technical Design Report," CERN, Geneva, 1997.

[92] `https://twiki.cern.ch/twiki/bin/viewauth/AtlasProtected/STACODocumentation`.

[93] F. Siegert, "Monte-Carlo event generation for the LHC," PhD thesis, Durham University, 2010.

[94] M. L. Mangano and T. J. Stelzer, "TOOLS FOR THE SIMULATION OF HARD HADRONIC COLLISIONS," *Annual Review of Nuclear and Particle Science* **55** (2005) 555–588.

[95] M. Dobbs, S. Frixione, E. Laenen, K. Tollefson, H. Baer, *et al.*, "Les Houches guidebook to Monte Carlo generators for hadron collider physics," `arXiv:hep-ph/0403045`, Compiled by the Working Group on Quantum Chromodynamics and the Standard Model.

[96] D. J. Griffiths, "Introduction to elementary particles; 2nd rev. version," Wiley, New York, NY, 2008.

[97] Y. Kurihara, J. Fujimoto, T. Ishikawa, K. Kato, S. Kawabata, *et al.*, "QCD event generators with next-to-leading order matrix elements and parton showers," *Nucl.Phys.* **B654** (2003) 301–319, `arXiv:hep-ph/0212216`, 18 pages, 6 figures, version 2: update reference [13] Report-no: KEK-CP-121.

[98] *Monte-Carlo Methods*, pp. 249–280. Wiley-VCH Verlag GmbH & Co. KGaA, 2006.

[99] V. N. Gribov and L. N. Lipatov, "Deep inelastic ep scattering in perturbation theory," *Sov. J. Nucl. Phys.* **15** (1972), no. 4, 438–450.

[100] Y. L. Dokshitzer, "Calculation of the Structure Functions for Deep Inelastic Scattering and e+ e- Annihilation by Perturbation Theory in Quantum Chromodynamics," *Sov. Phys. JETP* **46** (1977) 641–653.

[101] G. Altarelli and G. Parisi, "Asymptotic Freedom in Parton Language," *Nucl. Phys.* **B126** (1977) 298.

[102] B. Andersson, G. Gustafson, G. Ingelman, and T. Sjöstrand, "Parton fragmentation and string dynamics," Tech. Rep. LUTP-83-10, Lunds Univ. Dept. Theor. Phys., Lund, Apr 1983.

[103] B. Andersson and M. Ringnér, "Bose-Einstein Correlations in the Lund Model," Tech. Rep. hep-ph/9704383. LUTP-97-07, Lunds Univ. Dept. Theor. Phys., Lund, Apr 1997.

[104] B. R. Webber, "A QCD model for jet fragmentation including soft gluon interference. oai:cds.cern.ch:147786," *Nucl. Phys. B* **238** Sep (1983) 492–528. 53 p.

[105] J. C. Winter, F. Krauss, and G. Soff, "A modified cluster-hadronization model. oai:cds.cern.ch:681839," *Eur. Phys. J. C* **36** Nov (2003) 381–395. 18 p.

[106] G. Corcella, I. Knowles, G. Marchesini, S. Moretti, K. Odagiri, *et al.*, "HERWIG 6: An Event generator for hadron emission reactions with interfering gluons (including supersymmetric processes)," *JHEP* **0101** (2001) 010, `arXiv:hep-ph/0011363`.

[107] `http://jimmy.hepforge.org/`.

[108] J. M. Butterworth, J. R. Forshaw, and M. H. Seymour, "Multiparton interactions in photoproduction at HERA," *Z. Phys.* **C72** (1996) 637–646, `hep-ph/9601371`.

[109] T. Sjöstrand, S. Mrenna, and P. Skands, "PYTHIA 6.4 physics and manual," *Journal of High Energy Physics* **2006** (2006), no. 05, 026.

[110] T. Gleisberg, S. Hoeche, F. Krauss, M. Schoenherr, S. Schumann, *et al.*, "Event generation with SHERPA 1.1," *J. High Energy Phys.* **02** Dec (2008) 007, Comments: 47 pages, 21 figures.

[111] M. L. Mangano, M. Moretti, F. Piccinini, R. Pittau, and A. D. Polosa, "ALPGEN, a generator for hard multiparton processes in hadronic collisions," *JHEP* **0307** (2003) 001, arXiv:hep-ph/0206293.

[112] B. P. Kersevan and E. Richter-Was, "The Monte Carlo event generator AcerMC version 2.0 with interfaces to PYTHIA 6.2 and HERWIG 6.5," arXiv:hep-ph/0405247.

[113] S. Frixione and B. R. Webber, "Matching NLO QCD computations and parton shower simulations," *JHEP* **0206** (2002) 029, arXiv:hep-ph/0204244.

[114] P. Nason, "A New method for combining NLO QCD with shower Monte Carlo algorithms," *JHEP* **0411** (2004) 040, arXiv:hep-ph/0409146.

[115] A. Rimoldi, A. Dell'Acqua, M. Gallas, A. Nairz, J. Boudreau, *et al.*, "The Simulation of the ATLAS Experiment: Present Status and Outlook," Tech. Rep. ATL-SOFT-2004-004. ATL-COM-SOFT-2004-006. CERN-ATL-COM-SOFT-2004-006, CERN, Geneva, 2004.

[116] S. Agostinelli, J. Allison, K. Amako, J. Apostolakis, H. Araujo, *et al.*, "Geant4 a simulation toolkit," *Nuclear Instruments and Methods in Physics Research Section A: Accelerators, Spectrometers, Detectors and Associated Equipment* **506** (2003), no. 3, 250 – 303.

[117] J. Butterworth, E. Dobson, U. Klein, B. M. Garcia, T. Nunnemann, *et al.*, "Single Boson and Diboson Production Cross Sections in pp Collisions at s = 7 TeV," Tech. Rep. ATL-COM-PHYS-2010-695, CERN, Geneva, 2010.

[118] A. Sherstnev and R. Thorne, "Parton Distributions for LO Generators," *Eur.Phys.J.* **C55** (2008) 553–575, arXiv:0711.2473.

[119] K. Chen, C. Deluca, B. DeWilde, J. Farley, T. Gadfort, *et al.*, "Searches for first generation leptoquarks in dielectron plus jets and electron,Etmiss plus jets final states using the ATLAS detector.," Tech. Rep. ATL-COM-PHYS-2011-1151, CERN, Geneva, Aug 2011.

[120] M. Hance, D. Olivito, and H. H. Williams, "Performance Studies for e/gamma Calorimeter Isolation," Tech. Rep. ATL-COM-PHYS-2011-1186, CERN, Geneva, 2011.

[121] D0 Collaboration, "Measurement of the shape of the boson rapidity distribution for $p\bar{p} \to Z/gamma^* \to e^+e^- + X$ events produced at $\sqrt{s}$ of 1.96-TeV," *Phys.Rev.* **D76** (2007) 012003, arXiv:hep-ex/0702025.

[122] S. Heim, private communication, unpublished.

[123] J. Hass, "RooFit Tutorial," unpublished.

[124] J. Farley, "QCD Fake Rates for the Matrix Method," unpublished.

[125] Hobbs, "Choosing normalization scale factors," unpublished.

[126] G. Romeo, A. Schwartzman, R. Piegaia, T. Carli, and R. Teuscher, "Jet Energy Resolution from In-situ Techniques with the ATLAS Detector Using Proton-Proton Collisions at a Center of Mass Energy $\sqrt{s} = 7$ TeV," Mar 2011.

[127] T. Junk, "Confidence level computation for combining searches with small statistics," *Nucl.Instrum.Meth.* **A434** (1999) 435–443, arXiv:hep-ex/9902006.

[128] A. Frodesen, O. Skjeggestad, and H. Tofte, "PROBABILITY AND STATISTICS IN PARTICLE PHYSICS," 1979.

[129] F. James, "Statistical methods in experimental physics," 2006.

[130] W. Fisher, "Collie: A Confidence Level Limit Evaluator," Tech. Rep. DZero note 5595, Fermilab, June 2009.

[131] W. Fisher, "Calculating Limits for Combined Analyses," 2005, DZero note 4975.

[132] ATLAS Collaboration, "Search for first generation scalar leptoquarks in pp collisions at sqrts=7 TeV with the ATLAS detector," *Phys.Lett.* **B709** (2012) 158–176, arXiv:1112.4828.

[133] C. Gemme, "ATLAS Upgrade Programme," unpublished.

[134] ATLAS Collaboration, "Charged-particle multiplicities in pp interactions measured with the ATLAS detector at the LHC," *New J.Phys.* **13** (2011) 053033, arXiv:1012.5104, Long author list - awaiting processing.

[135] M. Capeans, G. Darbo, K. Einsweiller, M. Elsing, T. Flick, *et al.*, "ATLAS Insertable B-Layer Technical Design Report," Tech. Rep. CERN-LHCC-2010-013. ATLAS-TDR-019, CERN, Geneva, Sep 2010.

[136] S. Grinstein, "Overview of the ATLAS Insertable B-Layer (IBL) Project," Tech. Rep. ATL-INDET-PROC-2012-004, CERN, Geneva, Jan 2012.

[137] P. Hansson, J. Balbuena, C. Barrera, E. Bolle, M. Borri, *et al.*, "3D silicon pixel sensors: Recent test beam results," *Nuclear Instruments and Methods in Physics Research Section A: Accelerators, Spectrometers, Detectors and Associated Equipment* **628** (2011), no. 1, 216 – 220.

[138] `http://atlas-highlumi-3dsensor.web.cern.ch/atlas-highlumi-3dsensor/Default.htm`.

[139] J. Boudreau and V. Tsulaia, "The GeoModel toolkit for detector description," 2005.

[140] A. Salzburger, S. Todorova, and M. Wolter, "The ATLAS Tracking Geometry Description," Tech. Rep. ATL-SOFT-PUB-2007-004. ATL-COM-SOFT-2007-009, CERN, Geneva, Jun 2007.

[141] "Commissioning of the ATLAS high-performance b-tagging algorithms in the 7 TeV collision data," Tech. Rep. ATLAS-CONF-2011-102, CERN, Geneva, Jul 2011.

Appendix A

Insertable B-Layer Simulation and Performance

A.1 Motivation

A series of upgrades are foreseen for the LHC to allow operation at higher energy and instantaneous luminosity. In 2011, the LHC operated at a center-of-mass energy of $\sqrt{s} = 7$ TeV and a peak instantaneous luminosity of $L \approx 3.5 \times 10^{33}$ cm^{-2}s^{-1}. The 2012 run period has just begun at an energy of $\sqrt{s} = 8$ TeV, and the instantaneous luminosity is expected to reach $L \approx 6 \times 10^{33}$ cm^{-2}s^{-1} [133]. Following the 2012 run period, a long shutdown of the LHC will allow operation to resume in late 2014 at or near the design energy of $\sqrt{s} = 14$ TeV. The instantaneous luminosity is expected to reach $L \approx 1 \times 10^{34}$ cm^{-2}s^{-1} at this time. A second (third) long shutdown is expected around 2018 (2022), after which the instantaneous luminosity is expected to reach $L \approx 2.5$ (5) $\times 10^{34}$ cm^{-2}s^{-1}.

With the increases in energy, the particle multiplicity per interaction will increase [134]. With the increases in luminosity, the amount of pileup interactions per bunch crossing will increase, which will also lead to an increase in the particle multiplicity, as shown in Figure A.1. Therefore, a series of upgrades to the ATLAS detector are planned in order to at least maintain the present level of performance under more challenging operating conditions, with the hope of actually improving the performance. These planned upgrades are referred to Phase-0, Phase-I, and Phase-II, and are scheduled to coincide with the LHC upgrades in 2013, ∼2018, and ∼2022 respectively.

As part of the Phase-0 upgrades, a new barrel layer of pixels, referred to as the "insertable b-layer" (IBL), will be inserted into the existing Pixel Detector. There is insufficient space between the existing b-layer and beam pipe for an

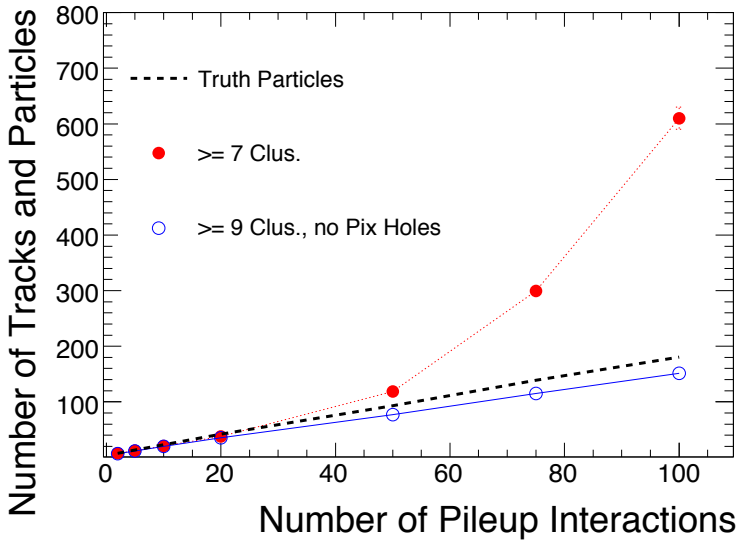

Figure A.1: Average number of reconstructed tracks and average number of true particles per event under different pileup conditions. Two track definitions are considered. The average number of tracks reconstructed using the nominal ATLAS track definition is represented by the filled red dots, and the number reconstructed using a stricter definition, designed to reduce reconstruction of fake tracks, is represented by the empty blue dots. The average number of true particles is represented by the dashed line [135].

additional layer, so the portion of the beam pipe located within the ATLAS detector will be replaced with a smaller radius beam pipe. The current beam pipe has an outer radius of 36 mm, while the new beam pipe will have an outer radius of only 29 mm. The IBL will occupy the space between the new beam pipe and the current b-layer. As part of the Phase-II upgrades, the entire ID will be replaced.

The current b-layer was designed to operate up to an instantaneous luminosity of $L \approx 1 \times 10^{34}$ cm^{-2}s^{-1}. Above this luminosity, inefficiencies in the front-end and module control chips set in, and some hits will be lost. It is now expected that an instantaneous luminosity of $L \approx 2.5 \times 10^{34}$ cm^{-2}s^{-1} will be reached before the Phase-II upgrades and the replacement of the ID. The IBL will be capable of operating efficiently at this luminosity, and will provide additional hits to mitigate the effect of lost b-layer hits due to output saturation. The enhanced pileup at this luminosity can also lead to fake tracks being reconstructed from random collections of hits from different low p_T particles. The IBL will improve the pattern recognition capabilities and help to reduce the number of these fake reconstructed tracks.

Also, it is anticipated that the LHC will deliver $\sim$300 fb^{-1} of integrated luminosity before the Phase-II shutdown, when the ID will be replaced. This is the expected lifetime of the current b-layer, after which significant performance degradation due to radiation damage is expected to set in. If no serious performance degradation occurs to the existing b-layer, then the addition of the IBL should significantly improve track impact parameter resolution, and hence vertex reconstruction and b-tagging performance. However, if the expected integrated luminosity is underestimated and/or the potential lifetime is overestimated, performance of the current b-layer would degrade due to radiation damage. In this case, it is hoped that the IBL will be capable of at least restoring the nominal performance.

A.2 Hardware

The IBL is an additional pixel barrel layer concentric with the existing pixel layers [135] [136]. A schematic drawing of a portion of the new beam pipe and IBL in the $r - \phi$ plane is shown in Figure A.2. The pixel size is 50×250 μm, compared to 50×400 μm for the existing pixels. The average radial distance of the sensors to the IP is 33 mm. Due to its close proximity to the IP, the radiation exposure and hit rate will be even greater than that experienced in the current b-layer. The IBL must remain functional until the entire ID is replaced during the Phase-II upgrades. In order to achieve this, a new front-end chip has been developed which is more radiation hard and

has a higher hit rate capability. Also, two different sensor technologies will be utilized.

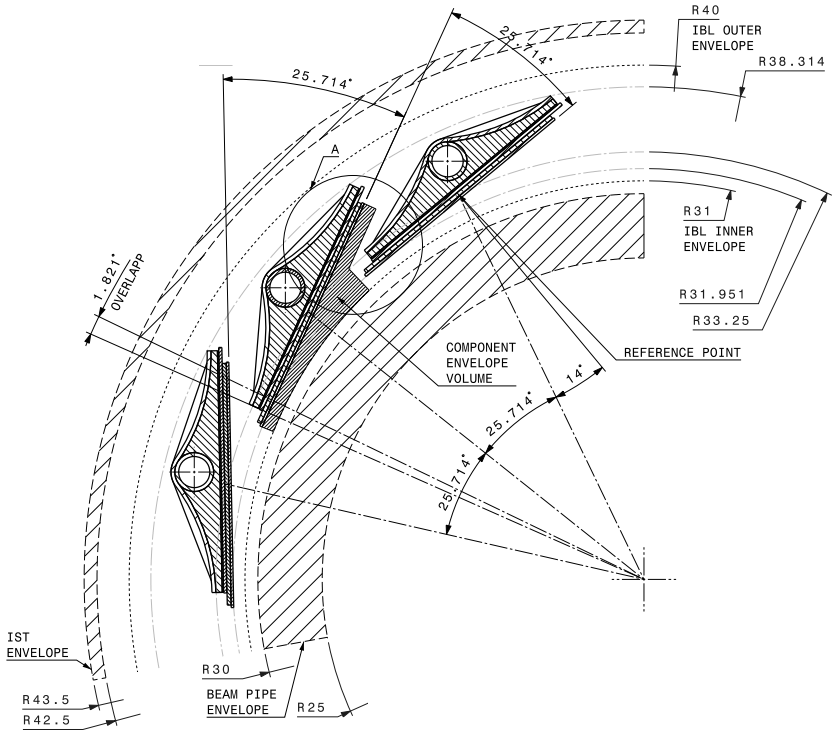

Figure A.2: Schematic drawing of a portion of the IBL and proposed beam pipe in the $r - \phi$ plane [135].

Planar sensors will be used in the central region. These are similar to the existing pixel sensors, but slightly less thick, only 200 μm compared to 250 μm. At higher $|\eta|$, 3D sensors may be utilized. A basic schematic of a 3D pixel sensor is shown in Figure A.3. Alternating column-like n^+ and p^+ implants serve as electrodes, extending into the sensor bulk. This allows the depletion zone to grow parallel to the sensor surface, rather than perpendicular, as in the planar case. The thickness, and therefore the distance over which a traversing charged particle produces electron-hole pairs, remains as large as in planar sensors, but the distance these electron-hole pairs must drift before they are read out can be reduced drastically. This is shown in Figure A.4. Also, a much lower bias voltage is needed to fully deplete 3D sensors compared to planar sensors. Before being exposed to any radiation, the planar (3D) sensors will require 30 (5-10) V for full depletion. At the end of the IBL lifetime, the planar

(3D) sensors will require 1000 (160) V for full depletion, and operate with a hit efficiency of 97.6% (98.7%) for a typical 15° incidence angle [136]. These values were measured using a 120 GeV pion test beam [137] and irradiated sensors.

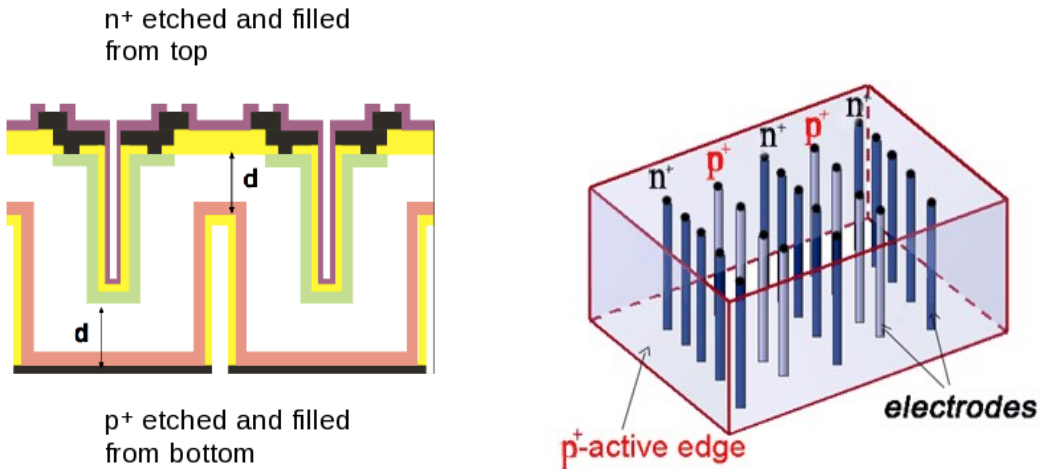

Figure A.3: Schematic drawings of a 3D pixel sensor [135].

A.3 Software Implementation

In order to make design decisions and evaluate the potential performance of the ATLAS detector with the addition of the IBL, it was necessary to incorporate the IBL into the ATLAS software framework [135]. The first step of this process was to create a geometrical description of the IBL and the new beam pipe within the GeoModel [139] framework, a toolkit for the description of complex detector geometries. The entire ATLAS detector is described in this framework, and this description is used by both the simulation and reconstruction software, ensuring a common detector description for these tasks. All the detector information needed for simulation and reconstruction is thus contained within the GeoModel description, including the physical geometry, materials, sensitive regions, readout systems, etc. The initial description of the IBL used planar sensors, since these were already well described in the ATLAS framework. Modules were described accurately, according to current expectations. The support and cooling infrastructure was not yet well defined, so its material distribution was smeared out and represented by a uniform alu-

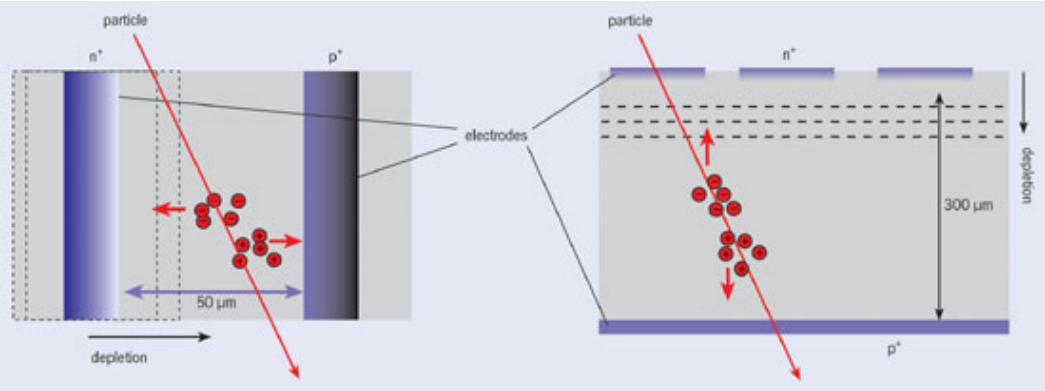

Figure A.4: Schematic comparison of a 3D sensor (left) and a planar sensor (right). The thickness is the same in both cases, but the drift length is considerably shorter in the 3D sensor. [138].

minium tube just outside the IBL modules. The IBL as initially implemented in the ATLAS software framework is shown in Figure A.5.

From the GeoModel detector description, a Geant4 detector description is obtained with the Geo2G4 [139] algorithm, for use in simulation and digitization. This is an extremely detailed and accurate description of the detector geometry and material distribution. For reconstruction, this level of detail is unnecessary and computationally expensive. A simplified "TrackingGeometry" [140] description of the detector is sufficient. The TrackingGeometry is a coarse description of the detector components and their location, derived from the GeoModel description, with material properties taken from a material map. The material map is obtained from the Geant4 detector description by stepping non-interacting "Geantino" particles through the detector, and recording the radiation length X_0, density ρ, atomic number Z, and mass index A as a function of position. This information is then used during reconstruction for track extrapolation and fitting. A comparison of the material distribution represented by the Pixel Detector and IBL as a function of η is shown in Figure A.6, according to the Geant4 and TrackingGeometry detector descriptions.

With the inclusion of the IBL in the GeoModel description and material map, the full chain of simulation, digitization, and reconstruction can be performed. Initially, the standard ATLAS track reconstruction algorithms were used, with the additional hit information form the IBL. Also, the standard ATLAS vertex reconstruction and b-tagging algorithms were used. In the future, these algorithms will be re-optimized to better incorporate the IBL.

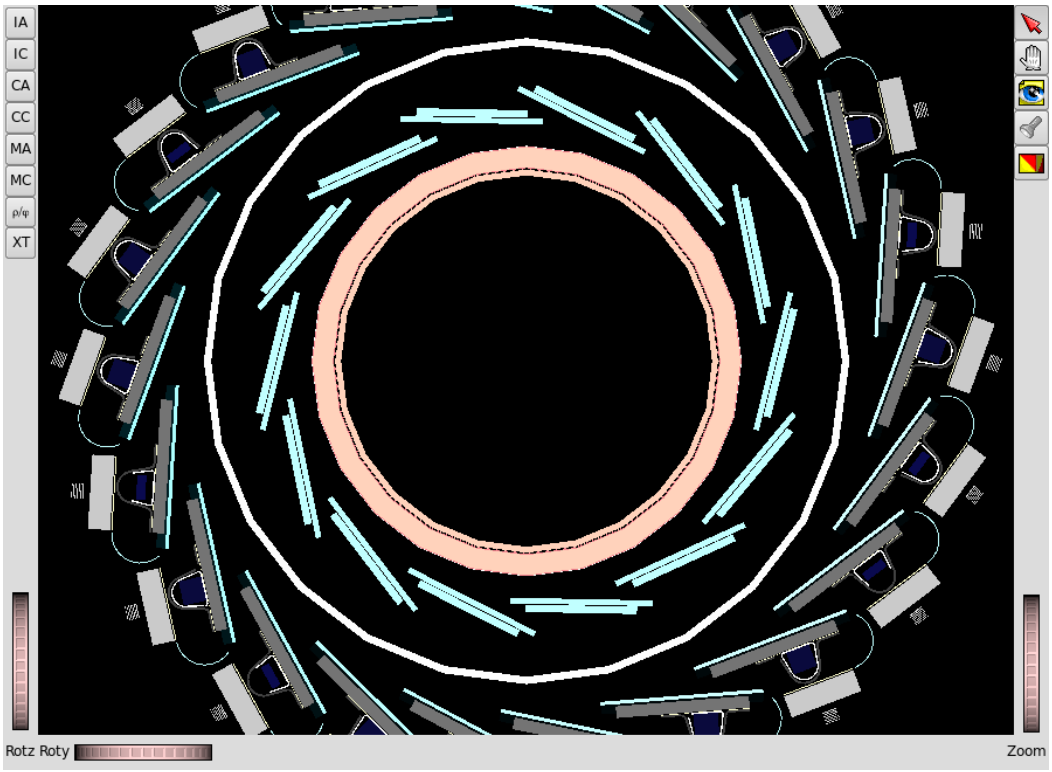

Figure A.5: GeoModel description of the proposed beam pipe, IBL, and current b-layer, viewed in the $r - \phi$ plane. The beam pipe is shown in pink, the IBL modules in light blue, and the services tube in white. Outside the services tube are the modules of the current b-layer and the associated services [135].

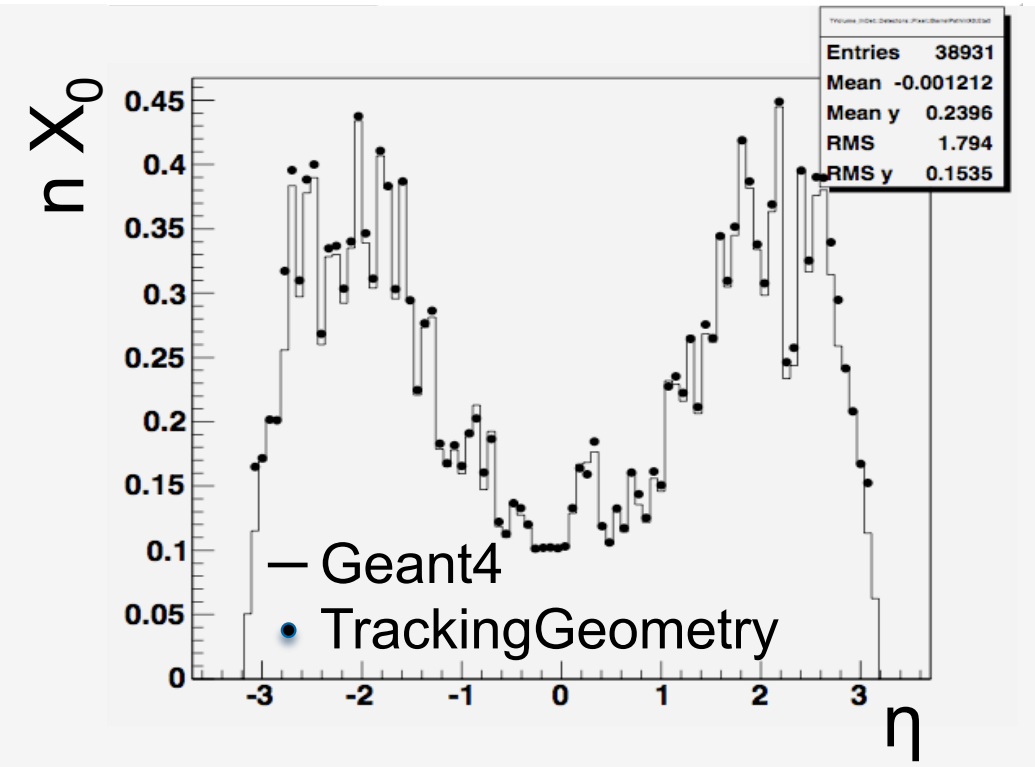

Figure A.6: IBL and Pixel Detector material distribution. The number of radiation lengths versus η according to the Geant4 (TrackingGeometry) detector description is represented by the line (dots). The two descriptions show good agreement.

A.4 Performance Evaluation

As a first (optimistic) evaluation of the IBL performance, no radiation damage or pileup was assumed. This describes the potential performance of ATLAS with the IBL under ideal conditions. Several physics scenarios were considered. The tracking efficiency was evaluated in $t\bar{t}$ MC events with and without the IBL. As shown in Figure A.7, the addition of the IBL has no significant effect.

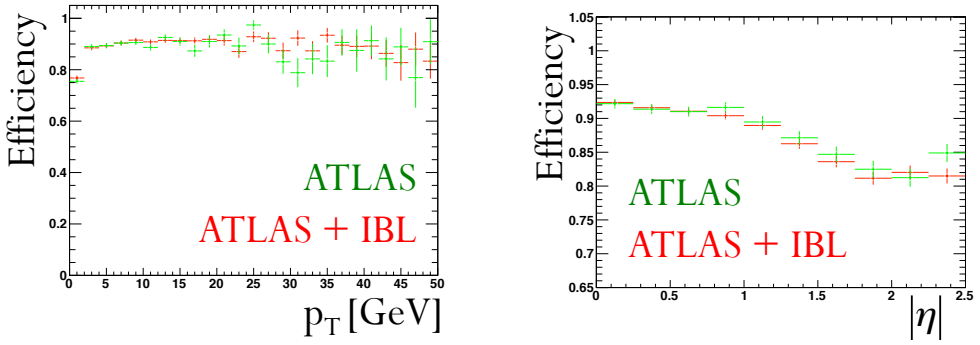

Figure A.7: Tracking efficiency measured in $t\bar{t}$ MC, with (red) and without (green) the inclusion of the IBL. The efficiency measured with respect to track p_T ($|\eta|$) is shown on the left (right).

The q/p_T resolution was evaluated in a MC sample composed of events containing a single muon and no other particles. The resolution is defined as the width of a Gaussian fit to a histogram containing the difference between the true and measured values of q/p_T. The muons were generated with 1 GeV $< p_T <$ 100 GeV. The extra space point measurement provided by the IBL only marginally increases the distance over which the track curvature is measured. The introduction of additional material leads to a degradation of the q/p_T resolution. These two factors offset, and the resolution is not significantly affected by the addition of the IBL, as shown in Figure A.8.

The impact parameter resolution was measured in a single pion MC sample. The resolution is defined as the width of a Gaussian fit to a histogram containing the difference between the true and measured values of the impact parameter. This is an important factor in determining the ultimate b-tagging performance, as b-jets are composed mainly of pions. Here, as expected, a significant improvement is found with the addition of the IBL. The improvement is due to the extra space point measurement quite close to the IP. In the

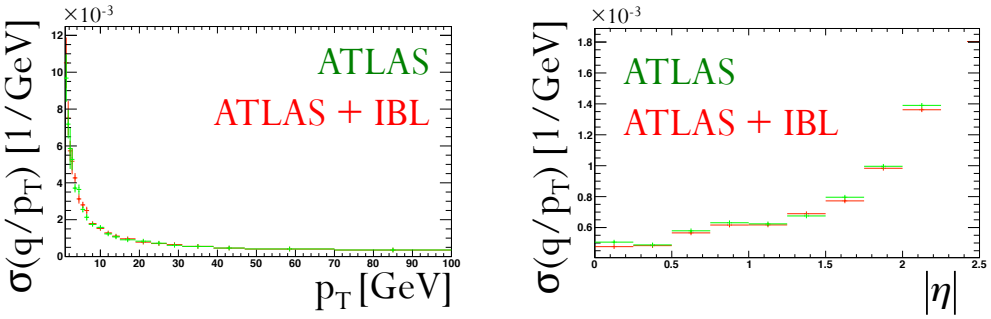

Figure A.8: q/p_T resolution measured in single muon MC, with (red) and without (green) the inclusion of the IBL. The resolution measured with respect to muon p_T ($|\eta|$) is shown on the left (right).

longitudinal direction, the improvement is even more pronounced, as the pixel size in this direction is reduced in the IBL. The impact parameter resolution is shown in Figure A.9.

B-tagging algorithms are designed to determine as accurately as possible if a jet originates from a b quark. Many algorithms return a jet weight, which tends to take large values for jets from b quarks, and small values for jets from light quarks, as shown in Figure A.10 for the IP3D+SV1 b-tagging algorithm [141]. A threshold value of this weight is chosen, and jets with a weight above this value are deemed b-jets. Choosing a large value of the threshold leads to a low light jet mis-tag rate (defined as the fraction of light jets which are mistakenly tagged as b-jets), but poor b-jet efficiency (defined as the fraction of b-jets which are correctly tagged as b-jets). Likewise, choosing a small value leads to good b-jet efficiency, but a poor mis-tag rate. Thus, the value of the threshold must be chosen carefully. A comparison of the light jet rejection (defined as the inverse of the mis-tag rate) and b-jet efficiency for a range of threshold values, with and without the IBL, is shown in Figure A.10, as measured using truth-matching in a $t\bar{t}$ MC sample.

Increased pileup interactions make vertex reconstruction, and therefore b-tagging, more difficult. Shown in Figure A.11 is the difference between a reconstructed dijet event in the absence of pileup and with the typical pileup for $L = 2 \times 10^{34}$ cm^{-2}s^{-1}. It is important to understand the b-tagging performance for various pileup scenarios. The light jet rejection, measured using truth-matching in $t\bar{t}$ MC samples with 0, 25, and 50 pileup interactions is shown in Figure A.12. In each case, the jet weight threshold was chosen to

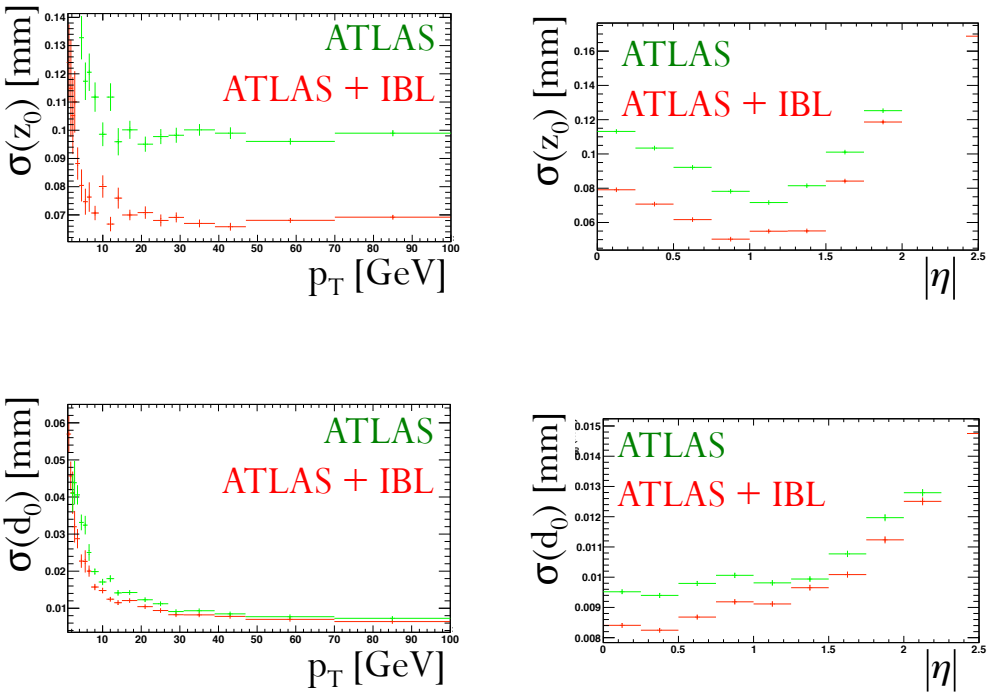

Figure A.9: Track impact parameter resolution measured in single pion MC, with (red) and without (green) the inclusion of the IBL. The resolution measured with respect to pion p_T ($|\eta|$) is shown on the left (right). The top (bottom) row shows the longitudinal (transverse) impact parameter resolution.

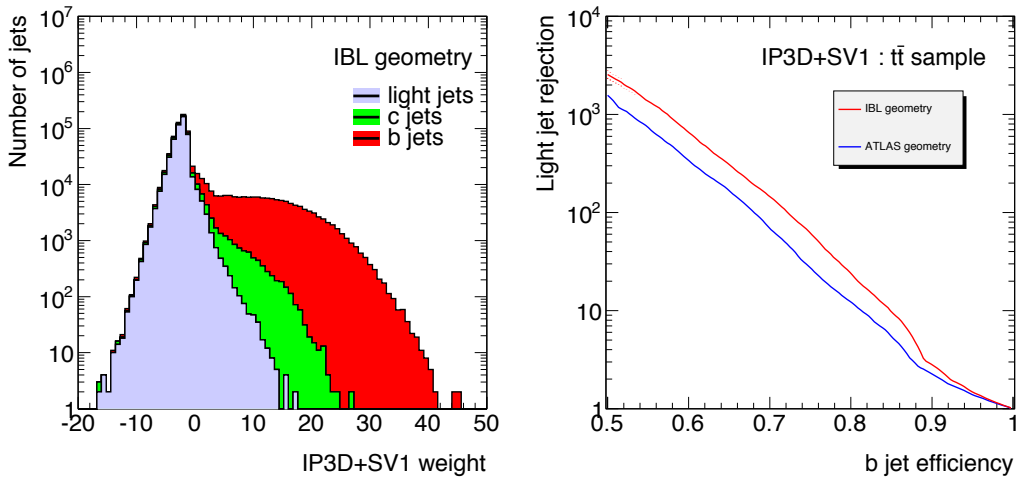

Figure A.10: Jet weight for light and b-jets according to the IP3D+SV1 b-tagging algorithm for the IBL geometry (left) and the light jet rejection versus b-jet efficiency for the ATLAS and IBL geometries (right), derived from $t\bar{t}$ MC [135].

yield a 60% b-jet efficiency. The rejection is shown using the nominal ATLAS track selection, and also using a stricter track selection designed to reduce fake track reconstruction due to random hits from pileup interactions. In all pileup scenarios considered, the light jet rejection improves using the stricter track definition. The improvement increases with increasing pileup interactions per event. Using the strict track definition, the light jet rejection with the IBL in events with 50 pileup interactions exceeds that observed without the IBL in events with no pileup.

It is also important to consider potential radiation damage effects in the existing b-layer. The most extreme damage scenario would entail complete b-layer failure. The light jet rejection measured in $t\bar{t}$ MC samples with 0, 25, and 50 pileup interactions is shown in Figure A.13, with a fully functional and a non-operational pixel b-layer. Without the IBL and a non-operational b-layer, it is not possible to achieve a 60% b-tagging efficiency. With the IBL and a non-operational b-layer, the light jet rejection exceeds that observed with a perfectly functional ATLAS detector for all pileup scenarios considered.

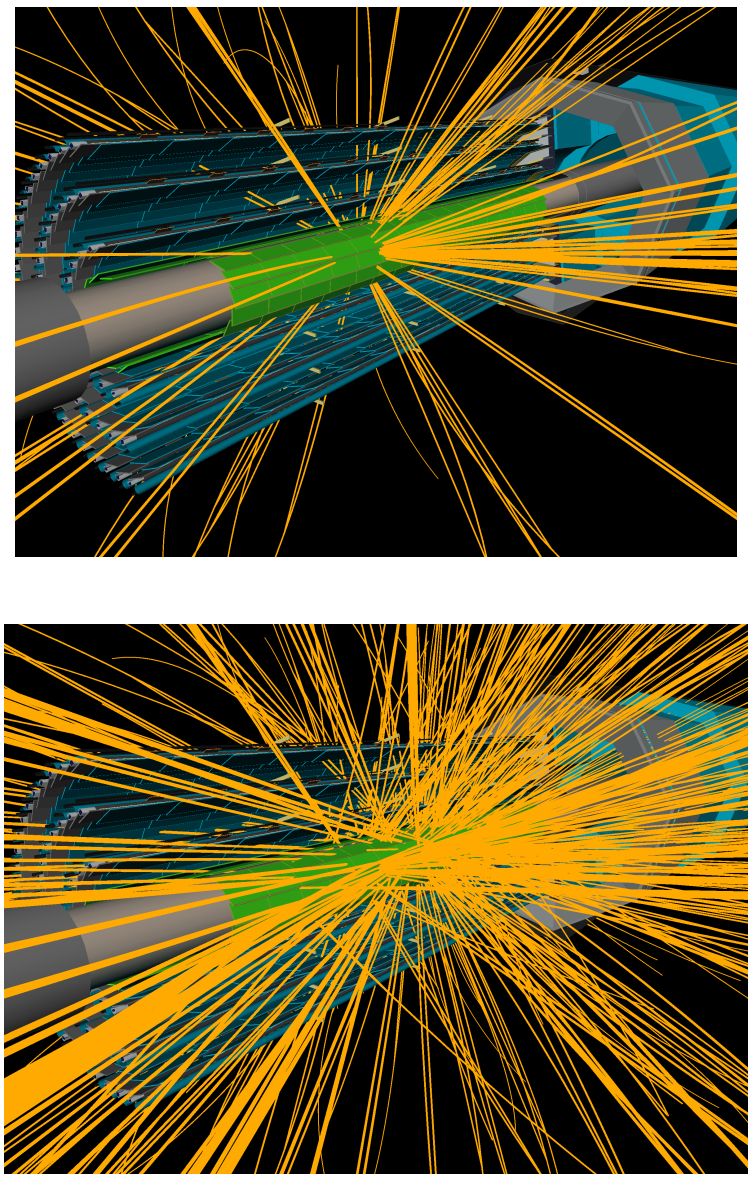

Figure A.11: Dijet event reconstructed with the IBL geometry, in the absence of pileup (top) and with typical pileup for $L = 2 \times 10^{34}$ cm^{-2}s^{-1} (bottom). The IBL is shown in green, the current Pixel Detector is shown in blue, and reconstructed tracks are shown in orange [135].

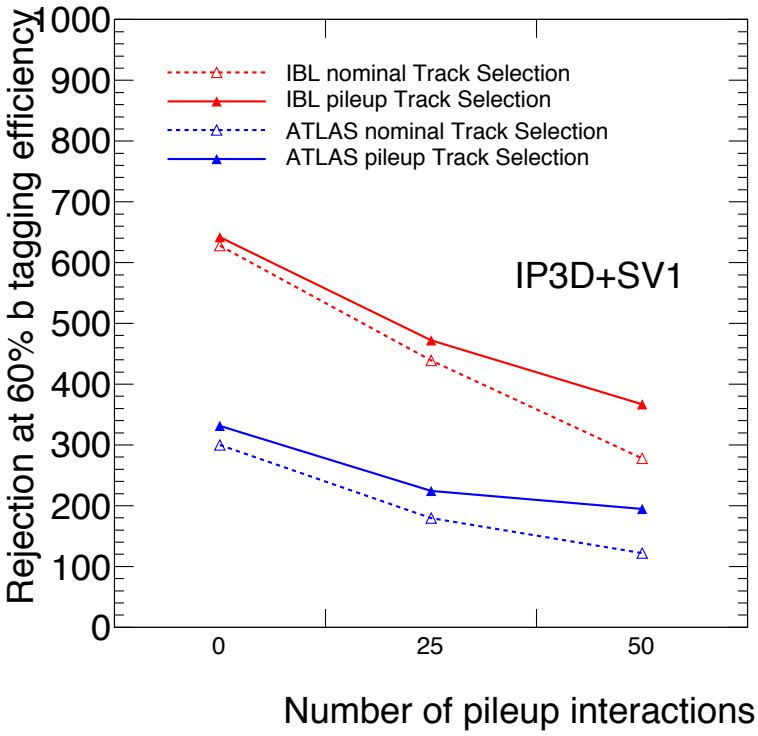

Figure A.12: Light jet rejection for the IP3D+SV1 b-tagging algorithm evaluated in $t\bar{t}$ MC with different levels of simulated pileup. In each case, the jet weight threshold was chosen to yield a 60% b-jet efficiency. Results for the IBL (ATLAS) geometry are shown in red (blue). Two track definitions are considered; results using the default ATLAS track definition are shown by dashed lines, whereas results using a stricter track definition are shown by solid lines [135].

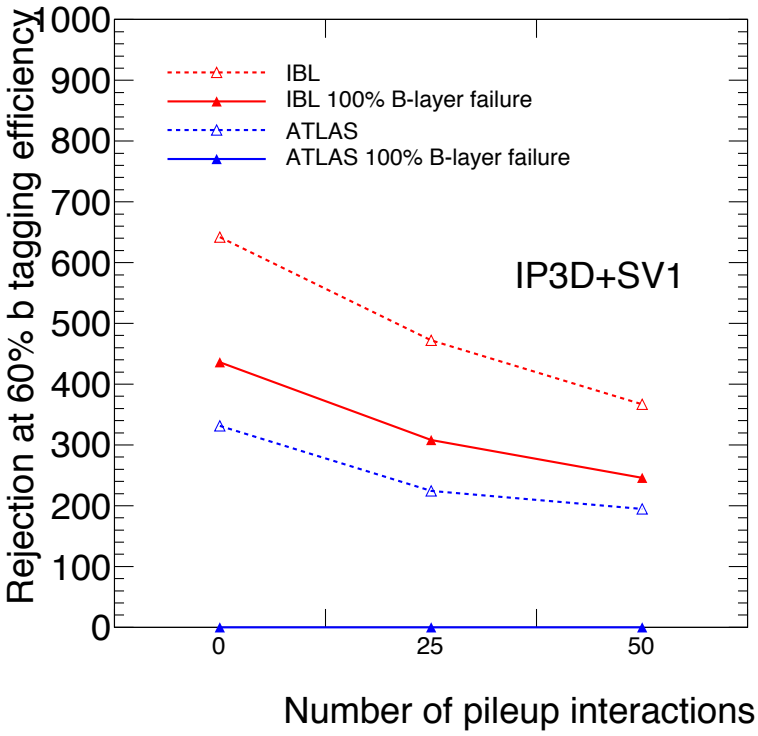

Figure A.13: Light jet rejection for the IP3D+SV1 b-tagging algorithm evaluated in $t\bar{t}$ MC with different levels of simulated pileup. In each case, the jet weight threshold was chosen to yield a 60% b-jet efficiency. Results for the IBL (ATLAS) geometry are shown in red (blue). Two pixel b-layer scenarios are considered; results assuming a fully functional b-layer are shown by dashed lines, whereas results assuming a non-operational b-layer are shown by solid lines [135].